Clemson University
TigerPrints

All Theses | Theses

8-2018

Novel Parallel Continuum Robot Grippers and their Modeling

Phanideep Satyanarayana Gonthina
Clemson University, pgonthi@clemson.edu

Follow this and additional works at: https://tigerprints.clemson.edu/all_theses

Recommended Citation
Gonthina, Phanideep Satyanarayana, "Novel Parallel Continuum Robot Grippers and their Modeling" (2018). *All Theses*. 2942.
https://tigerprints.clemson.edu/all_theses/2942

This Thesis is brought to you for free and open access by the Theses at TigerPrints. It has been accepted for inclusion in All Theses by an authorized administrator of TigerPrints. For more information, please contact kokeefe@clemson.edu.

Novel Parallel Continuum Robot Grippers and their Modeling

A Thesis
Presented to
the Graduate School of
Clemson University

In Partial Fulfillment
of the Requirements for the Degree
Master of Science
Electrical Engineering

---

by
Phanideep Satyanarayana Gonthina
August 2018

Accepted by:
Dr. Ian D. Walker, Committee Chair
Dr. Apoorva Kapadia
Dr. Richard E. Groff

Abstract

In this thesis, we propose and investigate a new approach to modeling continuum robot sections, based on Euler spirals. Euler Spirals, also termed Clothoids, or Cornu Spirals, are those curves in which the curvature increases linearly with their arc length. In this work, Euler spirals are applied to the kinematic modeling of continuum robots for the first time. The new approach was tested on two new Parallel Continuum robots - named Mawby and Separating Sections. Mawby - a novel parallel continuum robot gripper featuring a webbing between its continuum fingers was designed and built. Separating Sections - another novel parallel continuum robot could operate as a single section unit, but could also branch out into three separate and distinct units as the situation demanded. Both robots consist of three parallel sections each with three thin, long McKibben actuators. These parallel sections are poorly modeled by the widely used constant curvature kinematic model. The constant curvature and Euler spiral models were compared and the Euler Spiral method was seen to be a significantly better match for the shapes of the robot hardware. An analysis of the underlying causes of non-constant curvature in long continuum robot sections is also presented in the thesis.

Dedication

To Mom and Dad

Acknowledgments

I would first like to thank Dr. Ian D. Walker for all the support, guidance and patience shown to me. I consider myself extremely fortunate to have an advisor such as him.

I would also like to thank Dr. Apoorva Kapadia for his support and guidance throughout my time here at Clemson University.

A special thanks to Dr. Richard Groff for accepting to be on my thesis committee.

I would also like to thank my friends and colleagues from the lab, especially Chase Frazelle and Michael Wooten for all the support throughout my time at Clemson.

Table of Contents

Title Page . . . . . **i**

Abstract . . . . . **ii**

Dedication . . . . . **iii**

Acknowledgments . . . . . **iv**

List of Tables . . . . . **vii**

List of Figures . . . . . **viii**

1 Introduction **1**

2 Novel Biologically Inspired Parallel Continuum Robots **6**
2.1 Construction of Continuum Robot Sections 8
2.2 Separating Sections 10
2.3 Mawby: A Parallel Continuum Gripper with a Webbing 14
2.4 Experiments with Mawby 21

3 Kinematics **29**
3.1 Constant Curvature Kinematic Modeling 29
3.2 Euler Spirals 40
3.3 Plant Curl 45
3.4 Modified Euler Spirals 50

4 Statics **86**
4.1 Underlying Theory 86
4.2 An Observation 93
4.3 Calculation of Forces in a Pneumatic Artificial Muscle 98
4.4 A Second Observation 100

5 Conclusions and Future Work **102**
5.1 Future work 103

Appendices 106

A Matlab Code 107
A.1 Matlab Code for Kinematic Modeling 107
A.2 Matlab Code for Error Calculation 111
A.3 Matlab Code for Resultant Force Calculation 113

Bibliography 115

List of Tables

3.1 Error - Constant curvature kinematics on Mawby section 38
3.2 Error - Constant curvature kinematics on Octarm tip section 39
3.3 Input values for Mawby - Euler spirals 42
3.4 Error Comparison for Mawby - Euler spiral 45
3.5 Input values for Mawby - Plant curl modeling 46
3.6 Error Comparison for Mawby - Plant curl modeling 49
3.7 Input values for Mawby - Modified Euler spirals 51
3.8 Error Comparison for Mawby - Modified Euler spirals 54
3.9 Error Comparison - all methods 55
3.10 Input values for Separating Sections - single muscle actuation 56
3.11 Error Comparison for Separating Sections - single muscle actuation . 60
3.12 Input values for Mawby - 2 muscles with fixed pressure of 9.75 PSI . 61
3.13 Input values for Mawby - 2 muscles with fixed pressure of 13 PSI . . 66
3.14 Input values for Mawby - 2 muscles with fixed pressure of 16.25 PSI . 70
3.15 Input values for Mawby - 2 muscles with same pressure 73
3.16 Input values for Separating Sections - 2 muscles with fixed pressure of 13 PSI 78
3.17 Input values for Mawby - 2D 82
3.18 Error Comparison - single muscle actuation for Mawby - 2D 85

List of Figures

1.1 Elephant trunk 2
1.2 Snake 2
1.3 Soft Robotics Adaptive Gripper 4
1.4 Barrett Hand Gripper 4

2.1 Three fingered gripper from [1] 7
2.2 Continuum robot maneuverability - traversing narrow openings 7
2.3 Top View of a continuum section 10
2.4 Section curving due to differing pressures in the muscles 10
2.5 Squid in prey capture. (Credit - William Kier, University of North Carolina, Chapel Hill) 11
2.6 Cross section view of Separating section design 12
2.7 Fishing line connecting the sections 12
2.8 Separating Sections acting as a single section 12
2.9 Separating Sections acting as a three sections 12
2.10 Separating Sections grasping an object - Initial Position 13
2.11 Separating Sections grasping an object - Opening motion 1 13
2.12 Separating Sections grasping an object - Opening motion 2 13
2.13 Separating Sections grasping an object - Closing motion 13
2.14 Vampire Squid 15
2.15 Octarm tip section 15
2.16 Gear system 17
2.17 Gear system with servo motor 17
2.18 Mawby grasping a stick at 0° orientation 18
2.19 Mawby grasping a stick at 180° orientation 18
2.20 Mawby grasping a box 18
2.21 Mawby grasping a ball with one section 18
2.22 Mawby grasping the large ball with two sections 19
2.23 Mawby grasping the large ball with all three sections 19
2.24 Mawby with the initial webbing design 19
2.25 Mawby with the initial webbing design grasping an object 19
2.26 Mold for the final webbing design 20
2.27 The final webbing design 20
2.28 Mawby in initial position 22

2.29 Mawby curving the sections outward and extending 22
2.30 Mawby getting under the sphere 22
2.31 Mawby picking up the sphere 22
2.32 Mawby picking up a roll of bubble wrap 23
2.33 Mawby picking up a pillow 23
2.34 Mawby picking up a ball 23
2.35 Mawby failing to pick up a box 23
2.36 A single section grasping the bubble-wrap roll 25
2.37 All three sections grasping the object 25
2.38 The first section loses contact with the object 25
2.39 Two sections grasp the bubble-wrap roll 25
2.40 A hoop placed on one section of Mawby at initial location 27
2.41 Transfer of hoop between two Mawby sections 27
2.42 The hoop transfered to another section successfully 27
2.43 Mawby section taking the hoop to final location 27

3.1 Constant curvature kinematics 30
3.2 Mawby - single muscle actuation with 13 PSI pressure 32
3.3 Mawby - single muscle actuation with 16.25 PSI pressure 32
3.4 Mawby - single muscle actuation with 19.5 PSI pressure 32
3.5 Mawby - single muscle actuation with 22.75 PSI pressure 32
3.6 Mawby - single muscle actuation with 26 PSI pressure 32
3.7 Example showing the points selected on the section to generate its line representation 36
3.8 line representation 36
3.9 CC model fit 36
3.10 CC with error 0.0659 meters 36
3.11 CC with error 0.0441 meters 36
3.12 13 PSI with CC model fit 37
3.13 16.25 PSI with CC model fit 37
3.14 19.5 PSI with CC model fit 37
3.15 22.75 PSI with CC model fit 37
3.16 26 PSI with CC model fit 37
3.17 Octarm - 13 PSI with CC model fit 38
3.18 Octarm - 26 PSI with CC model fit 38
3.19 Octarm - 39 PSI with CC model fit 39
3.20 Octarm - 52 PSI with CC model fit 39
3.21 Euler spiral 40
3.22 Euler spiral in roller coaster 40
3.23 Euler modeling. Pressure values (in PSI) in Mawby section muscles 1,2 and 3: 13-0-0 42

3.24 Euler modeling. Pressure values (in PSI) in Mawby section muscles 1,2 and 3: 16.25-0-0 43
3.25 Euler modeling. Pressure values (in PSI) in Mawby section muscles 1,2 and 3: 19.5-0-0 43
3.26 Euler modeling. Pressure values (in PSI) in Mawby section muscles 1,2 and 3: 22.75-0-0 44
3.27 Euler modeling. Pressure values (in PSI) in Mawby section muscles 1,2 and 3: 26-0-0 44
3.28 Plant curl modeling. Pressure values (in PSI) in Mawby section muscles 1,2 and 3: 13-0-0 47
3.29 Plant curl modeling. Pressure values (in PSI) in Mawby section muscles 1,2 and 3: 16.25-0-0 47
3.30 Plant curl modeling. Pressure values (in PSI) in Mawby section muscles 1,2 and 3: 19.5-0-0 48
3.31 Plant curl modeling. Pressure values (in PSI) in Mawby section muscles 1,2 and 3: 22.75-0-0 48
3.32 Plant curl modeling. Pressure values (in PSI) in Mawby section muscles 1,2 and 3: 26-0-0 49
3.33 Modified Euler modeling. Pressure values (in PSI) in Mawby section muscles 1,2 and 3: 13-0-0 51
3.34 Modified Euler modeling. Pressure values (in PSI) in Mawby section muscles 1,2 and 3: 16.25-0-0 52
3.35 Modified Euler modeling. Pressure values (in PSI) in Mawby section muscles 1,2 and 3: 19.5-0-0 52
3.36 Modified Euler modeling. Pressure values (in PSI) in Mawby section muscles 1,2 and 3: 22.75-0-0 53
3.37 Modified Euler modeling. Pressure values (in PSI) in Mawby section muscles 1,2 and 3: 26-0-0 53
3.38 Pressure values (in PSI) in Separating Sections muscles 1,2 and 3: 13-0-0 57
3.39 Pressure values (in PSI) in Separating Sections muscles 1,2 and 3: 16.25-0-0 57
3.40 Pressure values (in PSI) in Separating Sections muscles 1,2 and 3: 19.5-0-0 58
3.41 Pressure values (in PSI) in Separating Sections muscles 1,2 and 3: 26-0-0 58
3.42 Pressure values (in PSI) in Separating Sections muscles 1,2 and 3: 29.25-0-0 59
3.43 Pressure values (in PSI) in Separating Sections muscles 1,2 and 3: 32.5-0-0 59
3.44 Pressure values (in PSI) in Mawby section muscles 1,2 and 3: 13-9.75-9.75 62
3.45 Pressure values (in PSI) in Mawby section muscles 1,2 and 3: 16.25-9.75-9.75 62

3.46 Pressure values (in PSI) in Mawby section muscles 1,2 and 3: 19.5-9.75-9.75 63
3.47 Pressure values (in PSI) in Mawby section muscles 1,2 and 3: 22.75-9.75-9.75 63
3.48 Pressure values (in PSI) in Mawby section muscles 1,2 and 3: 26-9.75-9.75 64
3.49 Pressure values (in PSI) in Mawby section muscles 1,2 and 3: 29.25-9.75-9.75 64
3.50 Pressure values (in PSI) in Mawby section muscles 1,2 and 3: 32.5-9.75-9.75 65
3.51 Pressure values (in PSI) in Mawby section muscles 1,2 and 3: 16.25-13-13 66
3.52 Pressure values (in PSI) in Mawby section muscles 1,2 and 3: 19.5-13-13 67
3.53 Pressure values (in PSI) in Mawby section muscles 1,2 and 3: 22.75-13-13 67
3.54 Pressure values (in PSI) in Mawby section muscles 1,2 and 3: 26-13-13 68
3.55 Pressure values (in PSI) in Mawby section muscles 1,2 and 3: 29.25-13-13 68
3.56 Pressure values (in PSI) in Mawby section muscles 1,2 and 3: 32.5-13-13 69
3.57 Pressure values (in PSI) in Mawby section muscles 1,2 and 3: 19.5-16.25-16.25 70
3.58 Pressure values (in PSI) in Mawby section muscles 1,2 and 3: 22.75-16.25-16.25 71
3.59 Pressure values (in PSI) in Mawby section muscles 1,2 and 3: 26-16.25-16.25 71
3.60 Pressure values (in PSI) in Mawby section muscles 1,2 and 3: 29.25-16.25-16.25 72
3.61 Pressure values (in PSI) in Mawby section muscles 1,2 and 3: 32.5-16.25-16.25 72
3.62 Pressure values (in PSI) in Mawby section muscles 1,2 and 3: 13-13-0 74
3.63 Pressure values (in PSI) in Mawby section muscles 1,2 and 3: 16.25-16.25-0 74
3.64 Pressure values (in PSI) in Mawby section muscles 1,2 and 3: 19.5-19.5-0 75
3.65 Pressure values (in PSI) in Mawby section muscles 1,2 and 3: 22.75-22.75-0 75
3.66 Pressure values (in PSI) in Mawby section muscles 1,2 and 3: 26-26-0 76
3.67 Pressure values (in PSI) in Mawby section muscles 1,2 and 3: 29.25-29.25-0 76
3.68 Pressure values (in PSI) in Mawby section muscles 1,2 and 3: 32.5-32.5-0 77
3.69 Pressure values (in PSI) in Separating Sections muscles 1,2 and 3: 16.25-13-13 79
3.70 Pressure values (in PSI) in Separating Sections muscles 1,2 and 3: 19.5-13-13 79
3.71 Pressure values (in PSI) in Separating Sections muscles 1,2 and 3: 22.75-13-13 80

3.72 Pressure values (in PSI) in Separating Sections muscles 1,2 and 3: 26-13-13 80
3.73 Pressure values (in PSI) in Separating Sections muscles 1,2 and 3: 29.25-13-13 81
3.74 Pressure values (in PSI) in Separating Sections muscles 1,2 and 3: 32.5-13-13 81
3.75 Pressure values (in PSI) in Mawby section muscles 1,2 and 3: 9.75-0-0 82
3.76 Pressure values (in PSI) in Mawby section muscles 1,2 and 3: 11.05-0-0 83
3.77 Pressure values (in PSI) in Mawby section muscles 1,2 and 3: 11.05-0-0 (2) 83
3.78 Pressure values (in PSI) in Mawby section muscles 1,2 and 3: 13-0-0 . 84
3.79 Pressure values (in PSI) in Mawby section muscles 1,2 and 3: 16.25-0-0 84
3.80 Pressure values (in PSI) in Mawby section muscles 1,2 and 3: 19.5-0-0 85

4.1 Two-muscle system representation 88
4.2 Muscle orientations and their forces 89
4.3 Resultant pressure in two muscle plot 91
4.4 Octarm section transition from 0° to 120° 92
4.5 2 muscles with same pressure - observation 94
4.6 Two muscles with 19.5 PSI - data point 3 94
4.7 Two muscles with 22.75 PSI - data point 4 94
4.8 2 muscles with fixed 9.75 PSI - observation 95
4.9 Mawby single muscle actuation - observation 96
4.10 Mawby single muscle actuation - 16.25 PSI 96
4.11 Mawby single muscle actuation - 19.5 PSI 96
4.12 2 muscles with fixed 13 PSI - observation 97
4.13 2 muscles with fixed 16.25 PSI - observation 97
4.14 Single muscle with 16.25 PSI 101
4.15 2 muscles each with 16.25 PSI 101

Chapter 1

Introduction

Continuum robots, which are currently the subject of much research, have a continuous backbone structure. Unlike traditional rigid-link robots which are largely inspired by human (vertebrate) limbs, they lack links and joints (like the elbow). An elephant trunk (Figure 1.1) or a snake (Figure 1.2) is a more representative of the form of a continuum robot element. These robots are usually inspired by nature and many robots which mimic continuum structures seen in nature have been built in recent years. Some of the work inspired by animals includes that by elephant trunks [2], octopus arms [3], snakes [4], and kangaroo tails [5]. Continuum robots have also been in inspired by plants as seen in [6].

Continuum robots have the ability to perform whole-arm grasping which allows them to grasp objects of different shapes by wrapping their body around the objects [7]. [8] introduces the application of shape detection of objects by continuum robots performing whole-arm grasping. The kinematic redundancy of continuum robots, due to the high number of degrees of freedom in their backbones, allows these robots to enter tight spaces and perform tasks that are in some cases impossible for conventional rigid-link robots to perform.

Figure 1.1: Elephant trunk

Figure 1.2: Snake

Continuum and soft robotics have been the subject of rapid developments in the past few years to expand their capabilities in medicine [9], space [10], inspection [11] and other applications. High precision and accuracy is expected from robots especially in the medical field and commercial industry. To achieve this, accurate kinematic and dynamic models for continuum robots are essential. Various kinematics and dynamics modeling approaches have been applied to continuum robots. The constant curvature model [12] is by far the most widely used kinematic model. This model assumes that the continuum structure can be approximated as a serially connected set of constant curvature sections. Chirikjian [13] was the first to introduce a formal method for modeling continuum kinematics and dynamics. His approach uses modal functions to represent the curve shaping function. However, the approach has restrictions on the class of shapes it is able to approximate, due to the modal functions selected. Problems such as singularity in these models were addressed in [14] and a solution via a new kinematic model was presented. Another noteworthy model was by Mochiyama [15] which used the Serret-Frenet formulae to develop the kinematics. A comparative study of five such Kinematic modeling methods - lumped system dynamic model [16], constant curvature [12], two-step modified constant curvature [17], variable curvature kinematics [18] with Cosserat rod and beam theory

approach [19], and series solution identification - is detailed in [20]. The work in [21] proposes a model for a wire driven continuum manipulator with non-constant curvature. While the non-constant curvature modeling approaches, as in [22], have been shown to better approximate the shape of some continuum robot sections, they are significantly computationally complex and non-intuitive, relative to constant curvature modeling. This thesis introduces a new, computationally straightforward and intuitive approach to non-constant curvature modeling of continuum robot sections.

Continuum robots are a specific example of the rapidly emerging class of soft robots, which lack rigid joints and in the case of "pure" soft robots, any rigid parts at all. Although soft robots have been an area of interest in the robotics community, there has not been a soft robot that has really captivated the public interest by means of a product that could be used in industries or homes like the Roomba, Baxter, or other traditional robots with rigid links. Soft robot grippers recently have been able to demonstrate some commercial applications. Grippers by the company Soft Robotics (seen in Figure 1.3) are being used for fruit picking applications where it is required to handle delicate materials; with further advancements proposed in the manufacturing field to operate in unstructured environments and in the e-commerce space to be used in warehouses to manipulate items of various shapes, sizes and weights. The soft robot gripper in [23] was also tested food handling applications. Some other soft multi-fingered robot grippers can be seen in [24], [25], [26] and [27]. The primary purpose of a gripper, analogous to the operation of the fingers of a human hand, is to grasp and interact with objects in the real world. Rigid link robot grippers are generally designed for grasping a limited size and shape of objects. Continuum robots have an advantage here as they not only offer a wider range of object size and shape grasping capabilities, they are also comparatively safer to work with due to their compliant structure. Due to their whole-arm grasping capabilities, they apply

Figure 1.3: Soft Robotics Adaptive Gripper

Figure 1.4: Barrett Hand Gripper

less pressure on the grasped object than their rigid link gripper counterparts, where the force is concentrated on a point or a small area. [28] incorporates sensor skins on soft robotic gripper to measure the deformation and contact. The current state of the art in soft multi-section robot grippers (Figure 1.3) uses relatively short "fingers" operated in an open loop, model-free architecture. In this thesis, we introduce two novel types of multi-(continuum) fingered grippers, each with relatively long thin fingers. We demonstrate how these grippers have novel functionality, and how to model their non-constant curvature kinematics.

Given the lack of research done with continuum fingers, this topic was the initial focus for this thesis. The construction and operation of two such parallel continuum grippers is discussed in Chapter 2. A new robot introduced in this thesis, termed 'Separating Sections' has the ability to transform from a single section to three sections by branching out from its tip to grasp an object. Another robot introduced in this thesis, termed Mawby, an alternative novel approach to multi-(continuum) fingered gripper design, is inspired by the (rigid-link) Barrett Hand design (seen in Figure 1.4). In addition to three continuum finger sections, Mawby has two sections that can rotate 180° in a circular arc while the third section is fixed at the base. This allows Mawby to achieve better orientations to grasp an object. A soft, extensible webbing was also installed on Mawby to aid the grasping process. The two new

hardware designs introduced and analyzed in Chapter 2 represent a new contribution to continuum robot design and grasping.

In Chapter 3 we discuss the inability of the constant curvature model to accurately model the shape and position of the finger sections of either of the new robots introduced in Chapter 2. We consequently propose and analyze a new approach to modeling the kinematics for long, thin continuum sections. We demonstrate the advantages of the new approach, quantitatively confirming its significantly greater accuracy in shape matching compared with the constant curvature model. The new approach to kinematic modeling introduced in this chapter is the first instance in the literature of a purely kinematic approach to non-constant curvature modeling of continuum robot sections.

In Chapter 4 the underlying reasons for the non-constant curvature shaping behavior of the continuum sections Mawby and Separating Sections robots are analyzed and discussed. Different models to predict the forces generated in and by each McKibben actuator and the combination of three such muscles are discussed. The relationship to the Euler spiral model are analyzed. The analysis in this chapter contributes new understanding of the nature of long thin continuum robot sections.

Chapter 2

Novel Biologically Inspired Parallel Continuum Robots

During the course of this research, two different continuum grippers were built. The first - termed 'Separating Sections', was initially designed to investigate the unique problems of parallel continuum robot hardware in terms of grasping and maneuverability. Based on lessons learned with the Separating Sections, another gripper, called 'Mawby' was designed and built. The design and construction of these two continuum grippers, and the experiments conducted, are discussed in this chapter.

Continuum robots offer advanced capabilities compared to conventional rigid-link robots as discussed in [12], [29] and Chapter 1. However there still exists scope for improvements for these robots, particularly related to grasping and manipulation. One such instance can be seen with the Octarm in [30] where the continuum robot holds on to a wooden log and drags it on the ground, instead of lifting and carrying it off the ground. One of the reasons for this is that the Octarm and similar serial continuum robots are incapable to carry heavy loads. In most cases, a single serial continuum robot would not be able lift such an object off of the ground unless holding

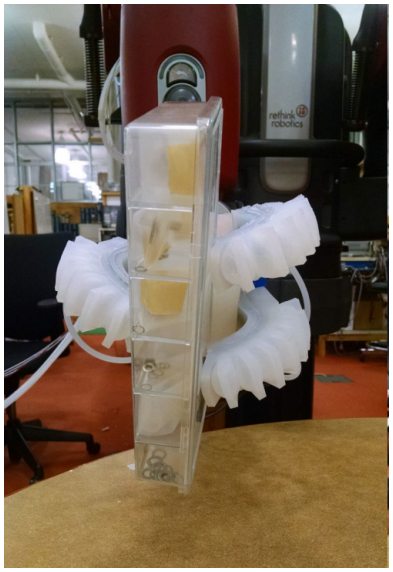

Figure 2.1: Three fingered gripper from [1]

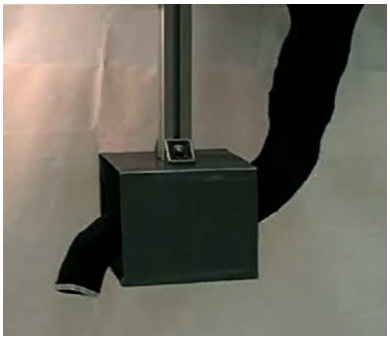

Figure 2.2: Continuum robot maneuverability - traversing narrow openings

it at the center of mass of the object. Another issue that is difficult to tackle is when objects are flat against a surface. In such cases, where the single continuum robot is unable to access the space beneath or otherwise constrain the object, it is incapable of getting a functional grasp of the object.

To overcome the issue of properly grasping objects in a reliable and adaptive manner with parallel continuum robots, soft/continuum robot grippers have been built in [31] and [1]. The work in [31] implements a two-fingered soft gripper and demonstrates a sequence of picking up operations of thin objects from a table. The concept is derived from an analysis of human motion, and proposes picking up a sheet of paper and a plastic card by a robot arm with the simple two-fingered parallel soft gripper. The work reported in [1] implements a three fingered gripper capable of grasping various objects of different sizes and shapes as shown in Figure 2.1. The fingers in both the robots discussed in [31] and [1] are short (high diameter to length ratio, compared to those of the robots considered in this thesis) continuum sections. The dimensions of a manipulator section in [31] and [1] are 8cm x 2.5 cm and 11cm

x 2.5 cm respectively.

While the above mentioned soft robotic grippers address some of the basic issues related to grasping objects, the resulting design precludes an important advantage continuum robots have over their rigid-link counterparts - maneuverability. Robots like the Octarm are designed to access locations conventional rigid-link robots cannot. In surgical and search-and-rescue operations continuum robots need to pass through narrow openings while still being able to maneuver on the other side of the opening. Such applications are represented in Figure 2.2.

The research reported in this chapter tries to address these issues and proposes two novel designs, one termed Separating Sections and the other termed Mawby. Both feature three parallel continuum elements, but differ in the way their sections are arranged. A section herein is defined to be a part of a continuum robot that can operate independently of the rest of the robot as a continuum robot. A Separating Section is defined herein as a parallel combination of multiple sections, combined such that the overall robot can function as single unit, but can also branch out into multiple units when the situation demands it. A unit here is a section and the two words can be used interchangeably.

2.1 Construction of Continuum Robot Sections

A single section of the continuum robots discussed in this thesis consists of three pneumatic McKibben actuators. Also known as 'pneumatic artificial muscles', each McKibben muscle consists of flexible and inflatable membrane inside a braided sleeving. The design and construction of a McKibben actuator muscle is detailed in [32]. To create a continuum robot section, the three muscles are joined together such that the centers of each of the muscles form the vertices of an equilateral triangle. An

example of such a construction is shown in Figure 2.3. Both the robots detailed in the following sections are constructed using this approach and from the same materials. The internal inflatable membrane used was silicone tubing. The selected silicone rubber tubing has an outer diameter of 11.11 mm and an inner diameter of 7.93 mm. The sleeving is made of polyester plastic and has an inner diameter of 9.525 mm and can expand laterally to an inner diameter of 12.7 mm. The sections of the two robots only differ in length and the method in which the three muscles are connected. While the Separating Sections' sections have an average length of 45 cm and the muscles are connected by zip ties, Mawby's sections are about 56 cm each in length and connected with fishing line. As explained in [5] pneumatic muscles can be 'Extenders' which increase in length as a function of increased pressure, or 'Contractors' which decrease in length as a function of increased pressure. In this thesis, extender muscles were built. When pressure is evenly changed in all three actuators of a section, the section length increases or decreases linearly. When different pressures are applied to each of the actuators, the section bends into a curve as shown in Figure 2.4. The plane of the curve is determined by the amount of pressure in each of the three sections, and this phenomenon is detailed in Chapter 4. Thus in general, the section extends, contracts, and changes its curvature and plane of curvature as a function of the applied pressures in each actuator.

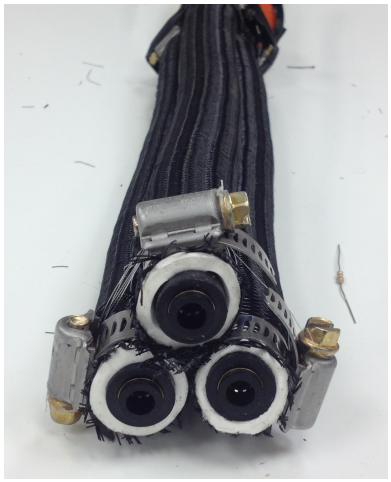

Figure 2.3: Top View of a continuum section

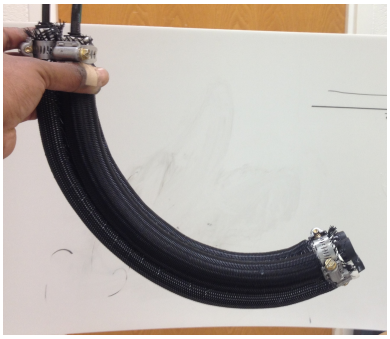

Figure 2.4: Section curving due to differing pressures in the muscles

2.2 Separating Sections

The underlying concept for the Separating Sections was to create a multi-purpose robot, which can operate as a single continuum robot with its three continuum "finger" sections aligned, but also have those fingers "open up" to form a parallel gripper. Motivation is provided by the way the squid deploys its arms and tentacles. See Figure 2.5. The main design challenge was how to achieve the separation of the sections, which was done using fishing wire, as detailed below.

The design of Separating Sections is shown in Figure 2.6. Zip ties were added to muscles 2,3,4,6,7 and 8 and fishing line was passed through these zip ties in a zig-zag fashion as shown in Figure 2.7 to connect the three sections. The loose ends of the fishing line are terminated at the bottom and are fed back through the center of the 3 sections system and taken out from the top to be connected to servo motors. This was done to ensure the fishing line is loosened at the tip, where the sections branch out from, instead of the base.

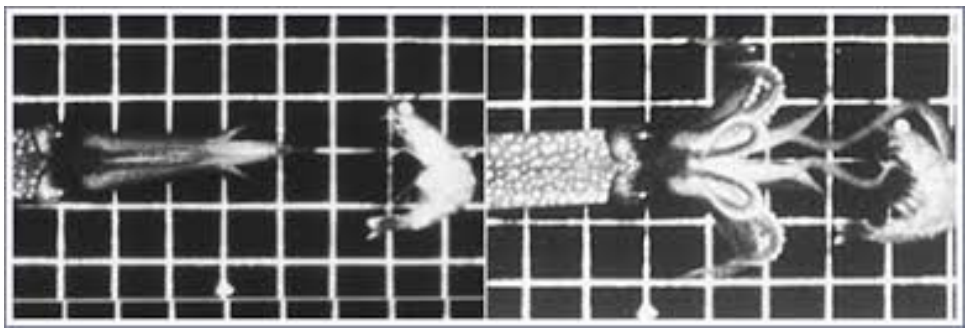

Figure 2.5: Squid in prey capture. (Credit - William Kier, University of North Carolina, Chapel Hill)

When the fishing line is held taut, the sections work as a single unit. The system extends in length when all nine muscles are actuated. When a single section is actuated, the resulting motion mimics that of a three-muscle unit when a single muscle in that unit is actuated as shown in Figure 2.8.

When the fishing line was loosened, the three sections were not held together anymore and can branch out. Figure 2.9 shows all three sections curving outwards. When the system is located directly above the object, the section can open up, hover around the object, and when in reach, the sections can close in and grasp the object. Experiments with the Separating Sections robot performing the grasping movements were conducted and the results of one such experiment can be seen in Figures 2.10-2.13. In Figure 2.10 a ball is placed underneath the Separating Sections within its reach. The fishing line is kept loose for this experiment to facilitate the opening and closing motion of the sections. In Figure 2.11 and 2.12 the opening process of the sections can be clearly seen. The sections also extend in this process which allows them to get underneath the object or get a better grasp from the sides. In Figure 2.13 the section start the closing motion to grasp the object.

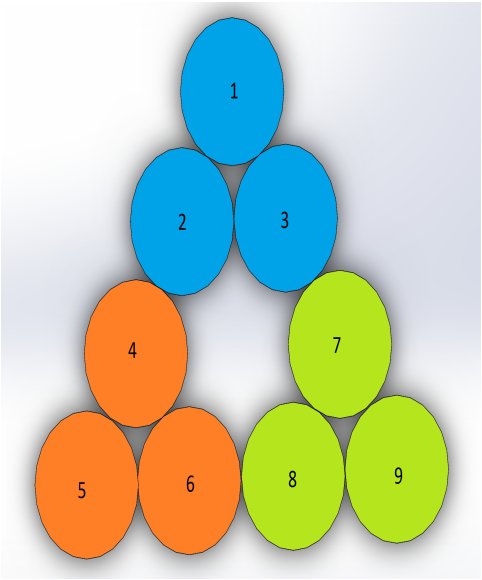

Figure 2.6: Cross section view of Separating section design

Figure 2.7: Fishing line connecting the sections

Figure 2.8: Separating Sections acting as a single section

Figure 2.9: Separating Sections acting as a three sections

Similar experiments with other objects of different size and shapes were conducted with the Separating Sections. However, the Separating Sections manipulator

Figure 2.10: Separating Sections grasping an object - Initial Position

Figure 2.11: Separating Sections grasping an object - Opening motion 1

Figure 2.12: Separating Sections grasping an object - Opening motion 2

Figure 2.13: Separating Sections grasping an object - Closing motion

failed to provide the desired opening and closing mechanism because the fishing line was found to get caught and needed adjustments more often than desired. This gave the rise to the idea of an alternative way of adjusting the relative section positions, along with a webbing-based design which could provide a better option to grasp objects as compared to the Separating Sections on their own to grasp different types of objects.

2.3 Mawby: A Parallel Continuum Gripper with a Webbing

Because of the shortcomings of the Separating Sections, another robot 'Mawby' (also called Mawbot) was designed. 'Maw' means the jaws or throat of a voracious animal, and Mawby was designed using the vampire squid (shown in Figure 2.14) as an inspiration. Note the parallel continuum elements of the squid, and also the webbing connecting its skin, both of which support its dexterous operations.

Three new continuum sections were constructed, similar to the way the Separating Sections were built. In this case, however, the sections were longer than those of the Separating Sections manipulator, and were 56 cm, 55 cm and 58 cm each. To compare the size of these sections with those of a serial continuum robot in our laboratory, the Octarm [33], the tip section of the Octarm (shown in Figure 2.15) has a length-diameter ratio of 6:1 whereas the ratio for the Mawby sections is close to 17:1. This higher length-diameter ratio for Mawby causes it to have a greater curl than the Octarm and also demonstrate a considerably different curvature to the Octarm. The kinematics of these sections was investigated further in the next chapter.

To provide a versatile testbed, Mawby was built with the intention of operating

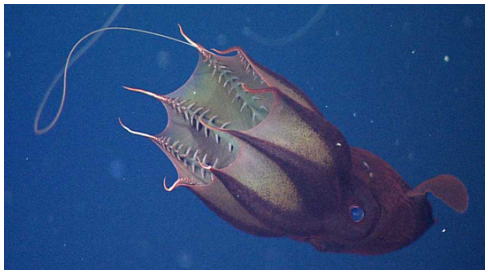

Figure 2.14: Vampire Squid

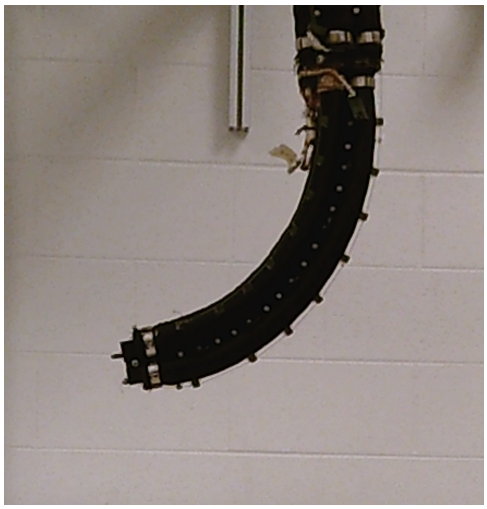

Figure 2.15: Octarm tip section

in two modes - with a webbing and without. In order to be able to grasp a wide range of objects, the design of the robot was inspired by the Barrett Hand (shown in Figure 1.4). In this design there are three robotic fingers. One finger is fixed while the other two can move 180° about the palm of the hand. The configurations to grasp objects can be made with a simple, single degree of freedom design. The design and operation of the Barrett Hand design is given in [34].

To construct a similar capability for Mawby, gears were printed using additive manufacturing (3D Printing) - and assembled as shown in Figure 2.16. A servo motor was attached to the central gear (shown in Figure 2.17) and was able to move the two movable sections 180°. Several configurations of this design are as shown in Figures 2.18-2.23. Figure 2.18 shows Mawby lifting a stick with all three sections on one side

- 0° orientation. Figure 2.19 shows Mawby lifting a stick with a different orientation with two sections on one side and the fixed section on the other - 180° orientation. Objects of different shapes and sizes were also grasped. Figure 2.20 shows Mawby grasping a box, while Figure 2.21 shows Mawby lifting a ball with just one section while the other two sections are free to manipulate the object. Similarly, Figures 2.22 and 2.23 show Mawby grasping a larger ball with two sections and all three sections respectively. A potentiometer was connected to the servo motor and controlled via an Arduino Microcontroller unit, allowing the two sections of the robot to be moved either by the manual rotation of a potentiometer or a computer interface.

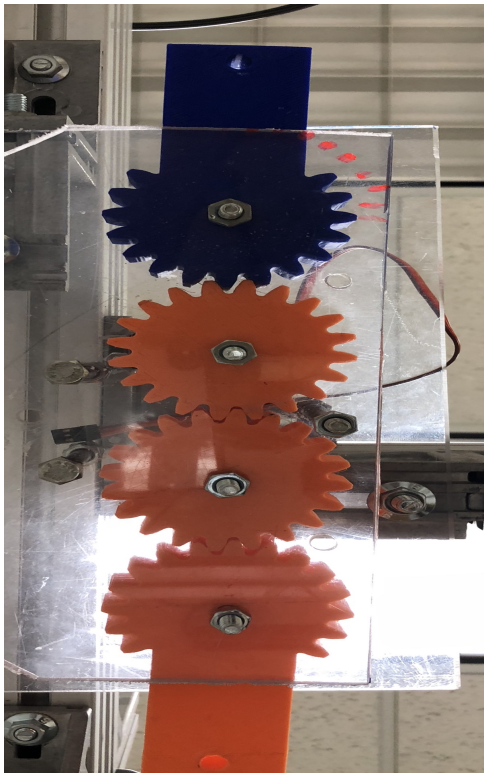

Figure 2.16: Gear system

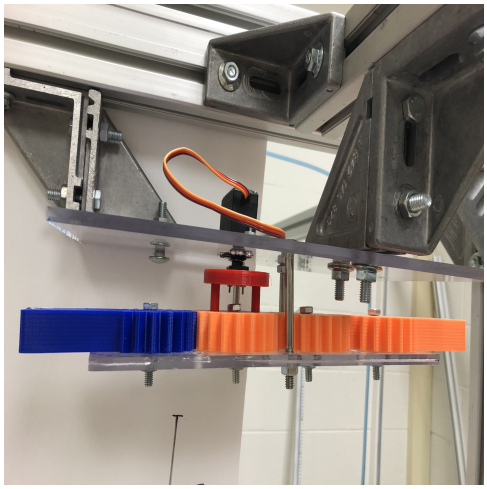

Figure 2.17: Gear system with servo motor

Although Mawby was able grasp various objects, due to its inherent compliant nature of the sections, there were issues where the sections would slip across the object, making it fall in the gap between two sections. A webbing appeared to be

a suitable and novel solution to solve this problem. To be used with the webbing, the sections were arranged 120° apart and two different webbings were added and investigated. Each webbing had to be flexible in order to accommodate a variety of objects. The initial, trial, webbing was created using zip ties and rubber bands, and was mounted on the robot as shown in Figure 2.24. Figure 2.25 shows Mawby grasping the large ball with this webbing design.

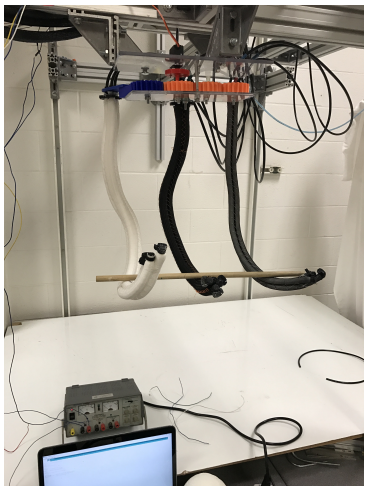

Figure 2.18: Mawby grasping a stick at 0° orientation

Figure 2.19: Mawby grasping a stick at 180° orientation

Figure 2.20: Mawby grasping a box

Figure 2.21: Mawby grasping a ball with one section

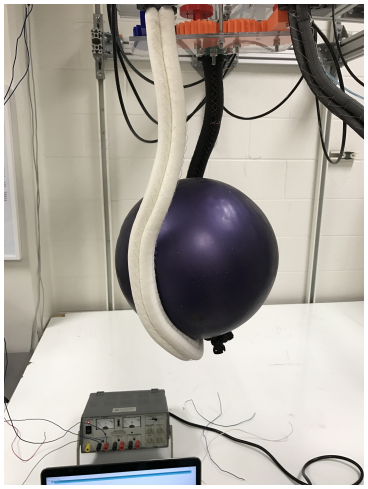

Figure 2.22: Mawby grasping the large ball with two sections

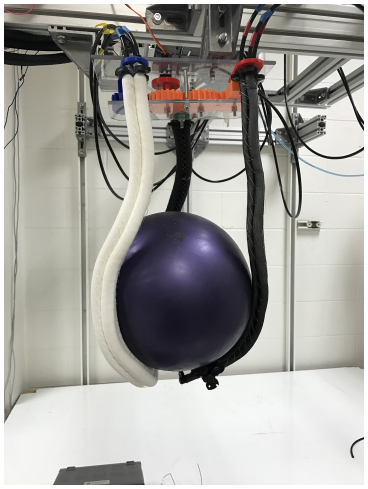

Figure 2.23: Mawby grasping the large ball with all three sections

Figure 2.24: Mawby with the initial webbing design

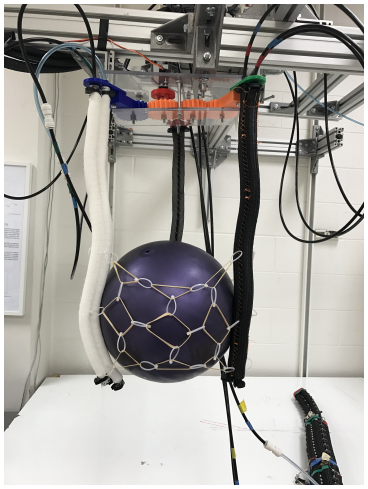

Figure 2.25: Mawby with the initial webbing design grasping an object

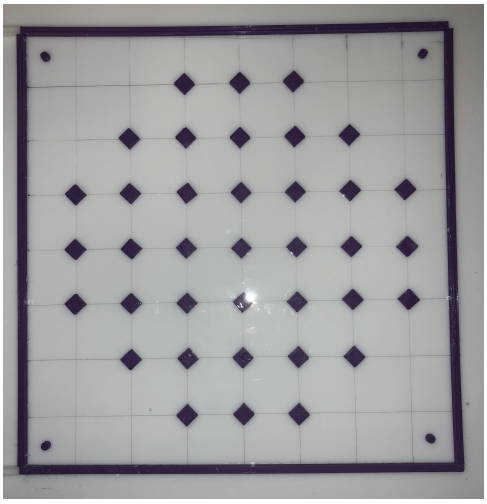

Figure 2.26: Mold for the final webbing design

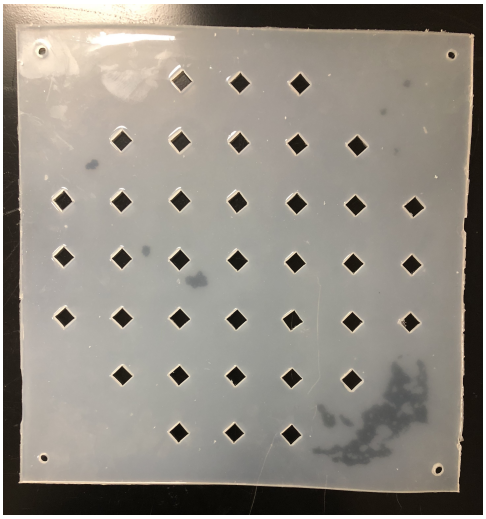

Figure 2.27: The final webbing design

This webbing, however, has its limitations. When the sections curved outward in order to grasp larger objects, the rubber bands were prone to breaking. Additionally, given that rubber bands tend to lose their elasticity over time, this design was not optimal for long term use. Given the limitations of this design, another design using silicone rubber was considered. A mold was created as shown in Figure 2.26 resulting in a mesh-type design in order to allow for some flexibility. Different grades of elasticity of the webbing material were tried - Ecoflex-00-50, 00-30 and Dragon skin from Smooth-On Inc. Ecoflex-00-50 was the softer and lighter of the three materials, and had greater stretching capabilities in comparison to the other two materials, but experienced tearing due to the stretching during the experiments. Dragon skin was the strongest of the three materials but also the heaviest and had the lowest elasticity in comparison to the others. The elasticity of Ecoflex 00-30 fell in between the other two, and ultimately proved the most effective webbing. The effects and capabilities of this new webbing can be seen in Experiment 1 in the next section.

2.4 Experiments with Mawby

2.4.1 Experiment 1

A set of experiments were conducted using Mawby and the new webbing to test its grasping capabilities. Objects of different shapes, sizes and weights were grasped. Grasping of a light spherical object is shown in Figures 2.28-2.31. Figure 2.28 is the initial position when the sphere is placed under the robot. In Figure 2.29 all the sections curve outward and also extend so as to accommodate the sphere, then the sections move beneath it, wrapping it entirely, as shown in in Figure 2.30 and finally the ball is grasped and lifted vertically in Figure 2.31. The same four steps were repeated for different object as seen in Figures 2.32-2.35. Although Mawby was successful in picking up a bubble wrap roll, a small pillow, and a ball, it failed to grasp the particular box shown as it couldn't get under it and the sections simply slid on the sides of the box.

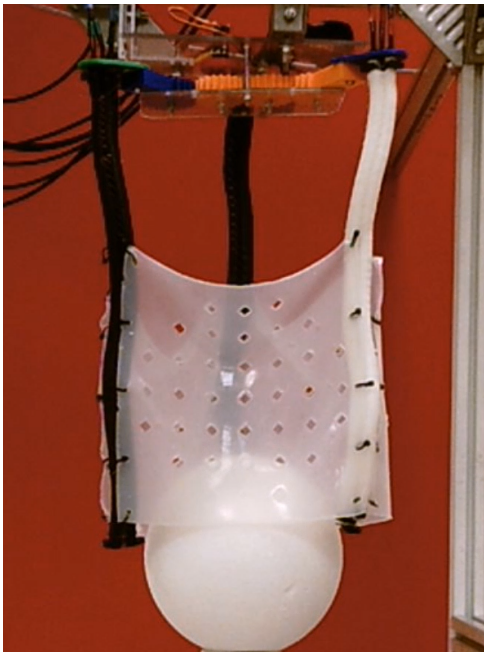

Figure 2.28: Mawby in initial position

Figure 2.29: Mawby curving the sections outward and extending

Figure 2.30: Mawby getting under the sphere

Figure 2.31: Mawby picking up the sphere

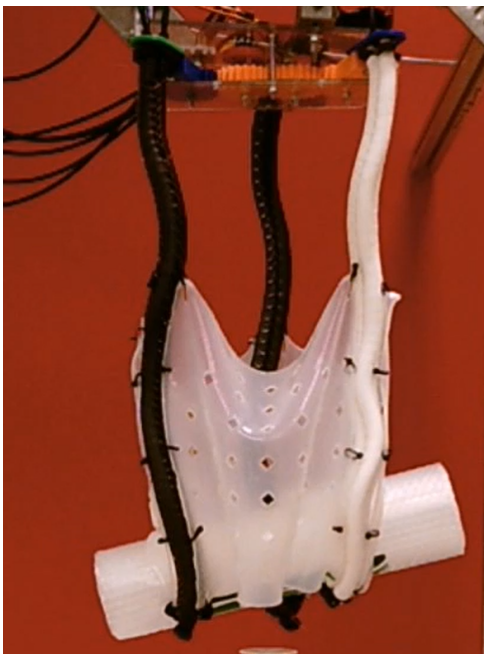

Figure 2.32: Mawby picking up a roll of bubble wrap

Figure 2.33: Mawby picking up a pillow

Figure 2.34: Mawby picking up a ball

Figure 2.35: Mawby failing to pick up a box

2.4.2 Experiment 2

The second experiment involves all three sections and demonstrates the ability of the robot to achieve a more stable grasp. The webbing was removed for this experiment. In Figure 2.36, a cylindrical bubble-wrap roll is held by one section, while the other two sections are at rest. In Figure 2.37, the other sections are actuated and all three sections grasp the object demonstrating a more stable grasp. In Figure 2.38, the first sections loses contact with the object and is completely at rest in Figure 2.39. Thus making the transition from a single section grasp to a two-section grasp.

Figure 2.36: A single section grasping the bubble-wrap roll

Figure 2.37: All three sections grasping the object

Figure 2.38: The first section loses contact with the object

Figure 2.39: Two sections grasp the bubble-wrap roll

2.4.3 Experiment 3

The final experiment demonstrates the ability of the sections to work in coordination with each other to transfer an object from one section to another. The webbing was removed for this experiment and only two sections were used. Figure 2.40 shows a hoop placed on one section at the initial loading position. The transfer of the hoop between two sections can be seen in Figure 2.41. In Figure 2.42 the hoop can be seen to be successfully transfered to the second section. The hoop is then taken to the final location (seen in Figure 2.43) where the loop could be unloaded from the section.

Figure 2.40: A hoop placed on one section of Mawby at initial location

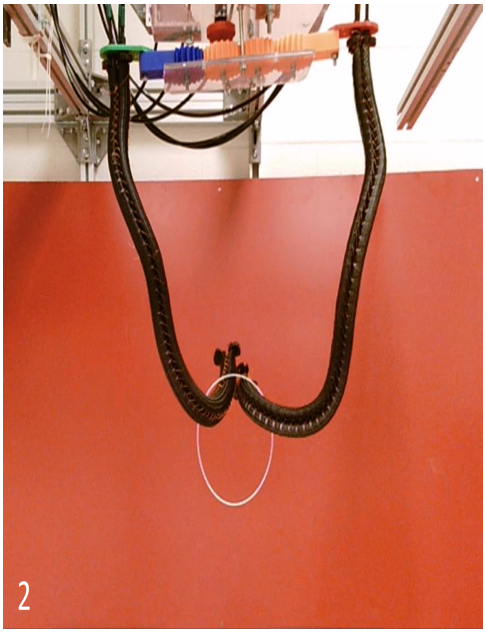

Figure 2.41: Transfer of hoop between two Mawby sections

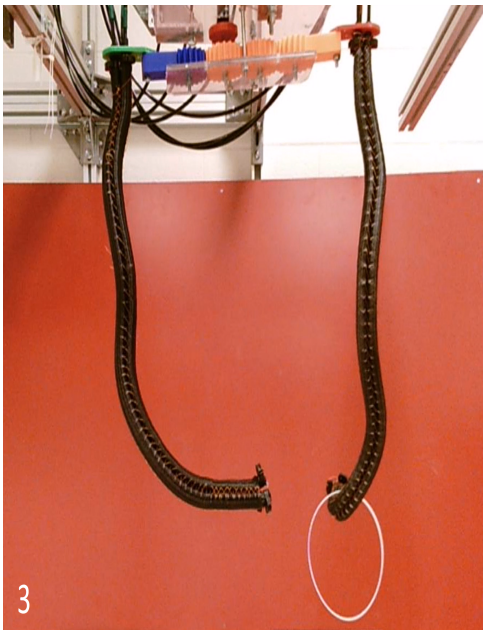

Figure 2.42: The hoop transfered to an other section successfully

Figure 2.43: Mawby section taking the hoop to final location

The robot designs introduced in this chapter represent a new contribution to continuum robot design. The Separating Sections is the first continuum robot that can operate as both an independent serial section and a parallel continuum robot. Mawby is the first parallel continuum robot in which the section base locations can be varied. Additionally, the use of a webbing between parallel sections to aid in grasping is the first instance of this in the robotics literature, to our knowledge.

Experiments with prototype hardware realizations of the designs indicate that they can be highly effective in a variety of novel adaptive grasping operations. However, the reliability of the method used to control the separation of the sections in Separating Sections was poor, motivating future refinement of that design. Similarly, it is expected that efforts in optimizing the shape and materials of the webbing in Mawby will produce even better and more robust results.

One feature common to both robots is the uneven, non-constant, curvature of their sections. This is a function of their long, thin design, which proves effective in grasping. However, it makes their modeling a challenge. This issue is addressed in the following chapters of the thesis.

Chapter 3

Kinematics

In order to analyze and predict the behavior of the continuum robots introduced in Chapter 2, kinematic models are necessary. The unusually long and thin bodies of the sections in these robots preclude the use of the constant curvature model to determine shape, an approach that is the current standard. In this chapter, we introduce a new approach to modeling the kinematics of long continuum sections and support the analysis with experimental validation.

The most commonly used model for continuum robots - the constant curvature model - will be reviewed in Section 3.1. A more accurate model, the Euler spiral approach will be applied in Section 3.2, and subsequent refinements to the Euler spiral model, the new contribution of this chapter, are introduced in the subsequent sections.

3.1 Constant Curvature Kinematic Modeling

Continuum robots are not modeled using the same techniques that are used for rigid-link robots which use joint angles and link lengths of the robot. Arc lengths

and curvatures better describe the shape of a continuum section. Due to the lack of an accurate model for the theoretically infinite degrees of freedom of a continuum structure, a constant curvature approximation has been widely used.

Different models have been used to formulate the constant curvature approximation, as discussed in [29] for example, continuum kinematics via virtual rigid-link kinematics extends the Denavit-Hartenberg (D-H) convention, which is widely used for rigid-link robots, to solve for the tip position by generating the transformation matrix [35], [36].

For a planar continuum section with the orange curved shape as shown in Figure 3.1, the tip position equations are given by Equations 3.1 and 3.2, where, $s \in \mathbb{R}^+$ is the arc length and $k \in \mathbb{R}^+$ is the curvature (given by $1/radius$).

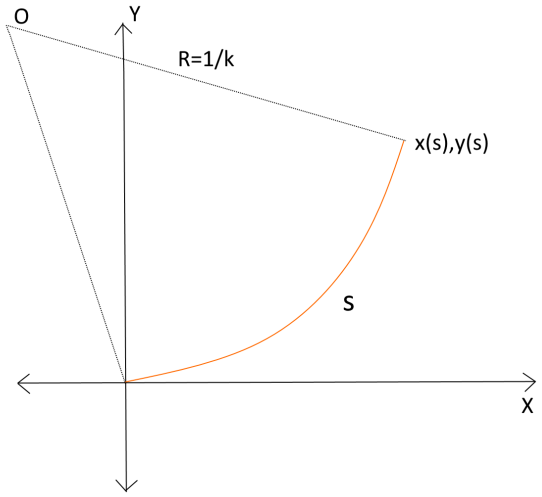

Figure 3.1: Constant curvature kinematics

$$x = (1/k)(cos(sk) - 1) \tag{3.1}$$

$$y = (1/k)sin(sk) \tag{3.2}$$

where $(x \in \mathbb{R}, y \in \mathbb{R})$ is the tip position for a given value of s and k.

To analyze the ability of both constant and non-constant curvature models to fit the continuum robots considered in Chapter 2, numerous images were captured from a fixed camera position of a Mawby section under various pressure values. Five such images can be seen in Figure 3.2 - 3.6 in which only one muscle is pressurized. For the range of $(0, s]$, using Equations 3.1 and 3.2, curves were subsequently matched to the shapes of the Mawby section shown in Figure 3.2 - 3.6.

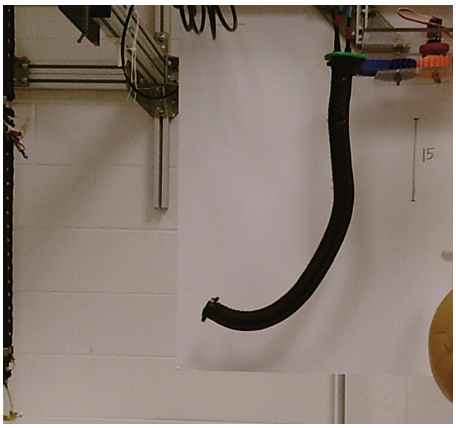

Figure 3.2: Mawby - single muscle actuation with 13 PSI pressure

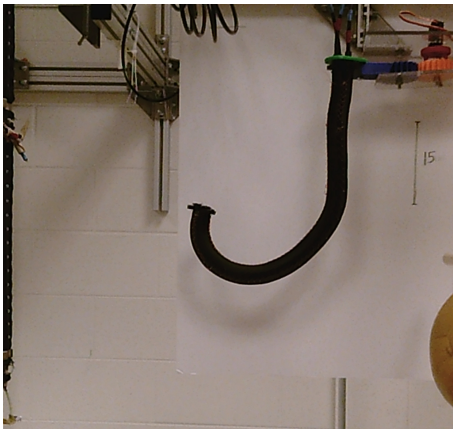

Figure 3.3: Mawby - single muscle actuation with 16.25 PSI pressure

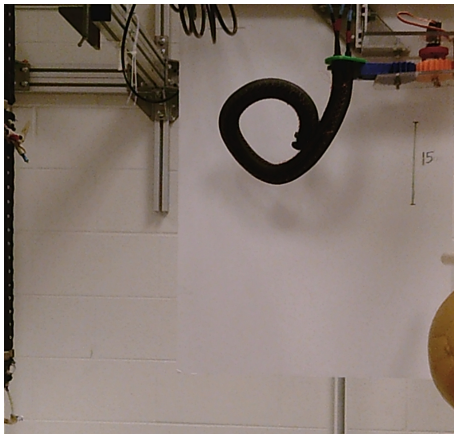

Figure 3.4: Mawby - single muscle actuation with 19.5 PSI pressure

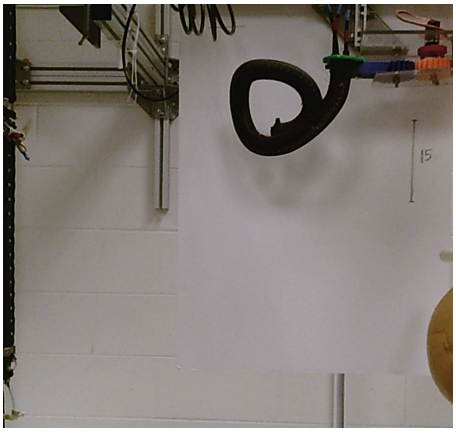

Figure 3.5: Mawby - single muscle actuation with 22.75 PSI pressure

Figure 3.6: Mawby - single muscle actuation with 26 PSI pressure

The procedure to obtain the best fit model for these Mawby curves and the error calculation between these curves is detailed below:

1. Points were selected along the length of curve, starting from the base of the section and ending at the tip of the section, and these points (x and y coordinates) were imported. To obtain the best fit model for these shapes more than 50 points were manually selected on the section in the image (example shown in Figure 3.7).

2. A Matlab code (available in Appendix A.1) was written to generate the non-constant curvature (Euler curve based, as introduced subsequently in this chapter) and constant curvature curves. In the code, Equations 3.1 and 3.2 were used to generate the constant curvature curves and corresponding equations to generate several types of Euler curves (3.7-3.8), (3.10-3.11), (3.17-3.18) are defined later in this chapter. These calculations generate a matrix of x and y coordinate values for increasing arc length (s) values. The values for the arc length and curvature (k) were chosen by trial and error by overlaying the generated Euler curves on the Mawby curve. The s values for the constant curvature equations were initially taken from 0.01 to 0.56 which is the length of the Mawby section in meters. The overlaying of the curves was achieved by using the 'hold on' command in Matlab. The matrix of position coordinates were plotted on the original Mawby curve image.

3. To overlay the generated curve, it was first scaled to fit the Mawby section. This was done since the Mawby curve image was of resolution 3000 x 4000 pixels, so a point on the curve had x and y coordinates, for example, of (1000,500) where 1000 is the vale of the x-coordinate and 500 is the value of y-coordinate. The x and y coordinates generated from the constant curvature and Euler curves were scaled

to fit the Mawby section in the image. All curves generated from a given equation were scaled by the same factor. For example all the coordinates generated from the constant curvature Equations 3.1 and 3.2 were scaled by a factor of 4000 whereas all the coordinates generated by the Euler equations (defined later in the chapter) were scaled by a factor of 2100. These scaling factors were chosen by trial and error to best fit the Mawby curve.

4. The generated coordinates were then translated and rotated to fit the Mawby section curve. For translation, all the scaled x and y coordinates were first subtracted by the value of the first point in the same generated coordinates such that the value of the first point becomes (0,0). The value of the first point in the Mawby section curve (selected in Step 1) was then added to all the points in the generated curve coordinates such that the first point in the generated curve coordinates becomes the same as the first point in the selected Mawby curve section coordinates. To align with the Mawby section curve, these scaled and translated coordinates generated were then rotated, by an angle θ using a rotation matrix R (Equation 3.3) and new coordinates were obtained using Equation 3.4. The value of the angle θ to be rotated was calculated using trial and error.

$$R(\theta) = \begin{bmatrix} cos(\theta) & -sin(\theta) \\ sin(\theta) & cos(\theta) \end{bmatrix} \tag{3.3}$$

$$x_{new} = R(\theta)x \tag{3.4}$$

5. To calculate the error between the generated curve and Mawby section

curve, the Euclidean distance between each point selected in Step 1 and the point closest to it in the generated Euler curve was calculated.

6. The root-mean-square value of the error values for each point selected in Step 1 was calculated.

7. Using the calibration line in the image background, it was known that 510 pixels in the image corresponds to 15cm in the real world. Using this conversion factor, an error value in centimeters and thereby an error value in meters was obtained. For example, Figure 3.10 has an error value of 0.0659 m while Figure 3.11 has an error value of 0.0441 m. In this way we can conclude numerically that the constant curvature model fit shown in Figure 3.11 is a better fit for the given Mawby curve.

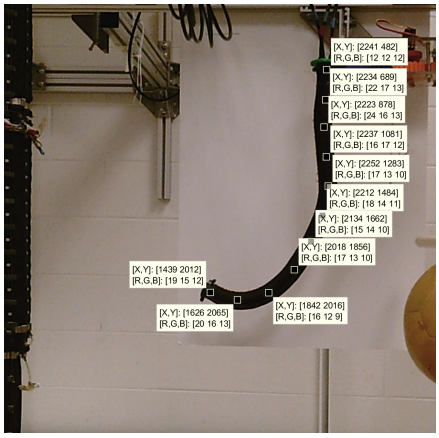

Figure 3.7: Example showing the points selected on the section to generate its line representation

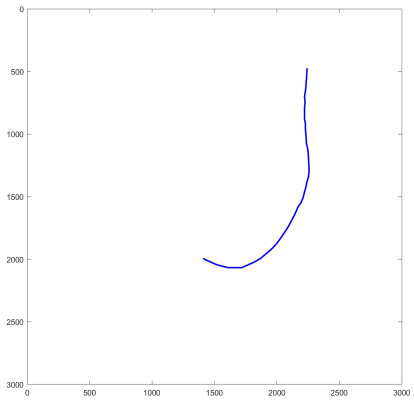

Figure 3.8: line representation

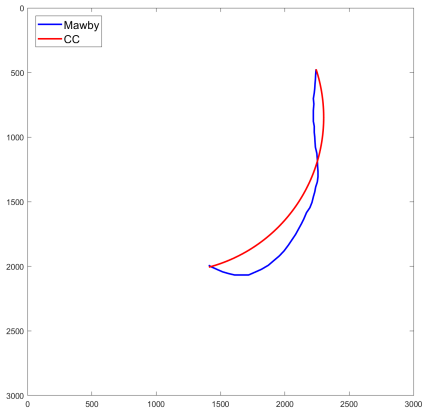

Figure 3.9: CC model fit

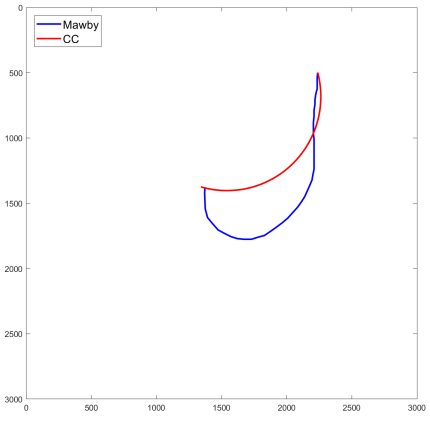

Figure 3.10: CC with error 0.0659 meters

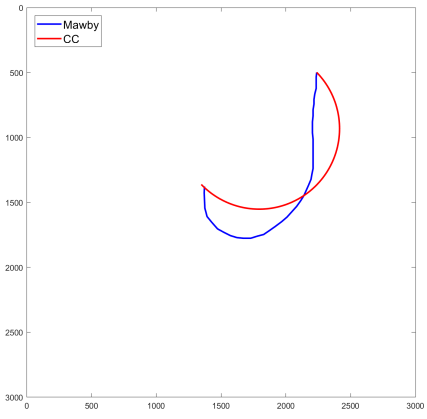

Figure 3.11: CC with error 0.0441 meters

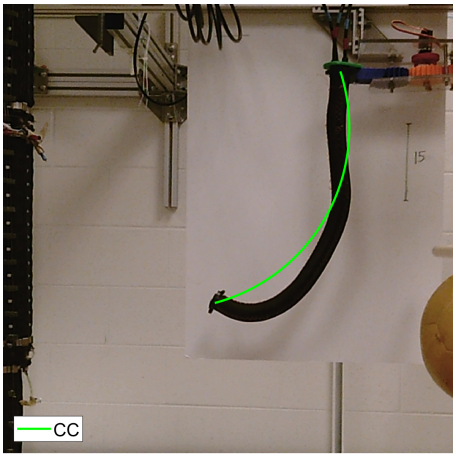

Figure 3.12: 13 PSI with CC model fit

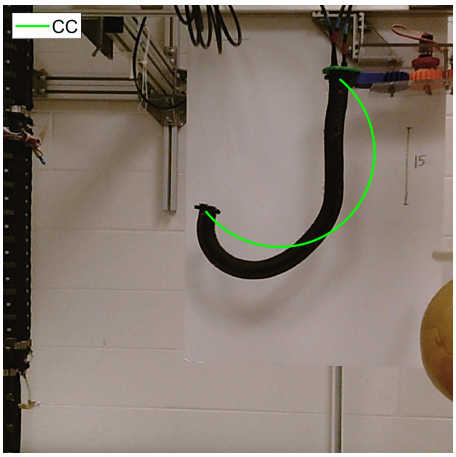

Figure 3.13: 16.25 PSI with CC model fit

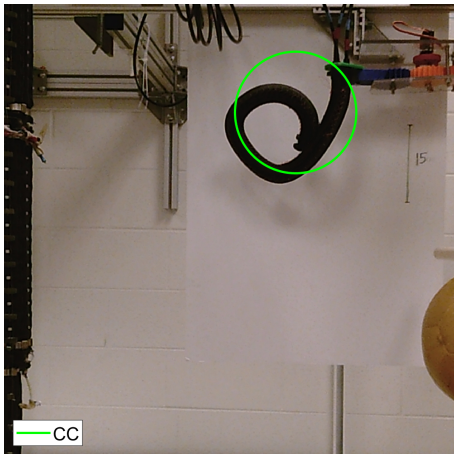

Figure 3.14: 19.5 PSI with CC model fit

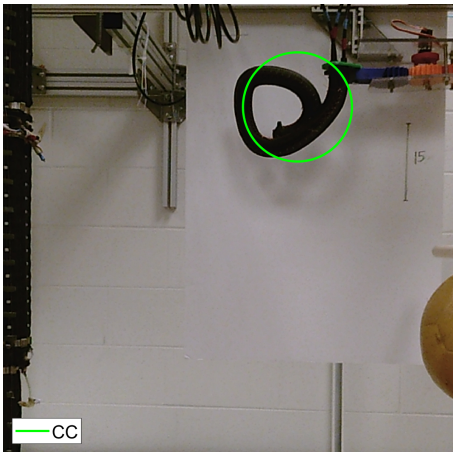

Figure 3.15: 22.75 PSI with CC model fit

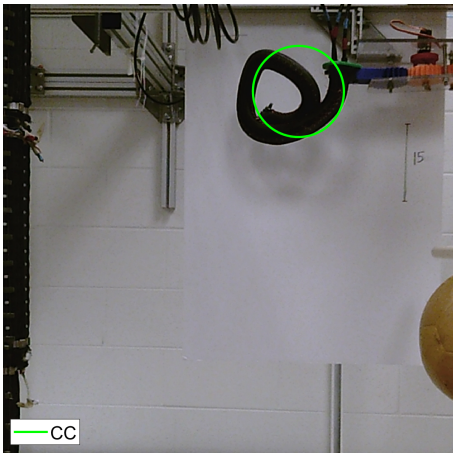

Figure 3.16: 26 PSI with CC model fit

The error value (in meters) for the various Mawby curves can be seen in Table 3.1.

Pressure (PSI)	13	16.25	19.5	22.75	26
error(meters)	0.0892	0.05	0.0443	0.0388	0.0389

Table 3.1: Error - Constant curvature kinematics on Mawby section

To better interpret these error values, the constant curvature model was applied to tip section of the Octarm, and the results were compared. Figures 3.17-3.20 show the Octarm actuated at varying pressure values and the constant curvature model fit. The results of the calculated error values are shown in Table 3.2.

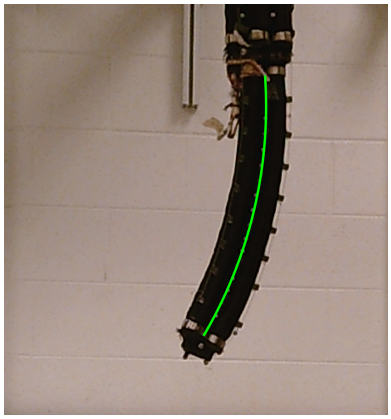

Figure 3.17: Octarm - 13 PSI with CC model fit

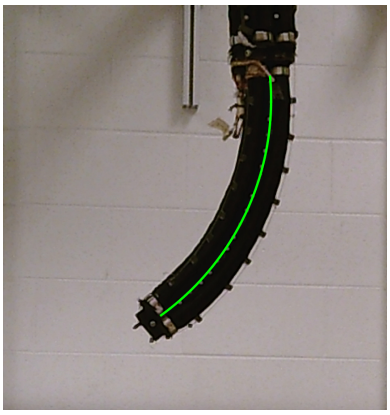

Figure 3.18: Octarm - 26 PSI with CC model fit

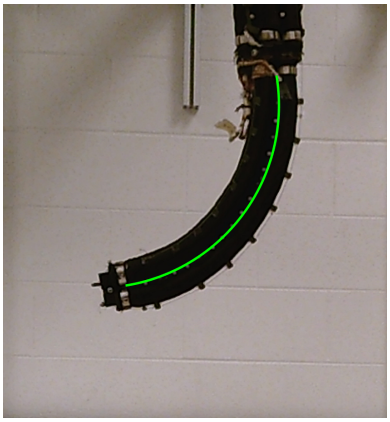

Figure 3.19: Octarm - 39 PSI with CC model fit

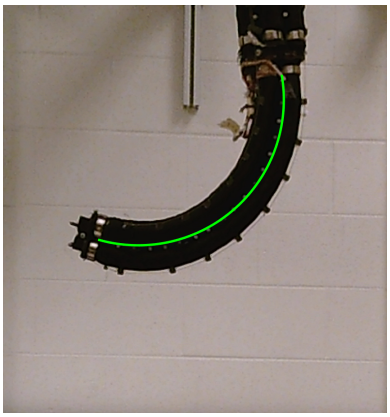

Figure 3.20: Octarm - 52 PSI with CC model fit

Pressure (PSI)	13	26	39	52
error(meters)	0.002	0.0018	0.0033	0.0038

Table 3.2: Error - Constant curvature kinematics on Octarm tip section

Due to the shape discrepancies clearly visible in the constant curvature images for Mawby sections (Figures 3.12 - 3.16), reflected in the comparison with the Octarm tip section results to be high error values for constant curvature kinematics, there is a clear need for a better model.

3.2 Euler Spirals

The Euler spiral, also termed the Clothoid spiral, is a curve whose curvature is linearly proportional to its arc length (shown in Figure 3.21). They are widely used in railroads as transition curves (to transition from straight segments to circular curves). They are also used in Optics and roller coaster construction as shown in Figure 3.22. A clothoid approximation technique and its application in path planning application is detailed in [37].

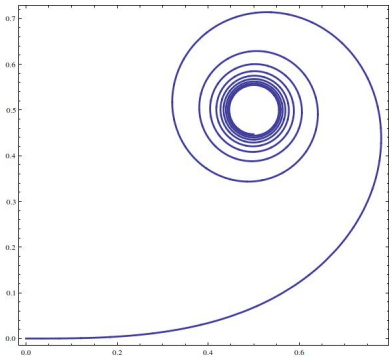

Figure 3.21: Euler spiral

Figure 3.22: Euler spiral in roller coaster

For their underlying theoretical application on elastic materials as stated in [38], and their visual resemblance to the curves that the Mawby section generates, Euler spirals were investigated further. Curvature $k \in \mathbb{R}^+$ linearly increasing with the arc length $s \in \mathbb{R}^+$ gives us the equations shown below.

$$k = rs \tag{3.5}$$

where $r \in \mathbb{R}$ is a constant.

$$s/k = r \tag{3.6}$$

Substituting k by s/r in Equations 3.1 and 3.2, Euler curve equations were

generated as follows:

$$x = (r/s)cos(s^2/r) \tag{3.7}$$

$$y = -(r/s)sin(s^2/r) \tag{3.8}$$

Using Equations 3.7 and 3.8, Euler curves were generated to approximate the Mawby section curves and their corresponding comparisons with an example set of constant curvature curves can be seen in Figure 3.23-3.27.

The Euler curves were numerically calculated by integrating Equations 3.7 and 3.8. Due to the r/s multiplication factor in these equations, the range $(0, s]$ generates an amplified result for lower values of the arc length resulting in longer than desired initial straight (low curvature) segments. Changing the limits of the integral from $(0, s]$ to $[s_1, s_2]$ allows the selection of different parts of the Euler curve, which will be needed to remove these low curvature segments to better fit the Mawby section curves, as detailed in subsequent sections. The percentage error decrease is calculated by the formula in Equation 3.9.

$$\%error = (\frac{e1 - e2}{e1})100 \tag{3.9}$$

The input parameters for each curve in the example sets are seen in Table 3.3 and the corresponding comparisons can be seen in Figures 3.23-3.27.

Pressure (PSI)	r	s_1	s_2
13	0.092	0.014	0.56
16.25	0.072	0.14	0.57
19.5	0.044	0.16	0.6
22.75	0.042	0.19	0.62
26	0.04	0.2	0.635

Table 3.3: Input values for Mawby - Euler spirals

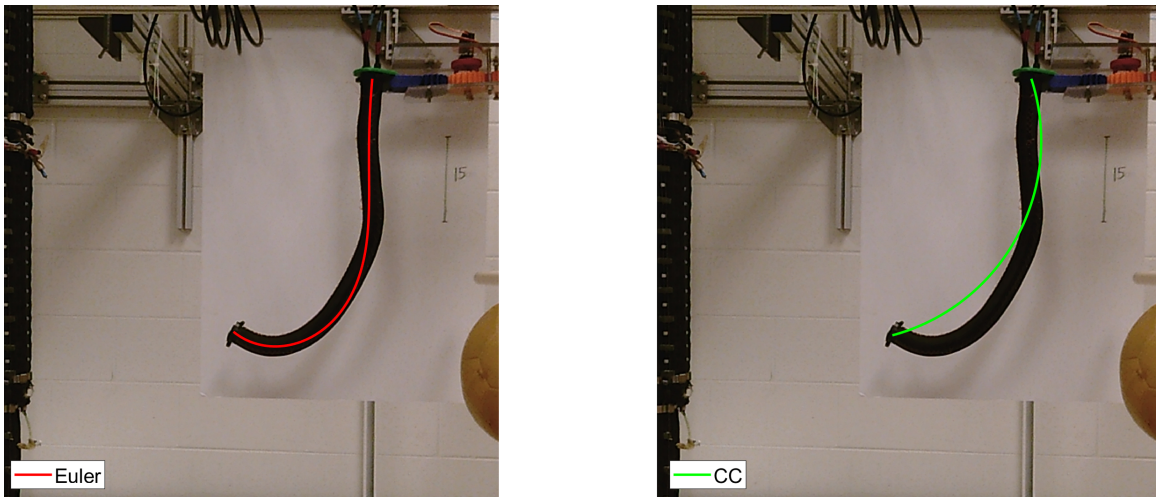

Figure 3.23: Euler modeling. Pressure values (in PSI) in Mawby section muscles 1,2 and 3: 13-0-0

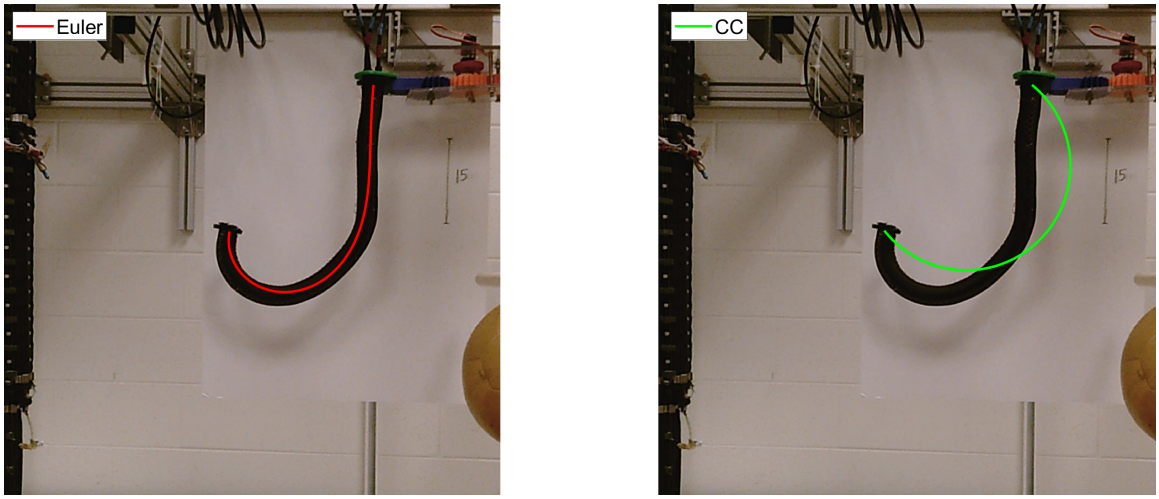

Figure 3.24: Euler modeling. Pressure values (in PSI) in Mawby section muscles 1,2 and 3: 16.25-0-0

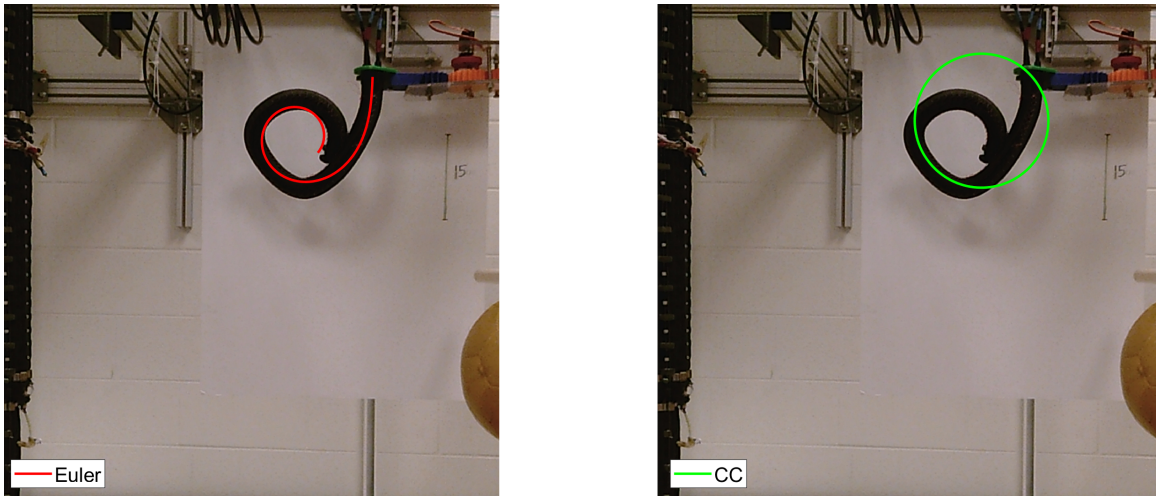

Figure 3.25: Euler modeling. Pressure values (in PSI) in Mawby section muscles 1,2 and 3: 19.5-0-0

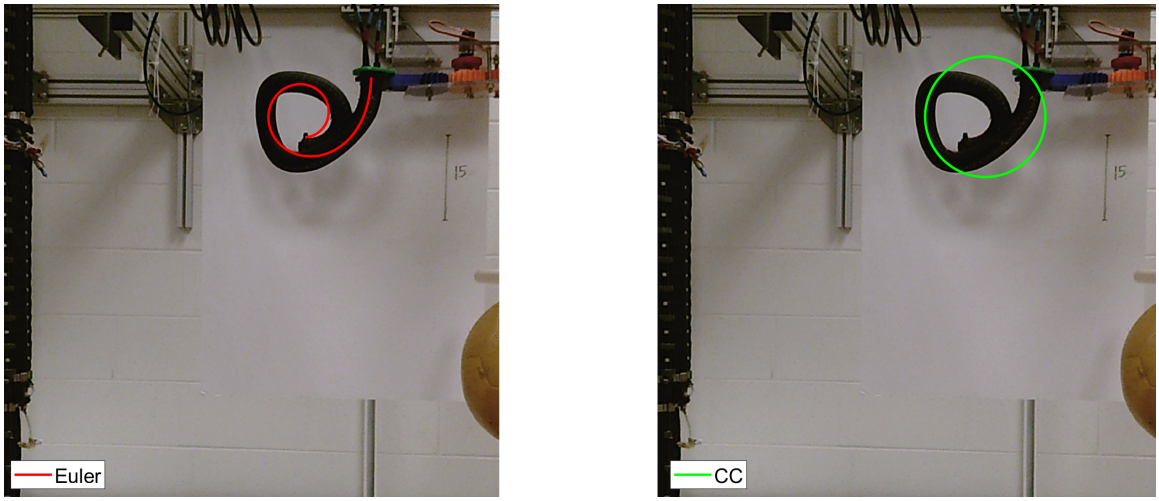

Figure 3.26: Euler modeling. Pressure values (in PSI) in Mawby section muscles 1,2 and 3: 22.75-0-0

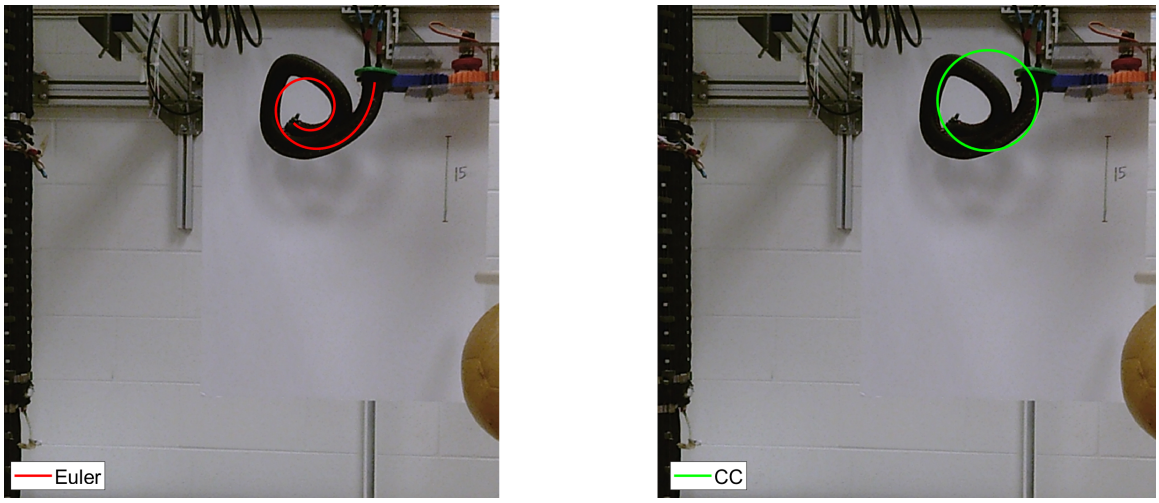

Figure 3.27: Euler modeling. Pressure values (in PSI) in Mawby section muscles 1,2 and 3: 26-0-0

Pressure (PSI)	CC error e1 (in m)	Euler error e2 (in m)	Percent error decrease
13	0.0892	0.0061	93.16
16.25	0.05	0.0059	88.2
19.5	0.0443	0.0124	72.01
22.75	0.0388	0.0126	67.53
26	0.0389	0.0109	71.98

Table 3.4: Error Comparison for Mawby - Euler spiral

Comparison of the Euler spiral model to the constant curvature model is seen in Table 3.4. It can be seen from Table 3.4 that the Euler spiral modeling is a significant improvement over the constant curvature modeling.

3.3 Plant Curl

The Euler spiral curves generated in the previous section are significantly closer to the robot shape, however, alternative approaches to Euler curve generation were investigated. Euler curves were generated as explained in [39], shown in equations 3.10 and 3.11.

$$x = \sqrt{\pi/r}sin(s^2) \tag{3.10}$$

$$y = \sqrt{\pi/r}cos(s^2) \tag{3.11}$$

where,

$$r = \sqrt{a} \tag{3.12}$$

$$k = as \tag{3.13}$$

By taking r as a variable, with an initial r value (r_1), the final r value (r_2) was found by Equation 3.14, where $\lambda \in \mathbb{R}$ and $\alpha \in \mathbb{R}$.

$$r_2 = r_1 + \alpha(s_2 - s1)/\lambda \tag{3.14}$$

Using the input parameters as shown in Table 3.5, the comparison plots, shown in Figure 3.28-3.32, were generated.

Pressure (PSI)	r_1	r_2	s_1	s_2	λ	α
13	0.11	0.93	0.74	1.87	0.0029	0.004
16.25	0.17	1.61	0.74	2.18	0.004	0.004
19.5	0.6	2.66	0.74	2.8	0.004	0.004
22.75	0.85	3.11	0.74	3	0.004	0.004
26	1	5.13	0.74	3.1	0.007	0.004

Table 3.5: Input values for Mawby - Plant curl modeling

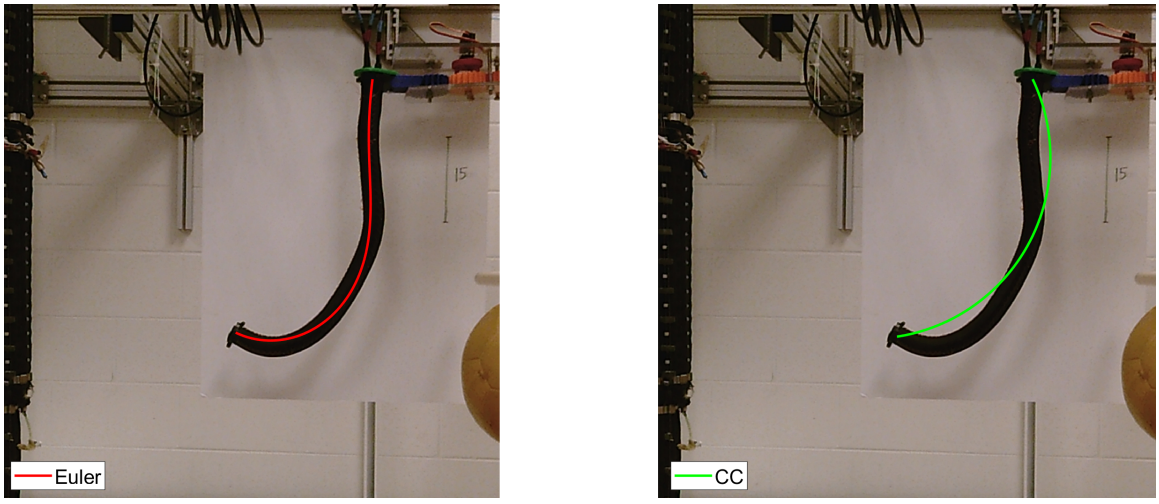

Figure 3.28: Plant curl modeling. Pressure values (in PSI) in Mawby section muscles 1,2 and 3: 13-0-0

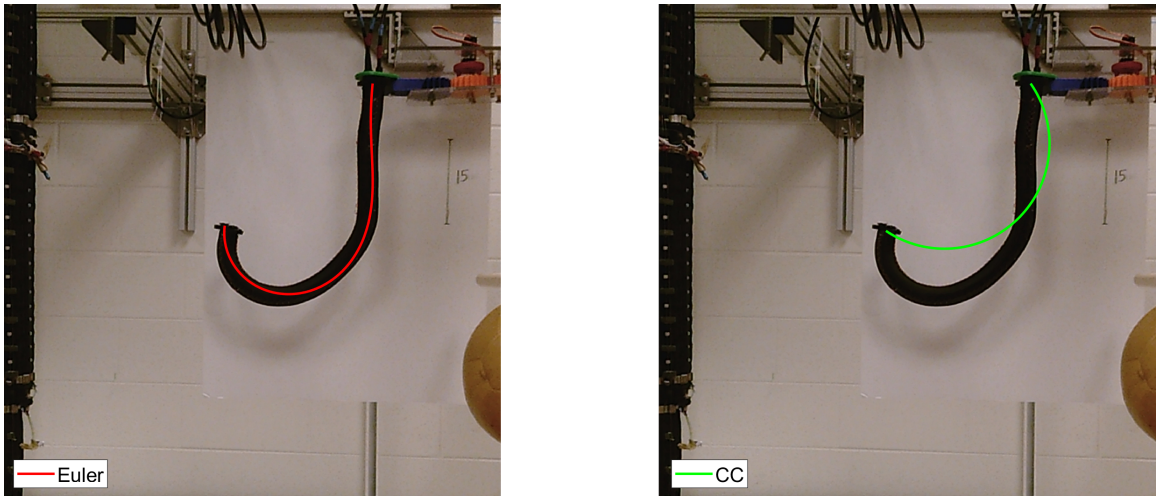

Figure 3.29: Plant curl modeling. Pressure values (in PSI) in Mawby section muscles 1,2 and 3: 16.25-0-0

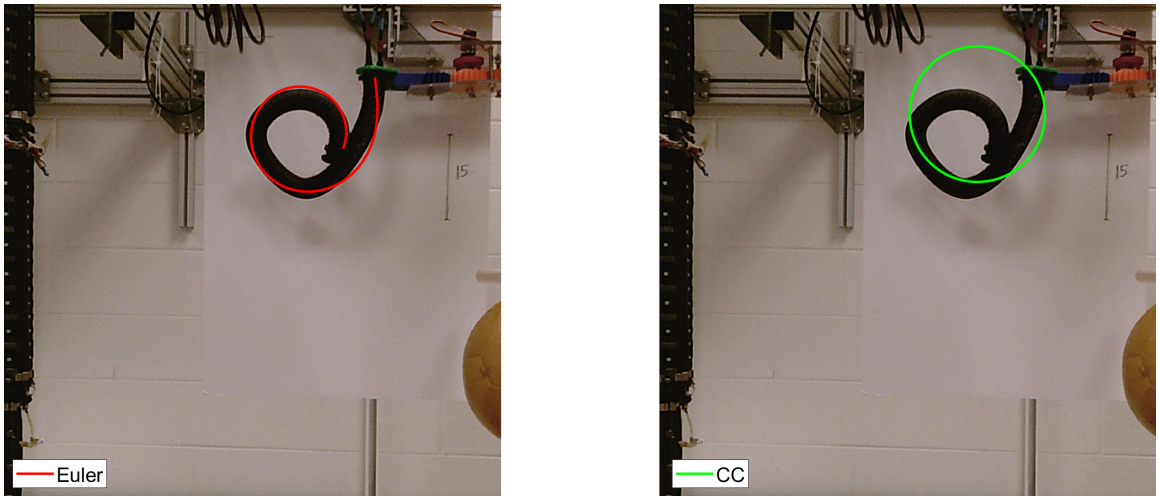

Figure 3.30: Plant curl modeling. Pressure values (in PSI) in Mawby section muscles 1,2 and 3: 19.5-0-0

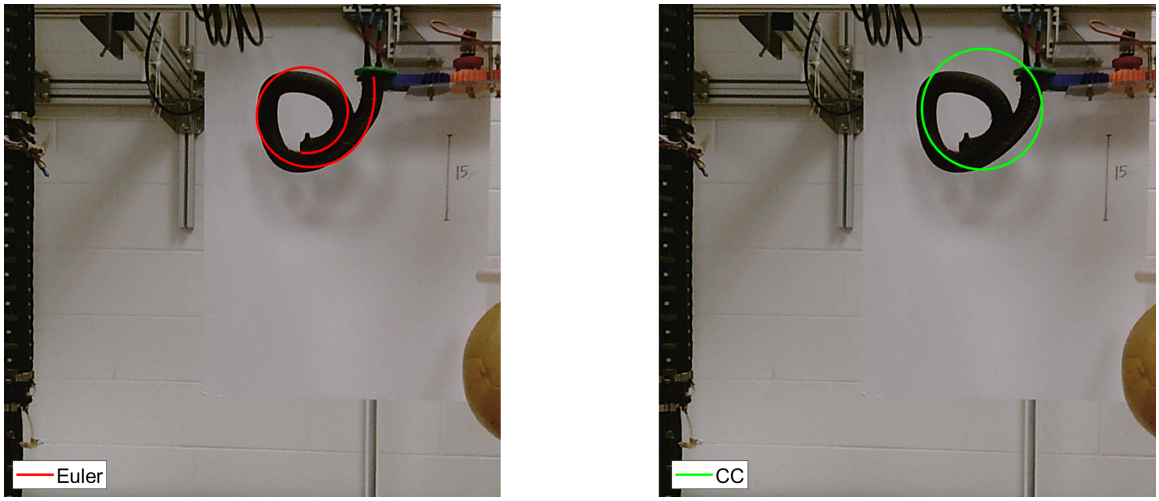

Figure 3.31: Plant curl modeling. Pressure values (in PSI) in Mawby section muscles 1,2 and 3: 22.75-0-0

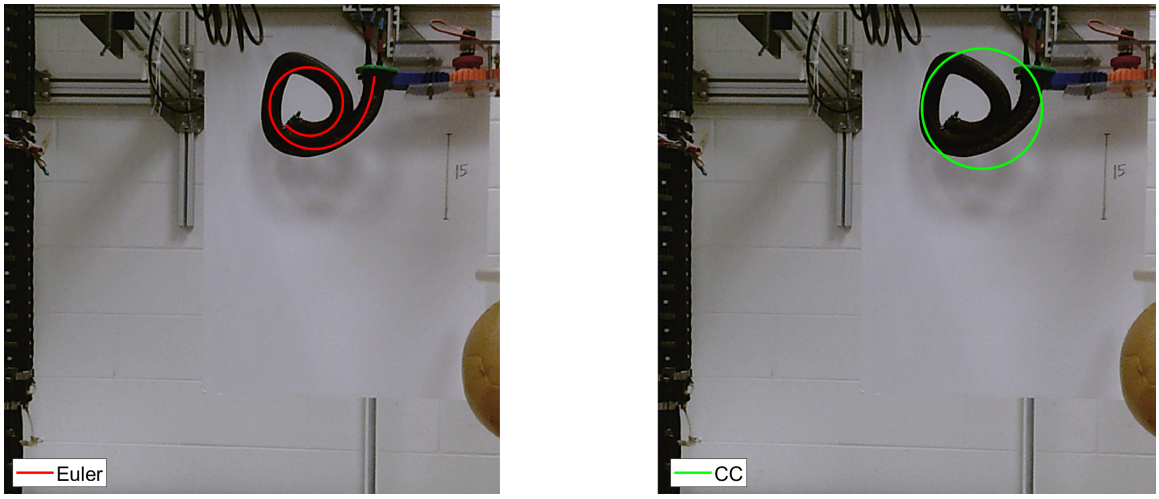

Figure 3.32: Plant curl modeling. Pressure values (in PSI) in Mawby section muscles 1,2 and 3: 26-0-0

Pressure (PSI)	CC error e1 (in m)	Plant curl error e2 (in m)	Percent error decrease
13	0.0892	0.0058	93.5
16.25	0.05	0.0056	88.8
19.5	0.0443	0.0156	64.79
22.75	0.0388	0.0144	62.89
26	0.0389	0.0062	84.06

Table 3.6: Error Comparison for Mawby - Plant curl modeling

It can be seen from Table 3.6 that the Plant Curl variation of Euler spiral modeling was similar in accuracy than the Euler spiral modeling seen in Section 3.2. It was evident that varying the value of r yielded slightly better results for few cases. Hence the effect of varying r values in the Euler spiral equations was investigated and their results are discussed in the next section.

3.4 Modified Euler Spirals

By using the equations from Euler spirals section (3.2), and varying the r value as in the Plant curl section (3.3), the input values shown in Table 3.7 generated the results shown in Figures 3.33-3.37. The values for r_2 were calculated by using the Equation 3.19

$$k = rs \tag{3.15}$$

$$s/k = r \tag{3.16}$$

Substituting k by s/a in equations 1.1 and 1.2 generates Euler curve equations:

$$x = (r/s)(cos(s^2/r) - 1) \tag{3.17}$$

$$y = (r/s)sin(s^2/r) \tag{3.18}$$

$$r_2 = r_1 - \alpha(s_2 - s1)/\lambda \tag{3.19}$$

Pressure (PSI)	r_1	r_2	s_1	s_2	λ	α
13	1.26	0.314	0.01	0.565	0.0068	0.004
16.25	1.1	0.14	0.01	0.5	0.007	0.004
19.5	0.048	0.0362	0.38	0.615	0.0002	0.004
22.75	0.04	0.0288	0.38	0.58	0.000224	0.004
26	0.04	0.0249	0.39	0.56	0.00035	0.004

Table 3.7: Input values for Mawby - Modified Euler spirals

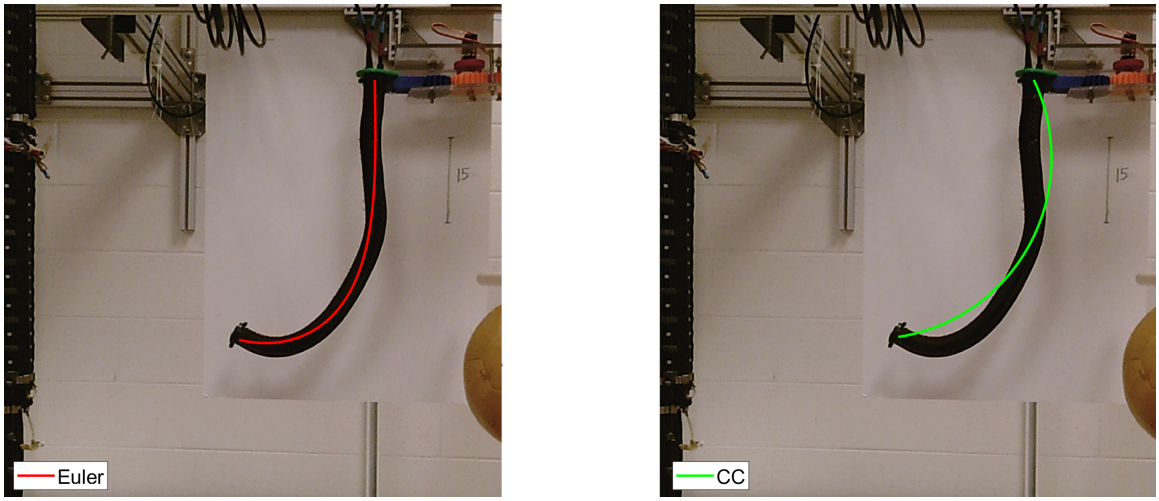

Figure 3.33: Modified Euler modeling. Pressure values (in PSI) in Mawby section muscles 1,2 and 3: 13-0-0

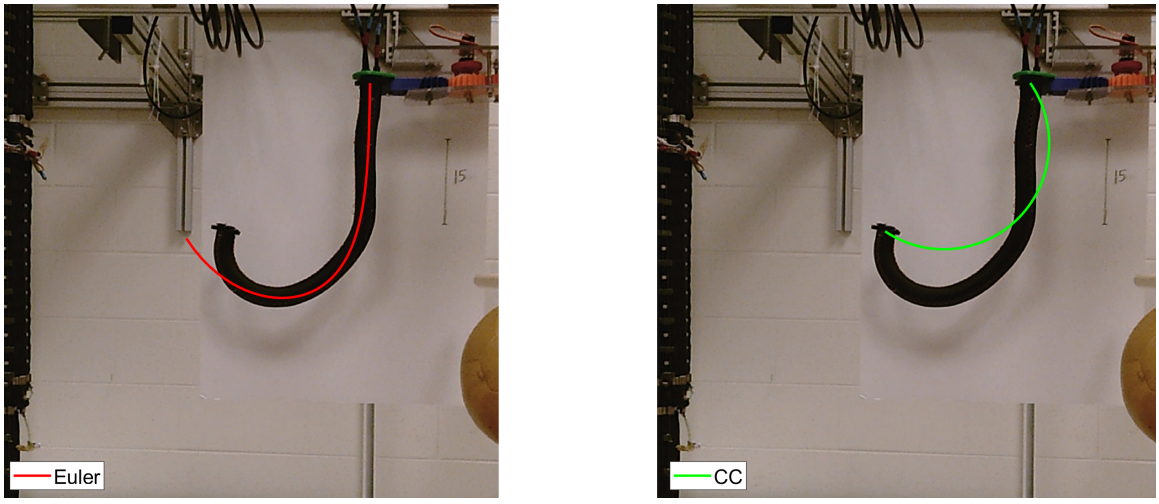

Figure 3.34: Modified Euler modeling. Pressure values (in PSI) in Mawby section muscles 1,2 and 3: 16.25-0-0

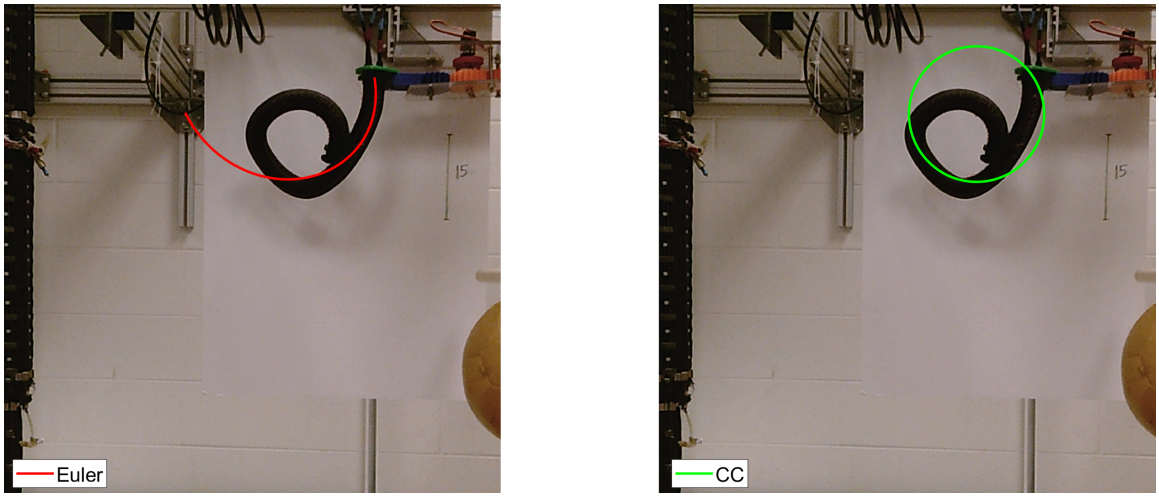

Figure 3.35: Modified Euler modeling. Pressure values (in PSI) in Mawby section muscles 1,2 and 3: 19.5-0-0

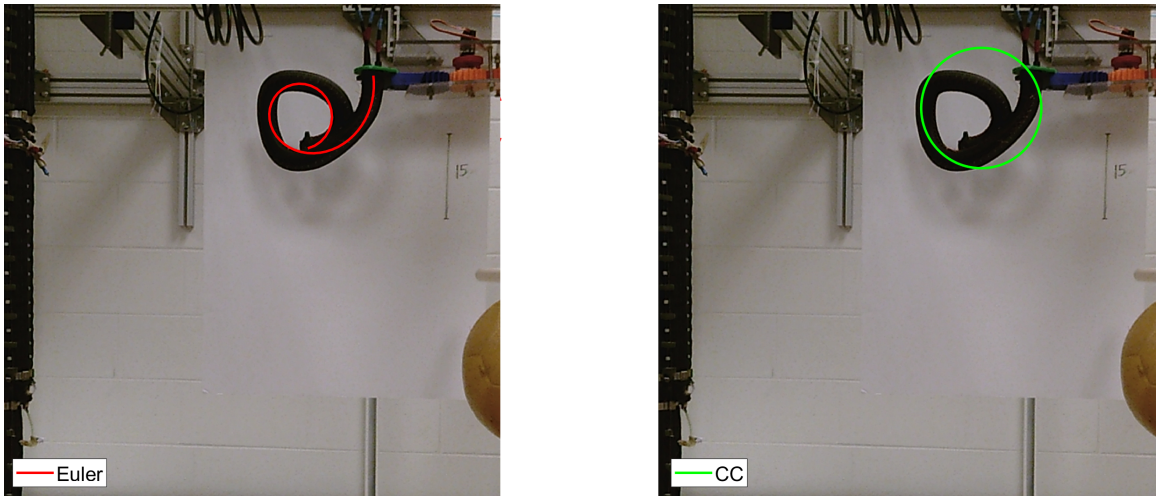

Figure 3.36: Modified Euler modeling. Pressure values (in PSI) in Mawby section muscles 1,2 and 3: 22.75-0-0

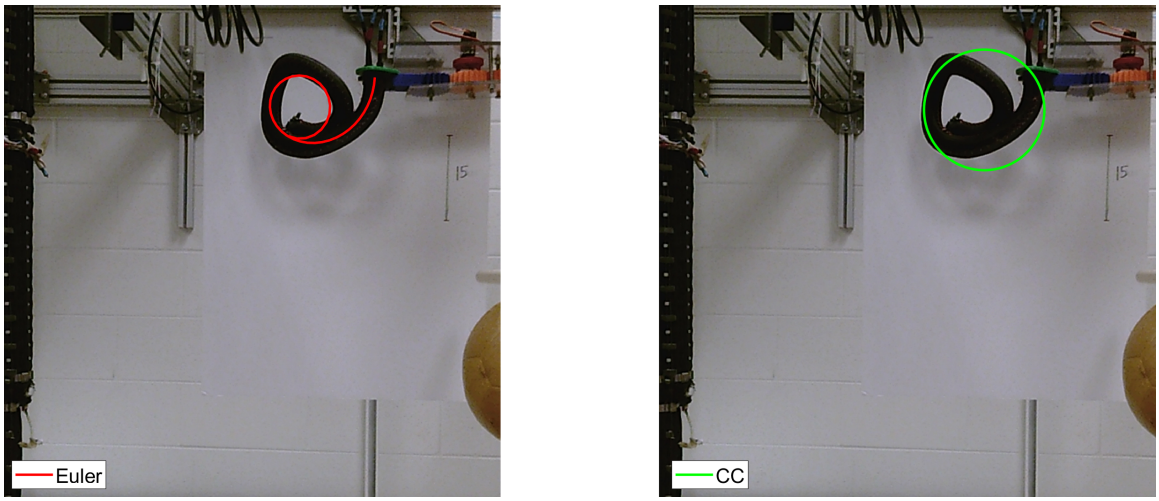

Figure 3.37: Modified Euler modeling. Pressure values (in PSI) in Mawby section muscles 1,2 and 3: 26-0-0

Pressure (PSI)	CC error e1 (in m)	Modified-Euler error e2 (in m)	Percent error decrease
13	0.0892	0.0056	93.72
16.25	0.05	0.0128	74.4
19.5	0.0443	0.0146	67.04
22.75	0.0388	0.0109	71.91
26	0.0389	0.0131	66.32

Table 3.8: Error Comparison for Mawby - Modified Euler spirals

While it is clear that the Modified approach to generating Euler curves in this section represents a significant improvement on the constant curvature model, it was lagging in accuracy when compared to the Plant curl model (Section 3.3) and the Euler model (Section3.2). Also, varying r adds more unknown variables to the Euler spiral generating equations which is not desired.

The comparison of all three methods discussed in this chapter is shown in Table 3.9.

Pressure (PSI)	CC (in m)	Euler (percent decrease)	Plant Curl (percent decrease)	Modified-Euler (percent decrease)
13	0.0892	93.16	93.5	93.72
16.25	0.05	88.2	88.8	74.4
19.5	0.0443	72.01	64.79	67.04
22.75	0.0388	67.53	62.89	71.91
26	0.0389	71.98	84.06	66.32

Table 3.9: Error Comparison - all methods

The Euler curves (and the two alternative models described in this chapter) are a significant improvement over the constant curvature assumption. Although the Euler Spiral, Plant curl and Modified Euler equations show similar results, since the Euler Spiral equations use a constant r, this approach was selected to be tested on different curves generated by Mawby under various pressure values. The Euler equations were also tested on the Separating Section robot curves, and the results are discussed in the next section.

3.4.1 Separating Section - Single muscle actuation

With the significant improvement recorded by the implementation of the Euler model for Mawby section as seen earlier in Section 3.2, the effect of this model was further investigated on the shorter sections of the Separating Sections robot discussed in Chapter 2. Separating Sections' section curves were generated by actuating a single muscle with the other two muscles unpressurized. The input parameters are as shown in Table 3.10 and their corresponding comparisons can be seen in Figures 3.43-3.38.

Pressure (PSI)	r	s_1	s_2
13	0.084	0.016	0.51
16.25	0.075	0.16	0.525
19.5	0.066	0.155	0.53
26	0.059	0.155	0.535
29.25	0.047	0.145	0.52
32.5	0.042	0.14	0.52

Table 3.10: Input values for Separating Sections - single muscle actuation

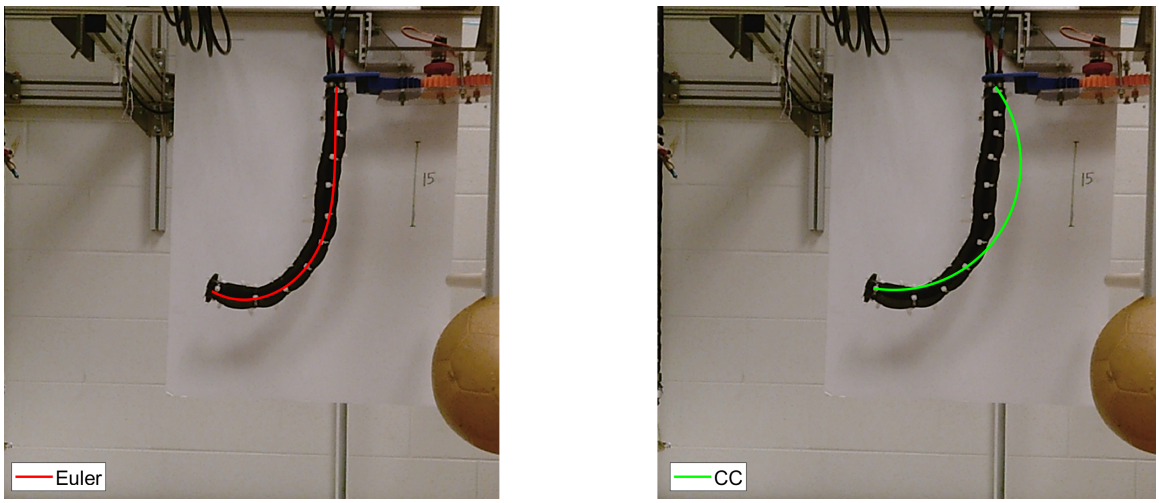

Figure 3.38: Pressure values (in PSI) in Separating Sections muscles 1,2 and 3: 13-0-0

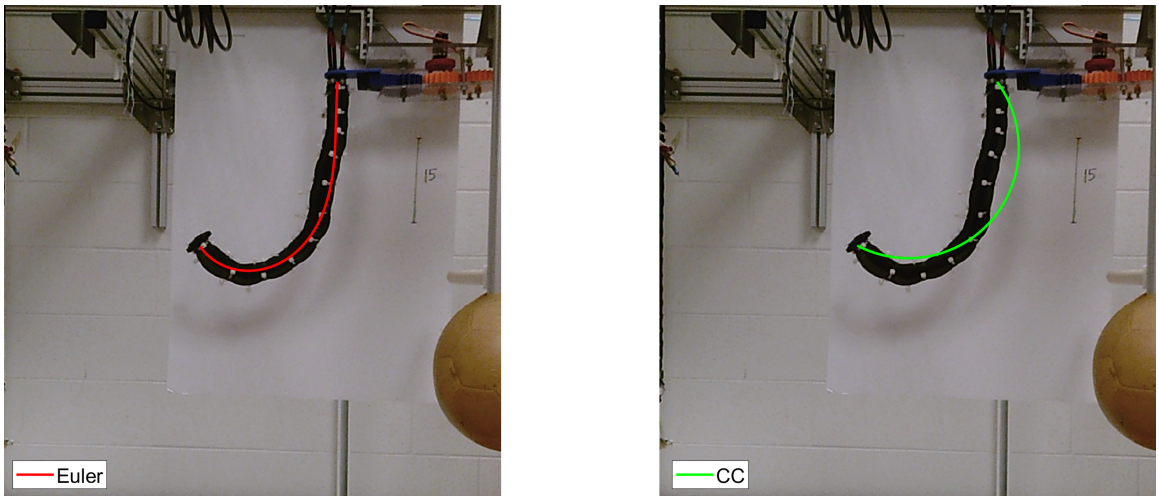

Figure 3.39: Pressure values (in PSI) in Separating Sections muscles 1,2 and 3: 16.25-0-0

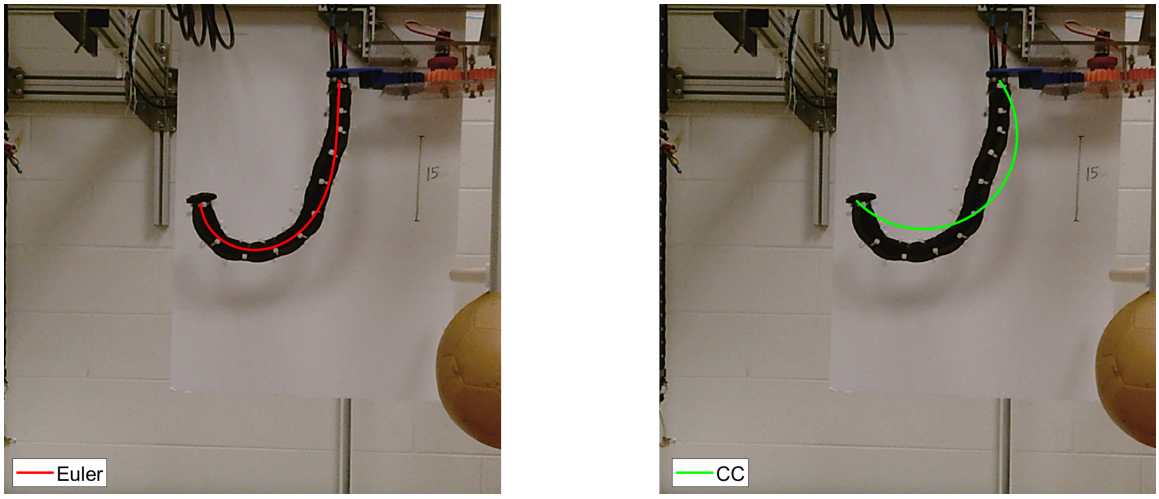

Figure 3.40: Pressure values (in PSI) in Separating Sections muscles 1,2 and 3: 19.5-0-0

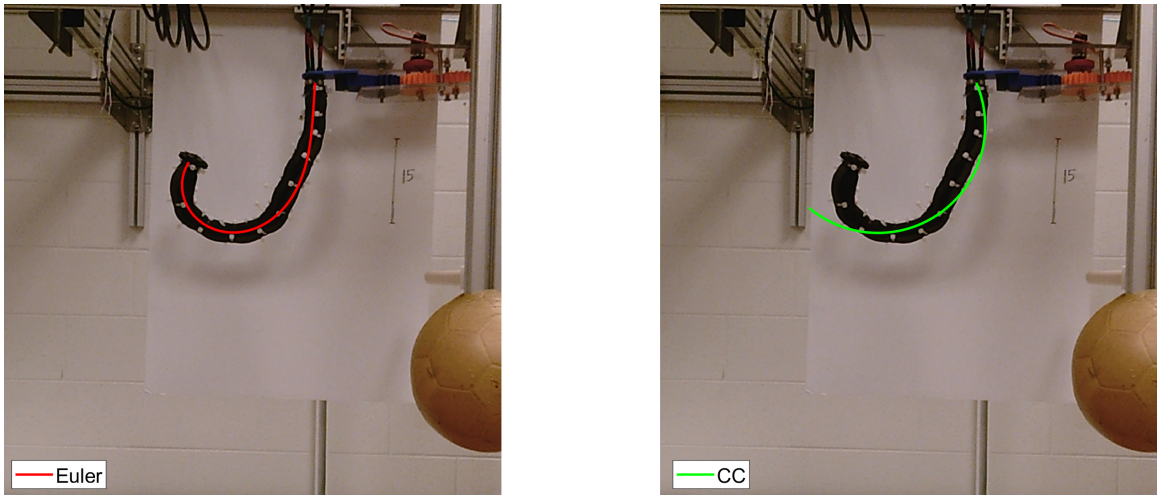

Figure 3.41: Pressure values (in PSI) in Separating Sections muscles 1,2 and 3: 26-0-0

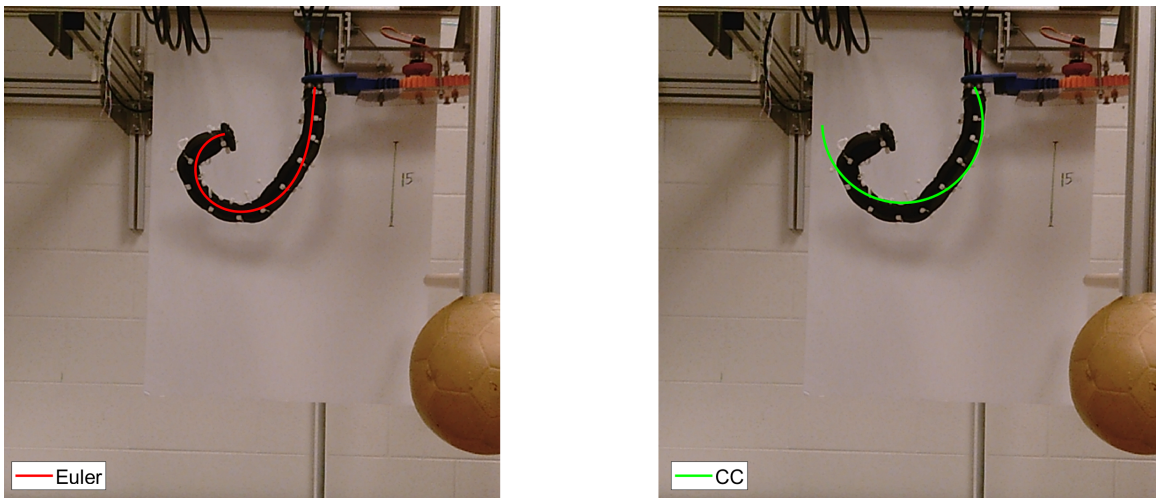

Figure 3.42: Pressure values (in PSI) in Separating Sections muscles 1,2 and 3: 29.25-0-0

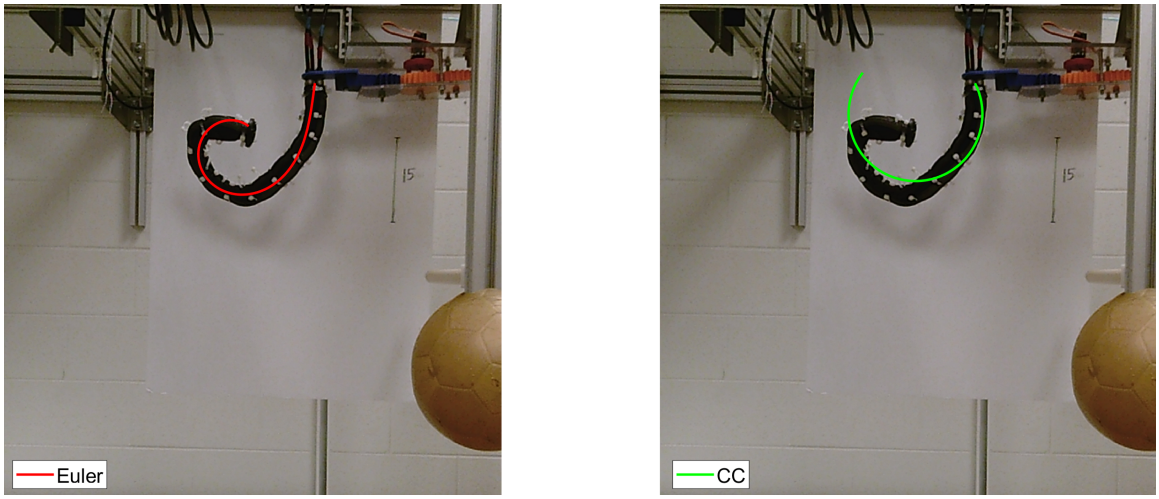

Figure 3.43: Pressure values (in PSI) in Separating Sections muscles 1,2 and 3: 32.5-0-0

Pressure (PSI)	CC error e1 (in m)	Euler error e2 (in m)	Percent error decrease
13	0.0311	0.0043	86.17
16.25	0.0278	0.0057	79.5
19.5	0.0311	0.0069	72.01
26	0.0301	0.0065	78.41
29.25	0.0307	0.0075	71.98
32.5	0.0291	0.0063	78.35

Table 3.11: Error Comparison for Separating Sections - single muscle actuation

3.4.2 2 muscles with fixed pressure of 9.75 PSI

The effect of this model was further investigated on the Mawby sections curves generated by varying the pressure in a muscle with the other two muscles actuated by a constant pressure each of 9.75 PSI. The input parameters are as shown in Table 3.12 and their corresponding comparisons can be seen in Figures 3.44-3.50.

Pressure (PSI)	r	s_1	s_2
13	0.115	0.14	0.535
16.25	0.086	0.115	0.525
19.5	0.069	0.1	0.52
22.75	0.057	0.09	0.518
26	0.043	0.085	0.518
29.25	0.033	0.1	0.518
32.5	0.03	0.1	0.518

Table 3.12: Input values for Mawby - 2 muscles with fixed pressure of 9.75 PSI

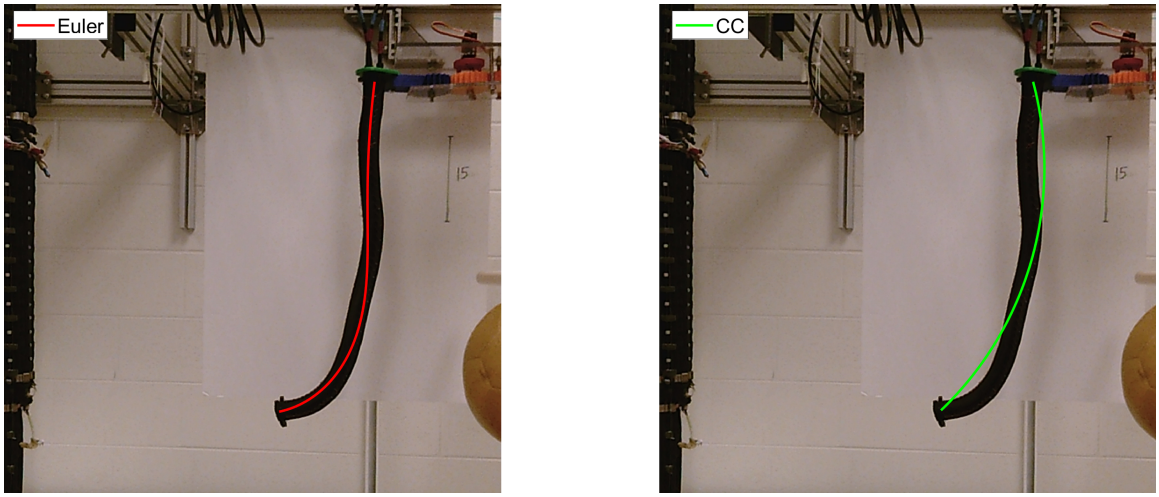

Figure 3.44: Pressure values (in PSI) in Mawby section muscles 1,2 and 3: 13-9.75-9.75

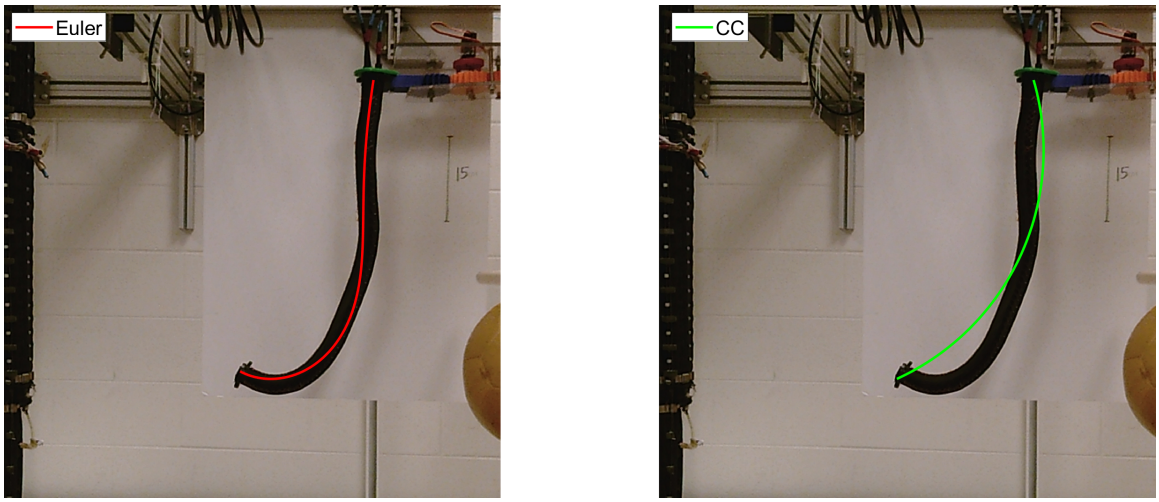

Figure 3.45: Pressure values (in PSI) in Mawby section muscles 1,2 and 3: 16.25-9.75-9.75

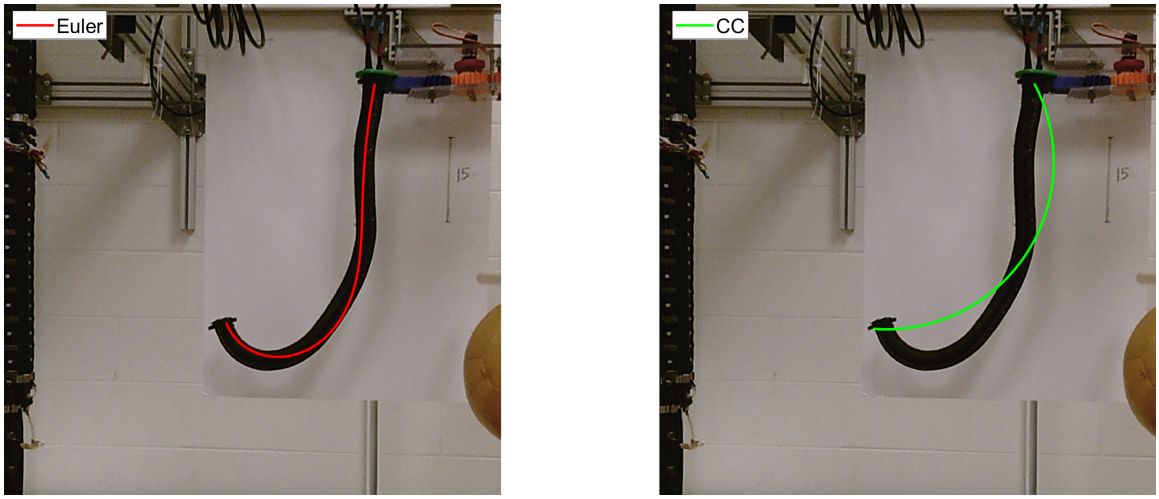

Figure 3.46: Pressure values (in PSI) in Mawby section muscles 1,2 and 3: 19.5-9.75-9.75

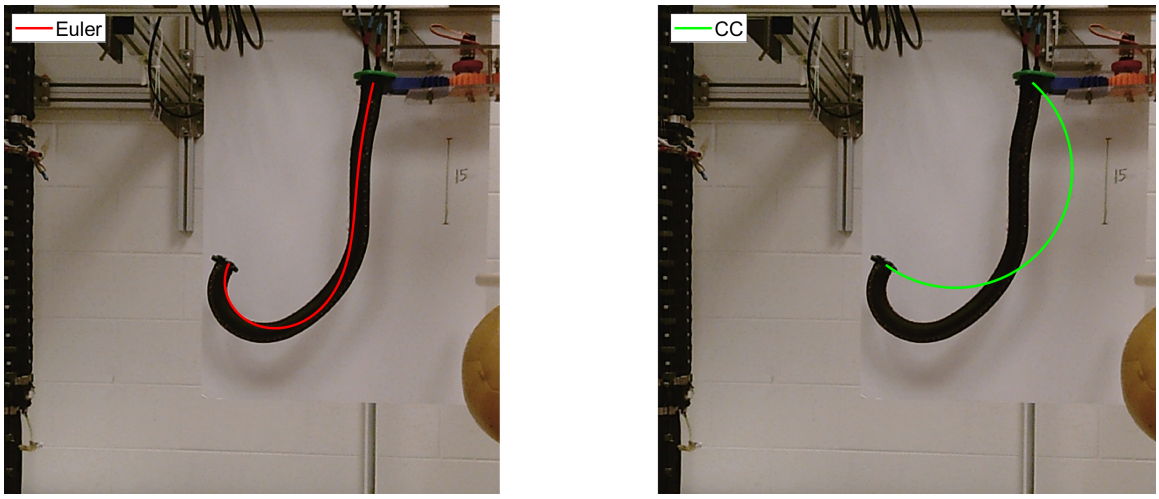

Figure 3.47: Pressure values (in PSI) in Mawby section muscles 1,2 and 3: 22.75-9.75-9.75

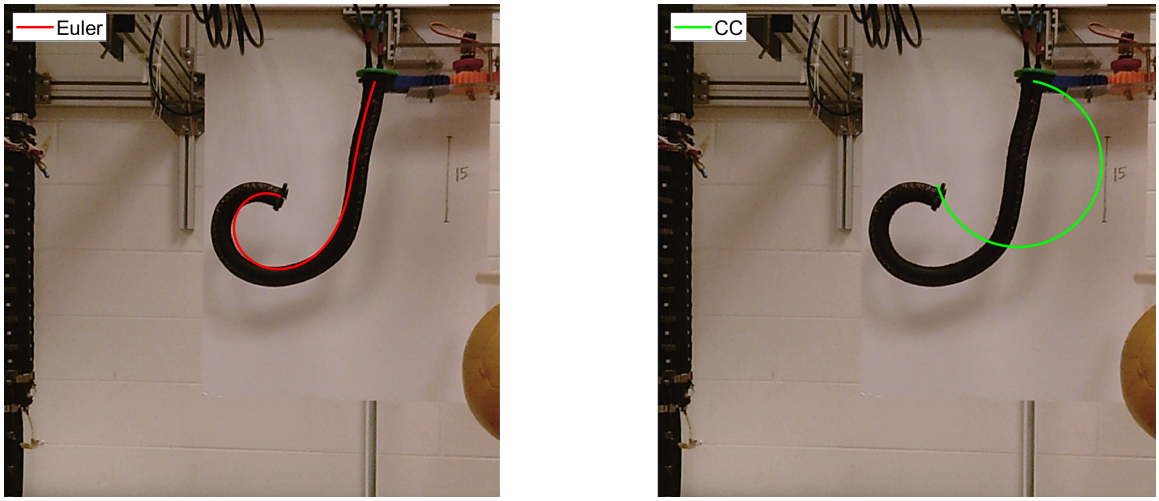

Figure 3.48: Pressure values (in PSI) in Mawby section muscles 1,2 and 3: 26-9.75-9.75

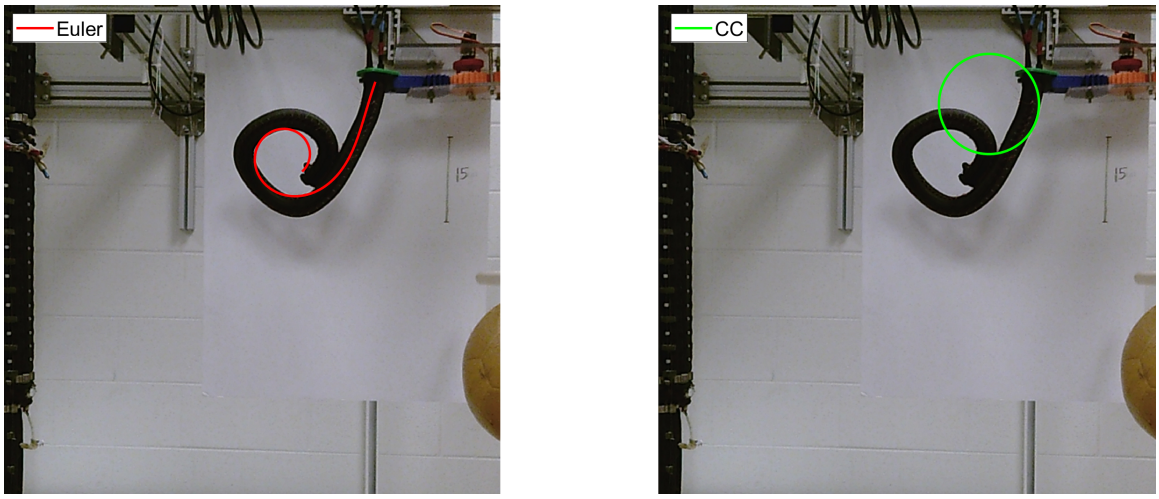

Figure 3.49: Pressure values (in PSI) in Mawby section muscles 1,2 and 3: 29.25-9.75-9.75

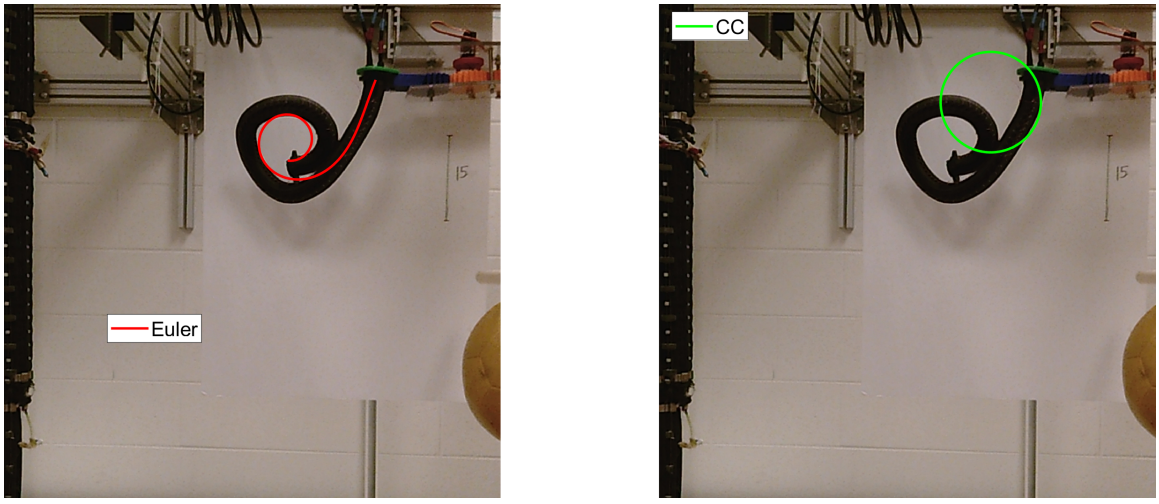

Figure 3.50: Pressure values (in PSI) in Mawby section muscles 1,2 and 3: 32.5-9.75-9.75

3.4.3 2 muscles with fixed pressure of 13 PSI

The effect of this model was further investigated on the Mawby sections curves generated by varying the pressure in a muscle with the other two muscles actuated by a constant pressure each of 13 PSI. The input parameters are as shown in Table 3.13 and their corresponding comparisons can be seen in Figures 3.51-3.56.

Pressure (PSI)	r	s_1	s_2
16.25	0.105	0.11	0.508
19.5	0.09	0.1	0.508
22.75	0.075	0.087	0.508
26	0.069	0.08	0.52
29.25	0.066	0.08	0.535
32.5	0.063	0.079	0.545

Table 3.13: Input values for Mawby - 2 muscles with fixed pressure of 13 PSI

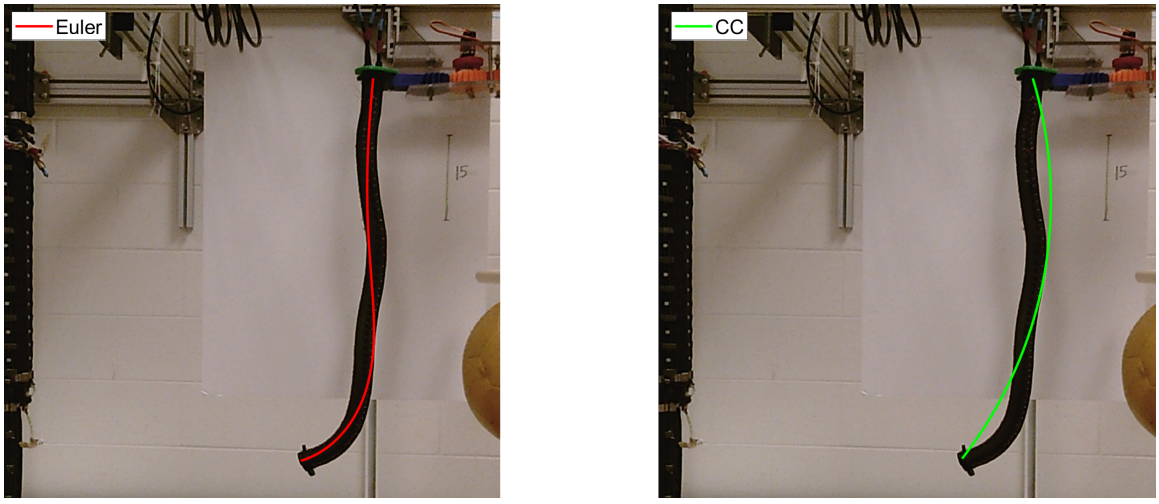

Figure 3.51: Pressure values (in PSI) in Mawby section muscles 1,2 and 3: 16.25-13-13

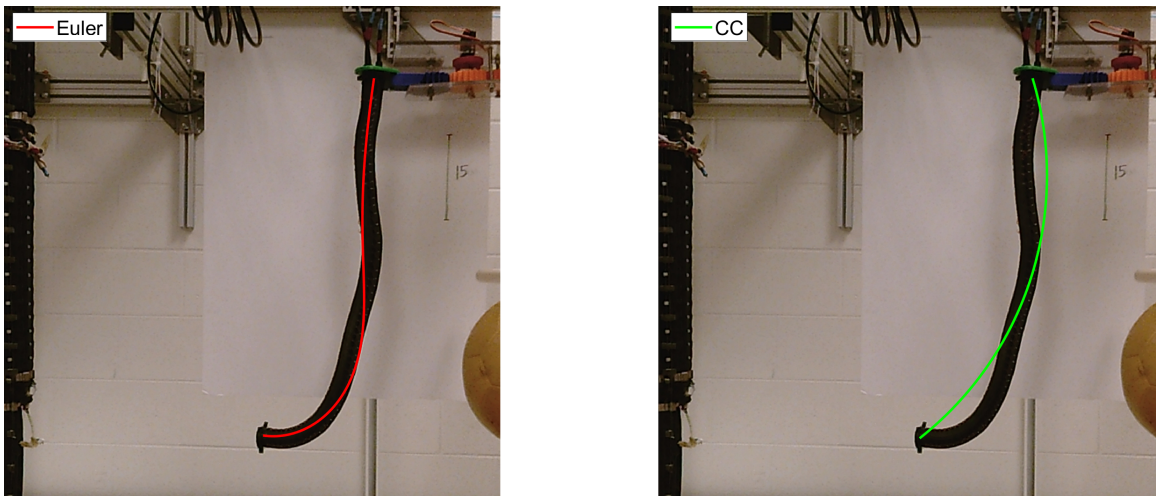

Figure 3.52: Pressure values (in PSI) in Mawby section muscles 1,2 and 3: 19.5-13-13

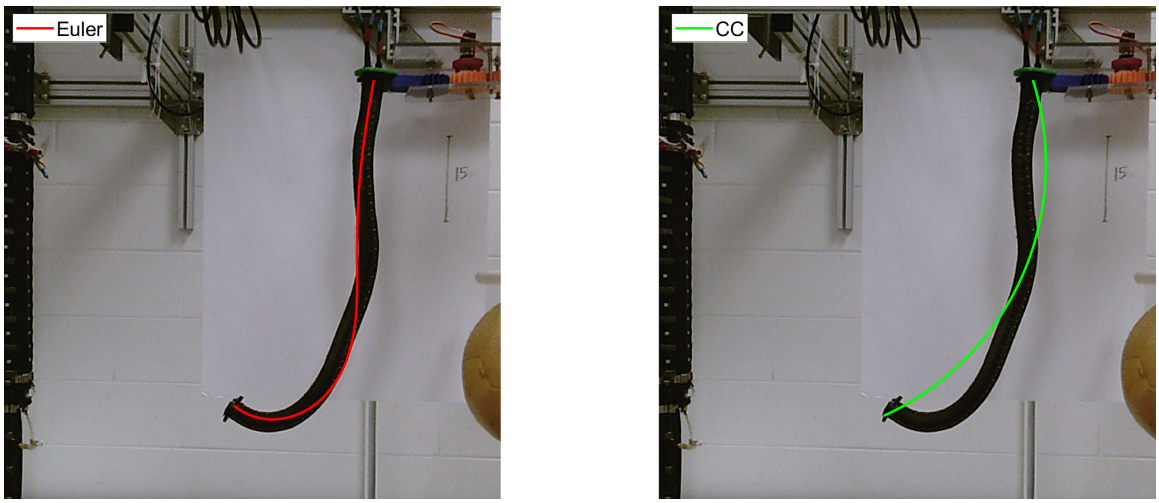

Figure 3.53: Pressure values (in PSI) in Mawby section muscles 1,2 and 3: 22.75-13-13

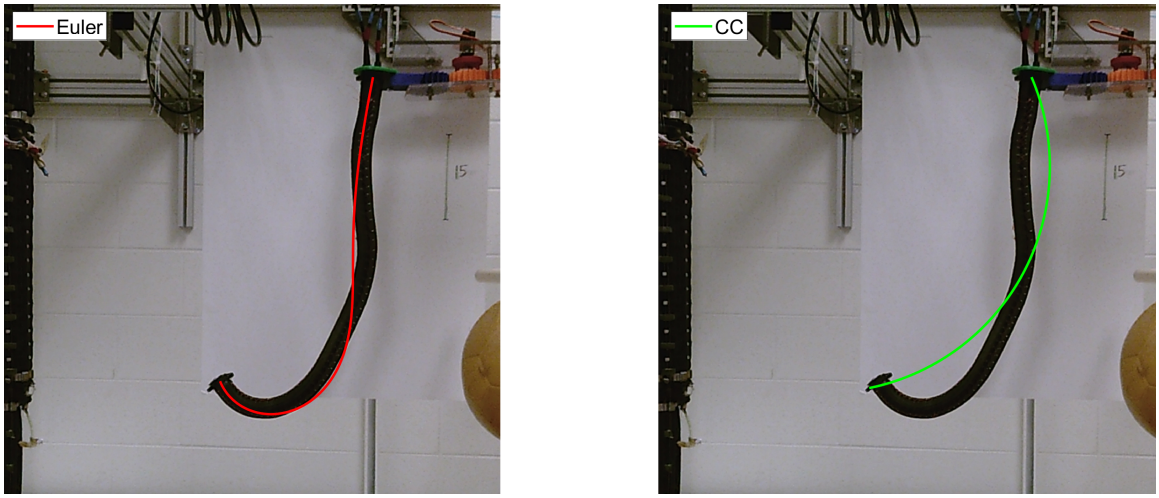

Figure 3.54: Pressure values (in PSI) in Mawby section muscles 1,2 and 3: 26-13-13

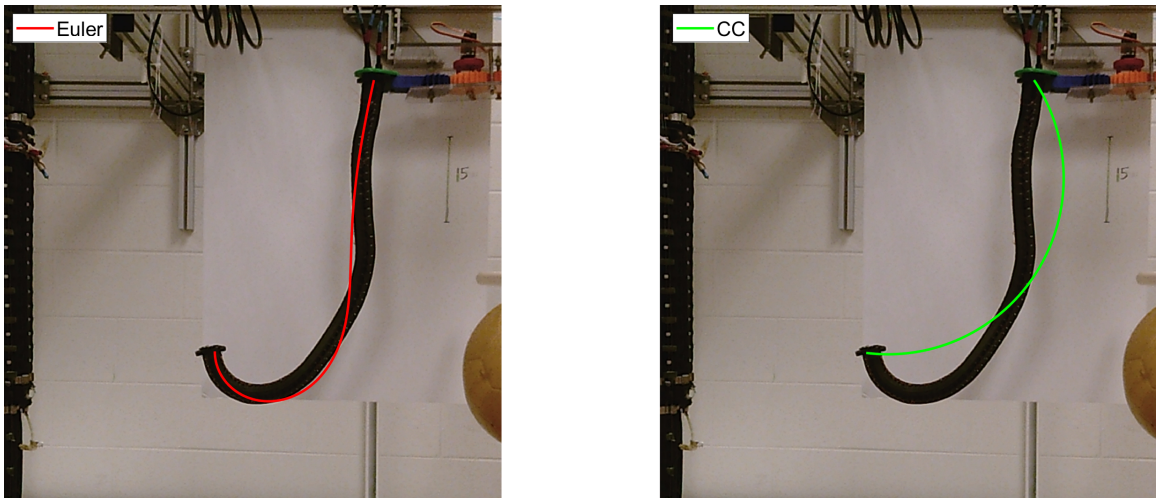

Figure 3.55: Pressure values (in PSI) in Mawby section muscles 1,2 and 3: 29.25-13-13

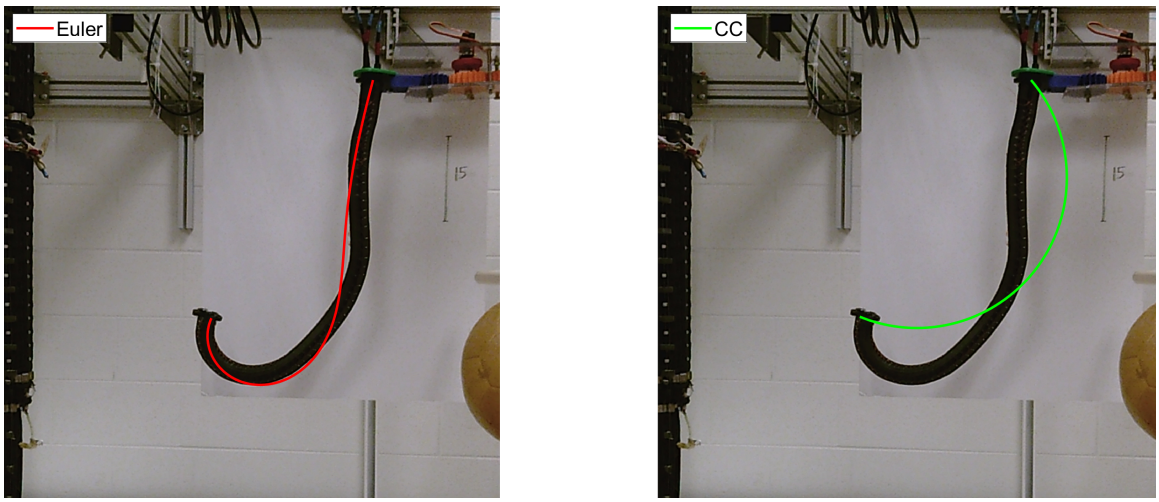

Figure 3.56: Pressure values (in PSI) in Mawby section muscles 1,2 and 3: 32.5-13-13

3.4.4 2 muscles with fixed pressure of 16.25 PSI

The effect of this model was further investigated on the Mawby sections curves generated by varying the pressure in a muscle with the other two muscles actuated by a constant pressure each of 16.25 PSI. The input parameters are as shown in Table 3.14 and their corresponding comparisons can be seen in Figures 3.57-3.61.

Pressure (PSI)	r	s_1	s_2
19.5	0.094	0.09	0.475
22.75	0.08	0.08	0.475
26	0.078	0.081	0.497
29.25	0.076	0.081	0.515
32.5	0.082	0.09	0.55

Table 3.14: Input values for Mawby - 2 muscles with fixed pressure of 16.25 PSI

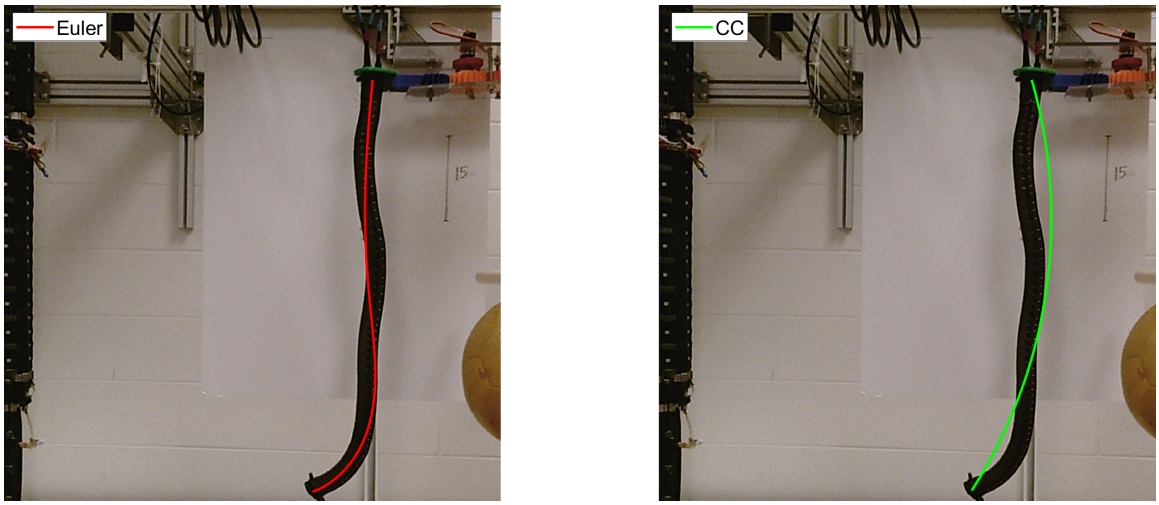

Figure 3.57: Pressure values (in PSI) in Mawby section muscles 1,2 and 3: 19.5-16.25-16.25

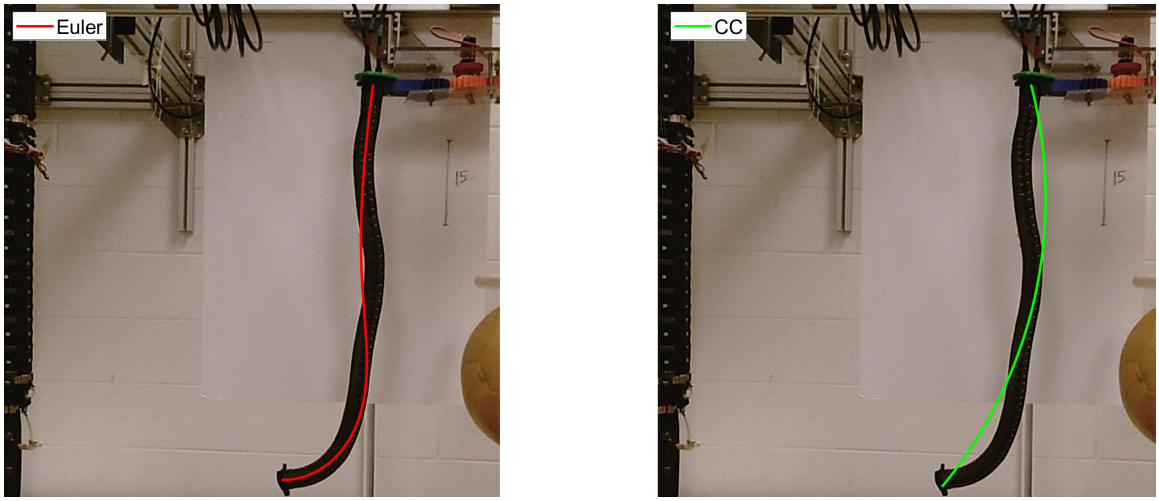

Figure 3.58: Pressure values (in PSI) in Mawby section muscles 1,2 and 3: 22.75-16.25-16.25

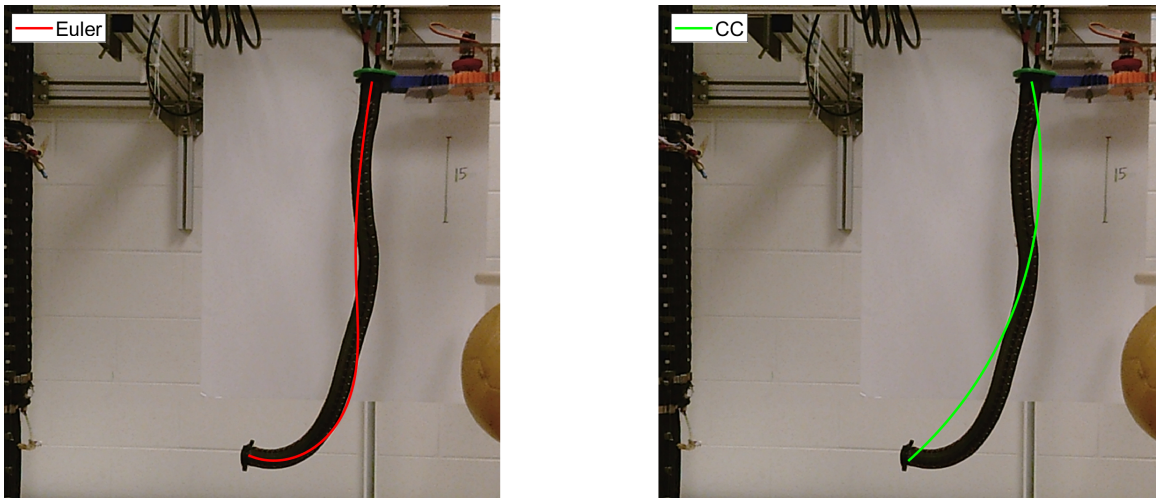

Figure 3.59: Pressure values (in PSI) in Mawby section muscles 1,2 and 3: 26-16.25-16.25

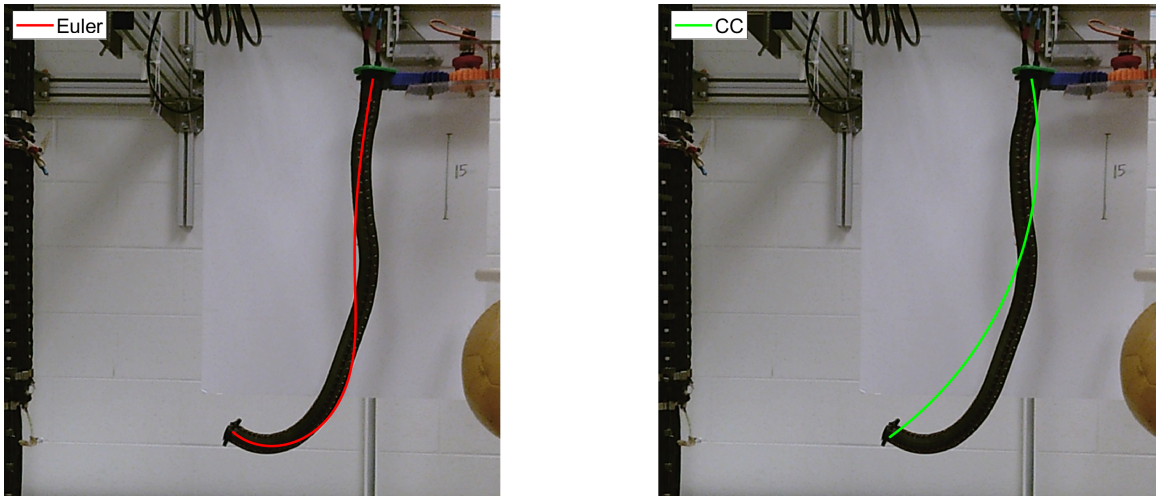

Figure 3.60: Pressure values (in PSI) in Mawby section muscles 1,2 and 3: 29.25-16.25-16.25

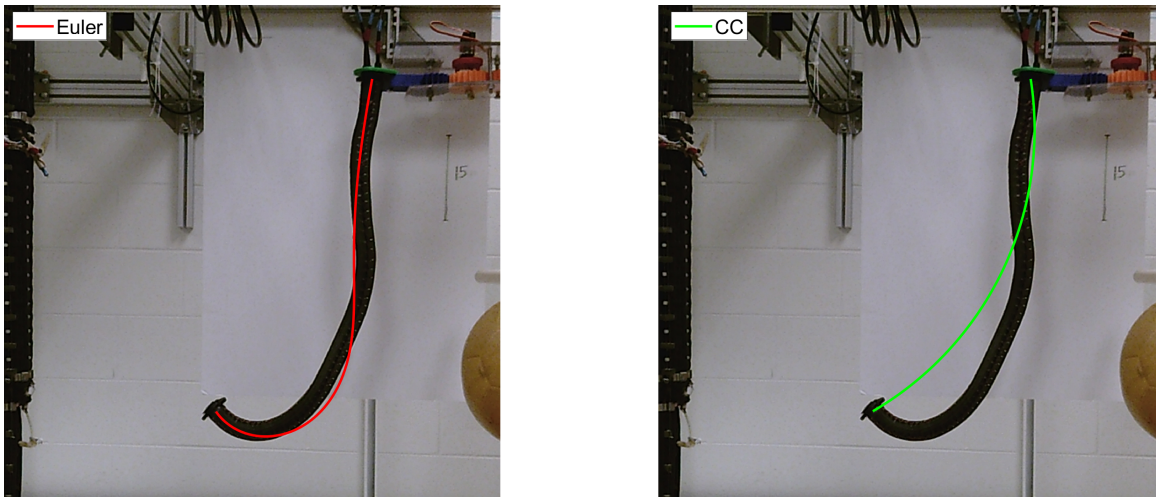

Figure 3.61: Pressure values (in PSI) in Mawby section muscles 1,2 and 3: 32.5-16.25-16.25

3.4.5 2 muscles with same pressure

The effect of this model was further investigated on the Mawby sections curves generated by actuating two muscles with same pressure while the third muscle was unpressurized. The input parameters are as shown in Table 3.15 and their corresponding comparisons can be seen in Figures 3.62-3.68.

Pressure (PSI)	r	s_1	s_2
13	0.09	0.125	0.56
16.25	0.075	0.11	0.57
19.5	0.061	0.1	0.57
22.75	0.042	0.1	0.57
26	0.038	0.1	0.57
29.25	0.036	0.1	0.57
32.5	0.034	0.1	0.58

Table 3.15: Input values for Mawby - 2 muscles with same pressure

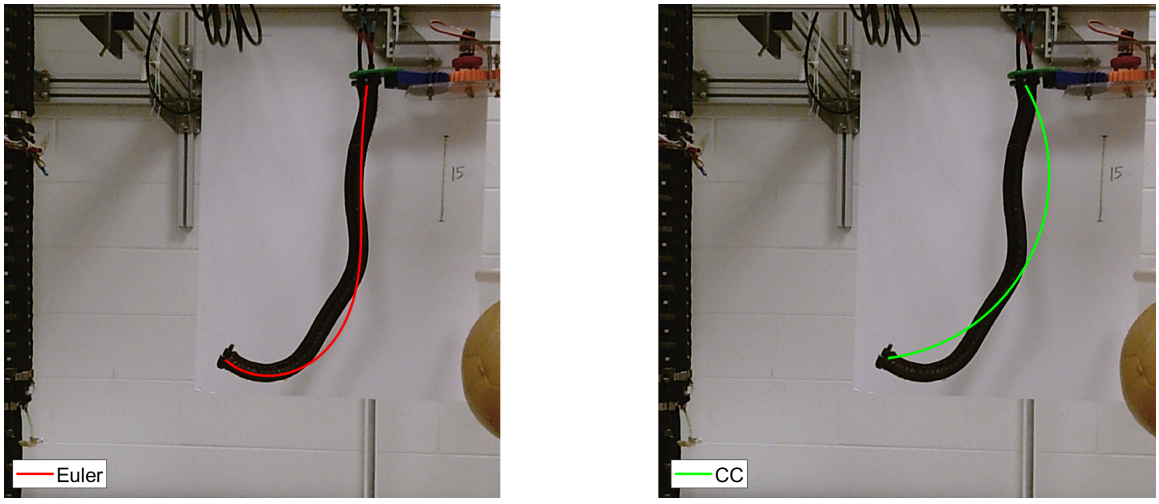

Figure 3.62: Pressure values (in PSI) in Mawby section muscles 1,2 and 3: 13-13-0

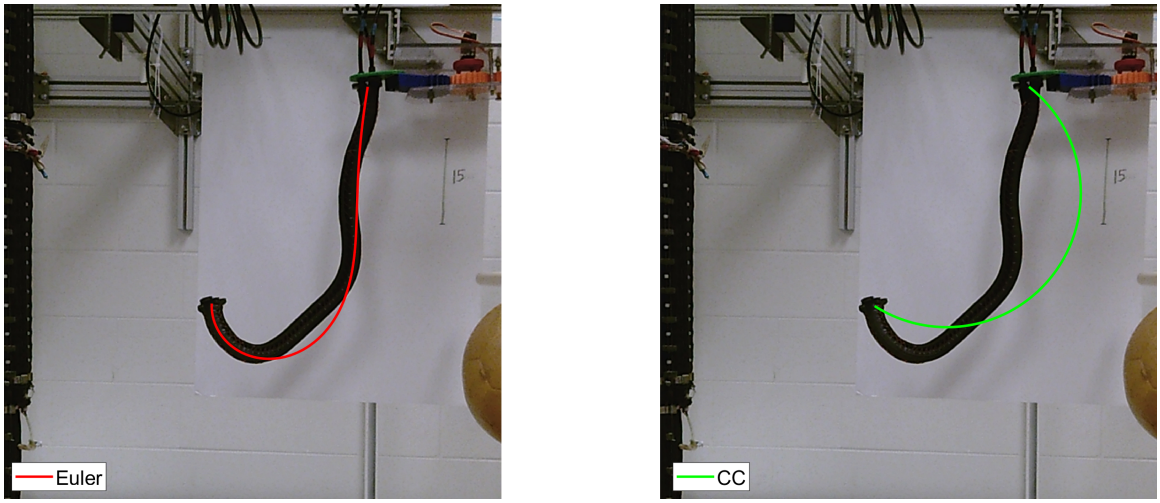

Figure 3.63: Pressure values (in PSI) in Mawby section muscles 1,2 and 3: 16.25-16.25-0

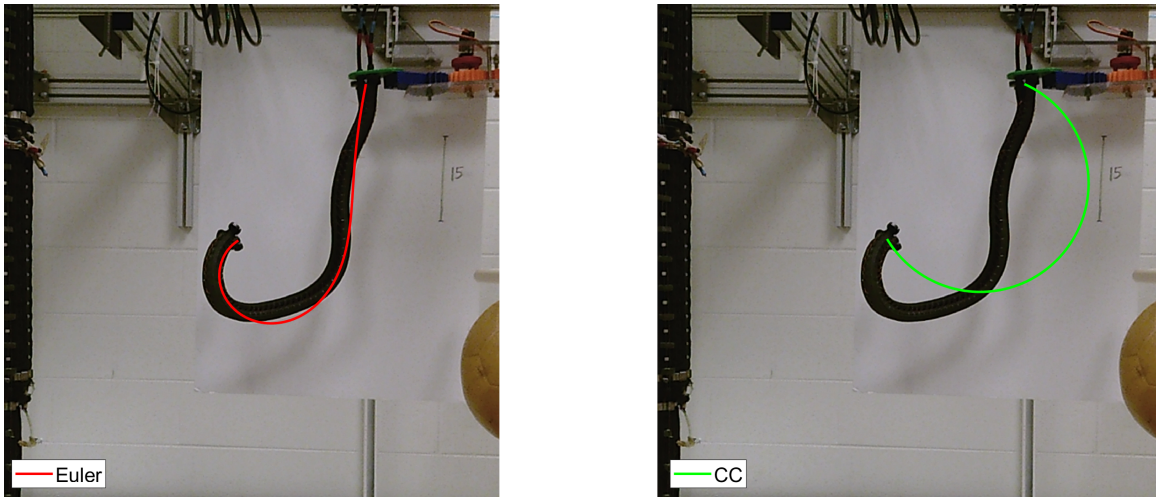

Figure 3.64: Pressure values (in PSI) in Mawby section muscles 1,2 and 3: 19.5-19.5-0

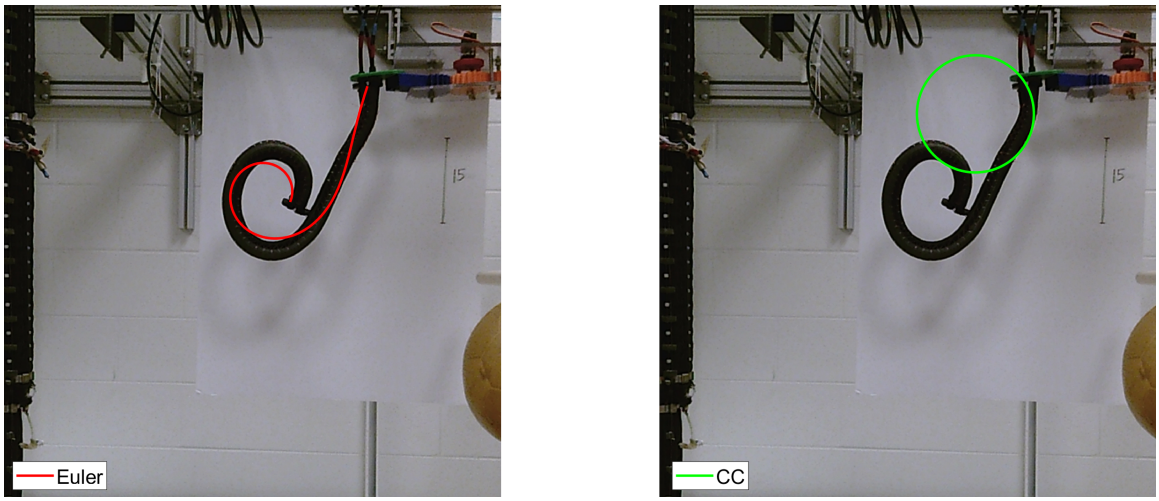

Figure 3.65: Pressure values (in PSI) in Mawby section muscles 1,2 and 3: 22.75-22.75-0

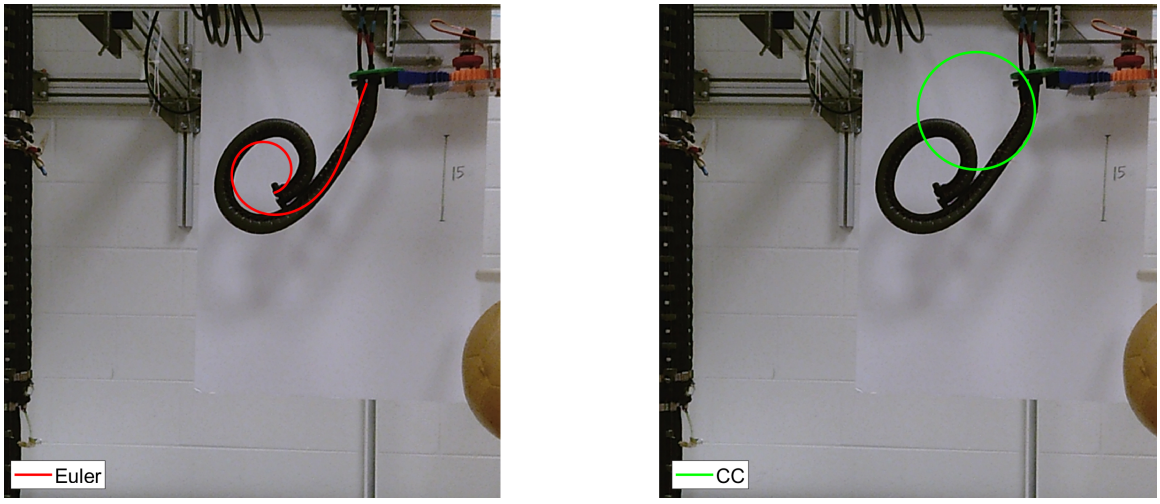

Figure 3.66: Pressure values (in PSI) in Mawby section muscles 1,2 and 3: 26-26-0

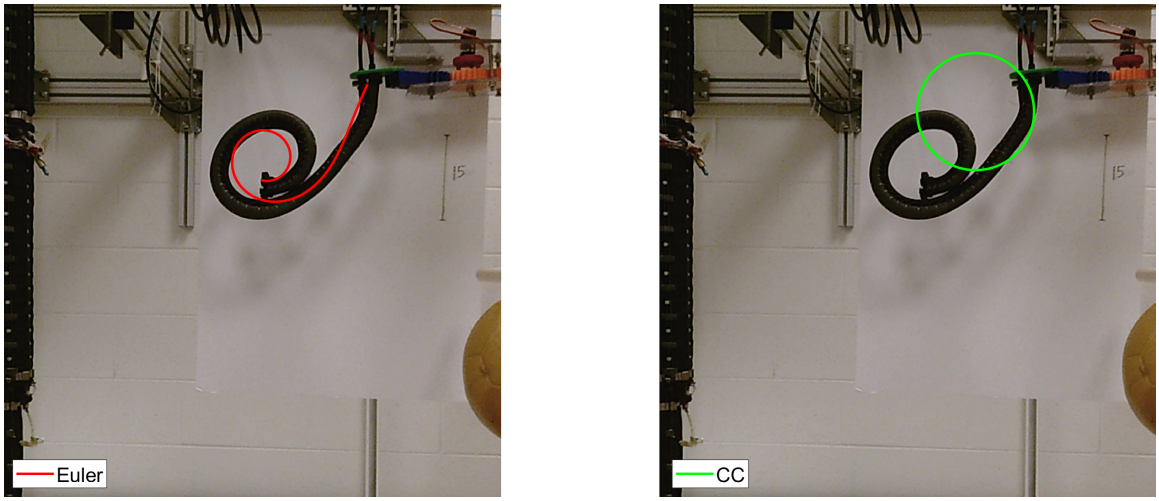

Figure 3.67: Pressure values (in PSI) in Mawby section muscles 1,2 and 3: 29.25-29.25-0

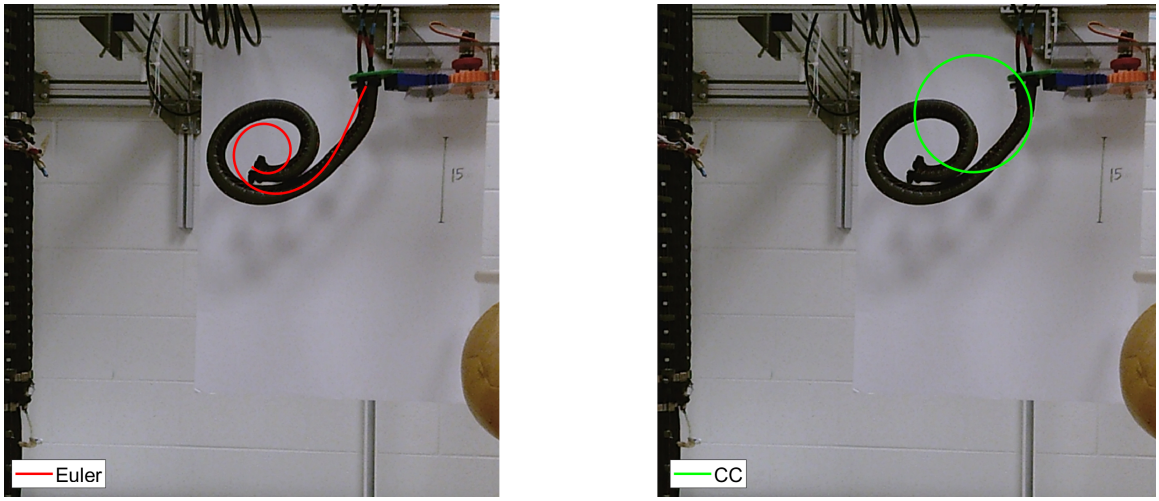

Figure 3.68: Pressure values (in PSI) in Mawby section muscles 1,2 and 3: 32.5-32.5-0

3.4.6 Separating Sections - 2 muscles with fixed pressure of 13 PSI

The effect of this model was further investigated on the Separating Sections section curves generated by varying the pressure in a muscle with the other two muscles actuated by a constant pressure each of 13 PSI. The input parameters are as shown in Table 3.16 and their corresponding comparisons can be seen in Figures 3.69-3.74.

Pressure (PSI)	r	s_1	s_2
16.25	0.105	0.14	0.48
19.5	0.1	0.14	0.49
22.75	0.096	0.14	0.5
26	0.092	0.14	0.515
29.25	0.089	0.14	0.52
32.5	0.087	0.14	0.525

Table 3.16: Input values for Separating Sections - 2 muscles with fixed pressure of 13 PSI

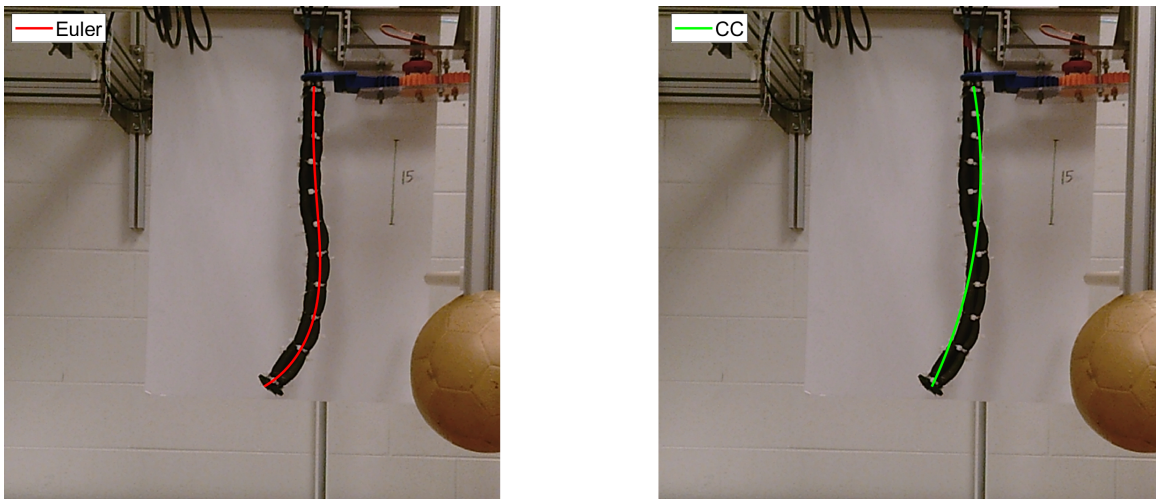

Figure 3.69: Pressure values (in PSI) in Separating Sections muscles 1,2 and 3: 16.25-13-13

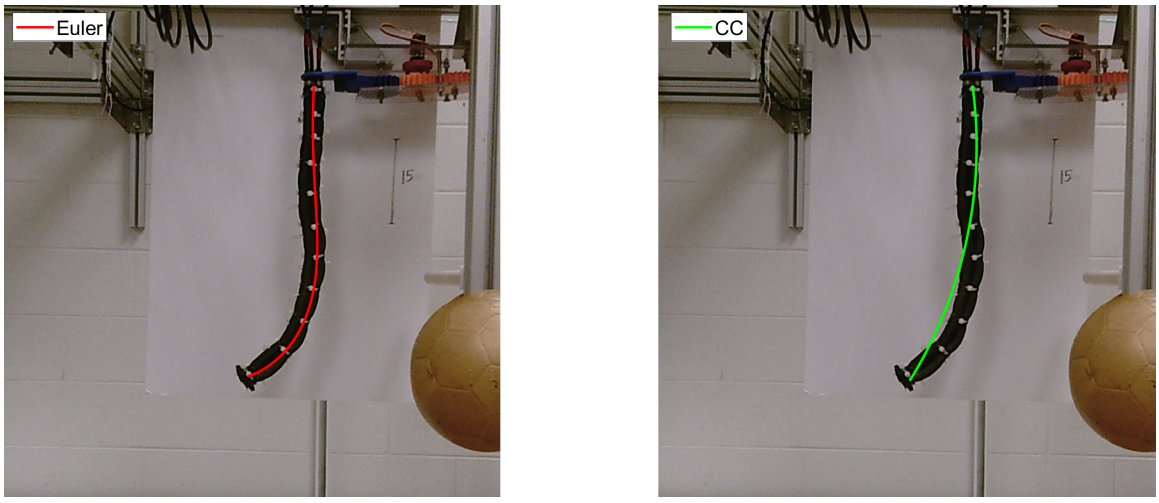

Figure 3.70: Pressure values (in PSI) in Separating Sections muscles 1,2 and 3: 19.5-13-13

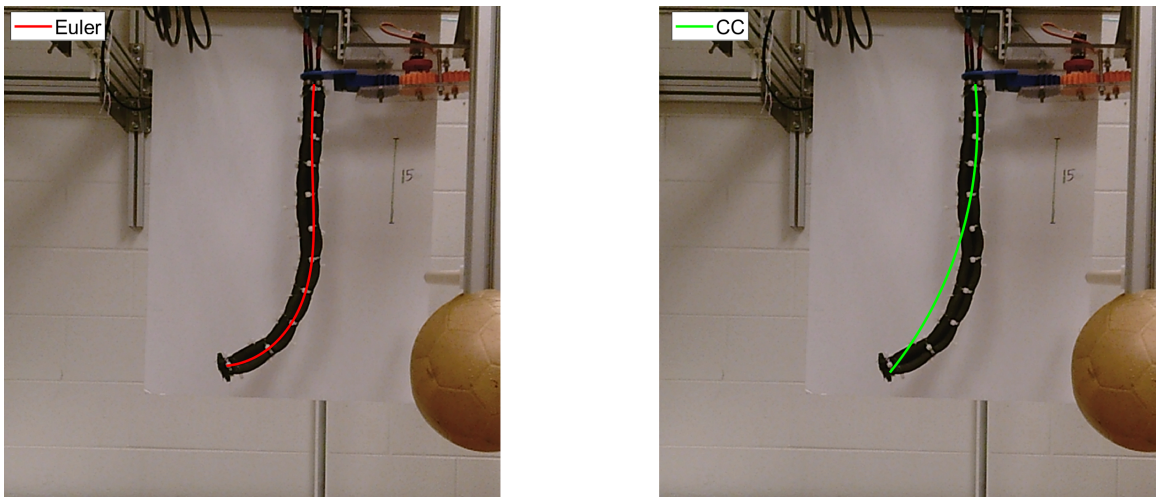

Figure 3.71: Pressure values (in PSI) in Separating Sections muscles 1,2 and 3: 22.75-13-13

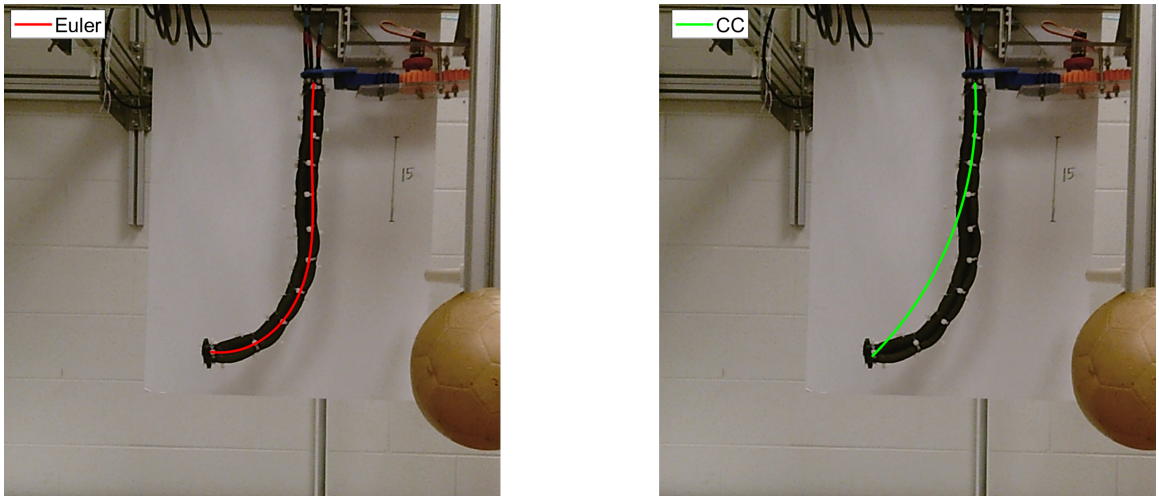

Figure 3.72: Pressure values (in PSI) in Separating Sections muscles 1,2 and 3: 26-13-13

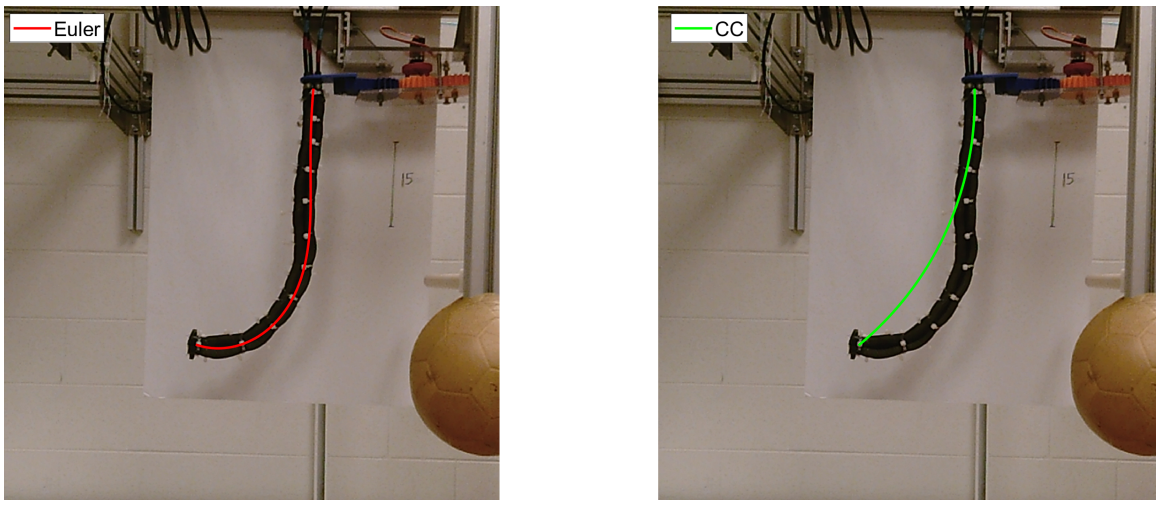

Figure 3.73: Pressure values (in PSI) in Separating Sections muscles 1,2 and 3: 29.25-13-13

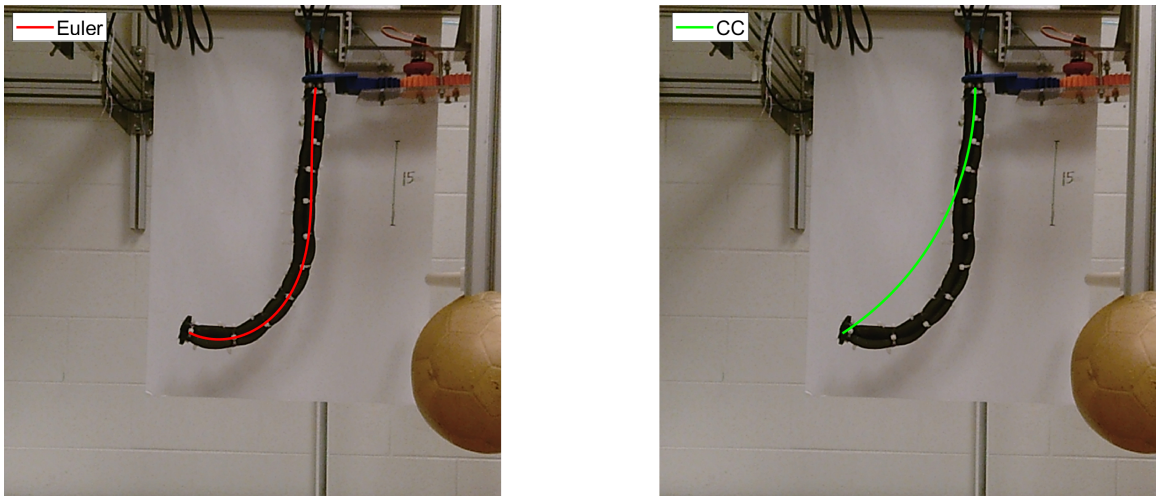

Figure 3.74: Pressure values (in PSI) in Separating Sections muscles 1,2 and 3: 32.5-13-13

3.4.7 Mawby - 2D experiments' results

The effect of this model was further investigated on the Mawby section curves generated for 2D experiments conducted by actuating a single muscle with the other two muscles unpressurized. The input parameters are as shown in Table 3.17 and their corresponding comparisons can be seen in Figures 3.75-3.80.

Pressure (PSI)	r	s_1	s_2
9.75	0.27	0.4	0.97
11.05	0.25	0.45	1.025
13	0.19	0.45	1.06
16.25	0.15	0.45	1.15
19.5	0.13	0.45	1.15

Table 3.17: Input values for Mawby - 2D

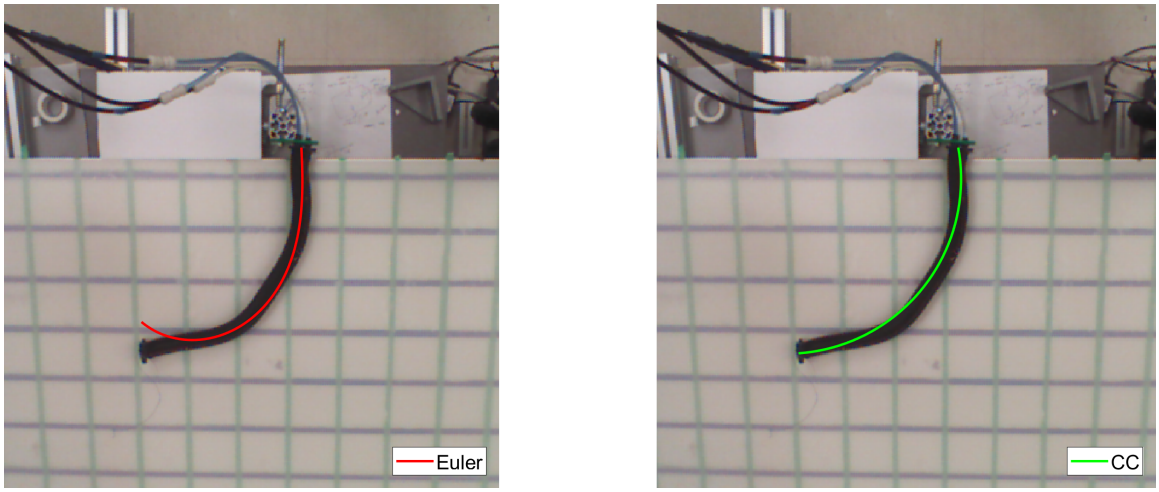

Figure 3.75: Pressure values (in PSI) in Mawby section muscles 1,2 and 3: 9.75-0-0

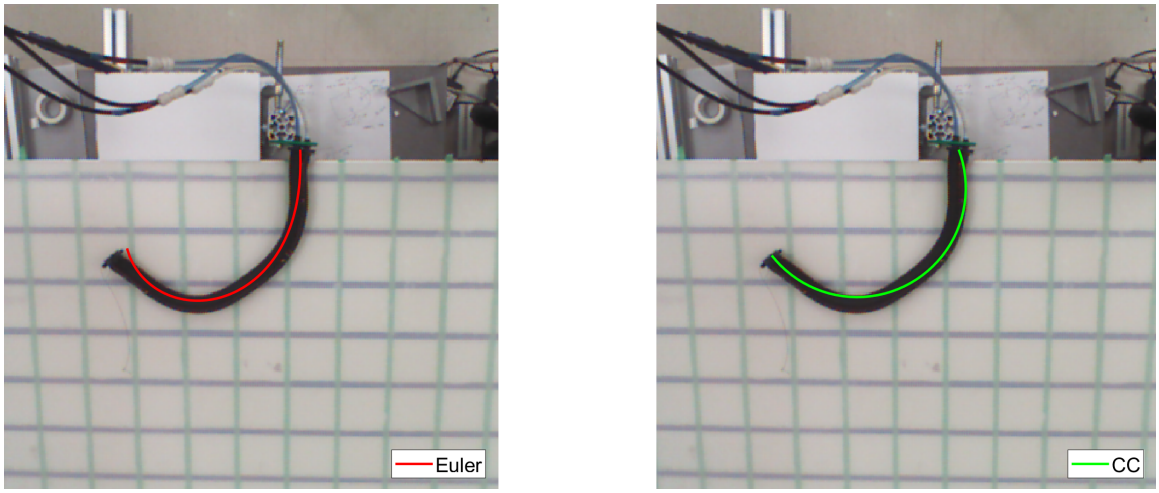

Figure 3.76: Pressure values (in PSI) in Mawby section muscles 1,2 and 3: 11.05-0-0

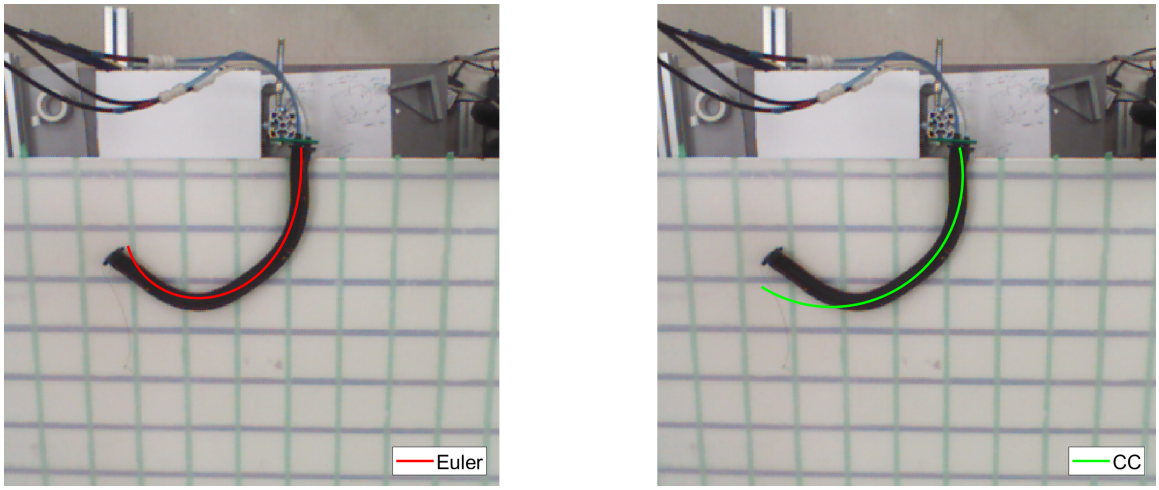

Figure 3.77: Pressure values (in PSI) in Mawby section muscles 1,2 and 3: 11.05-0-0 (2)

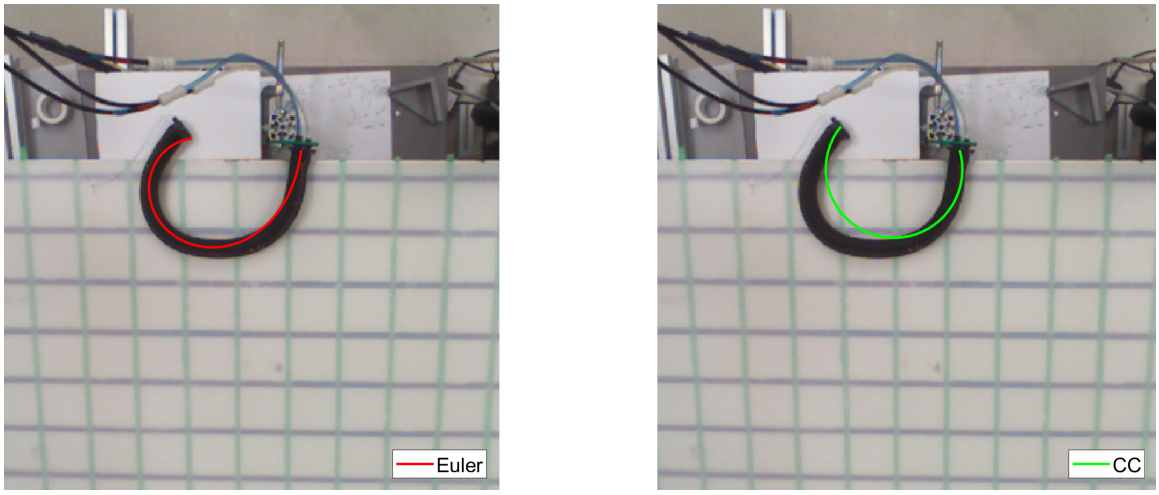

Figure 3.78: Pressure values (in PSI) in Mawby section muscles 1,2 and 3: 13-0-0

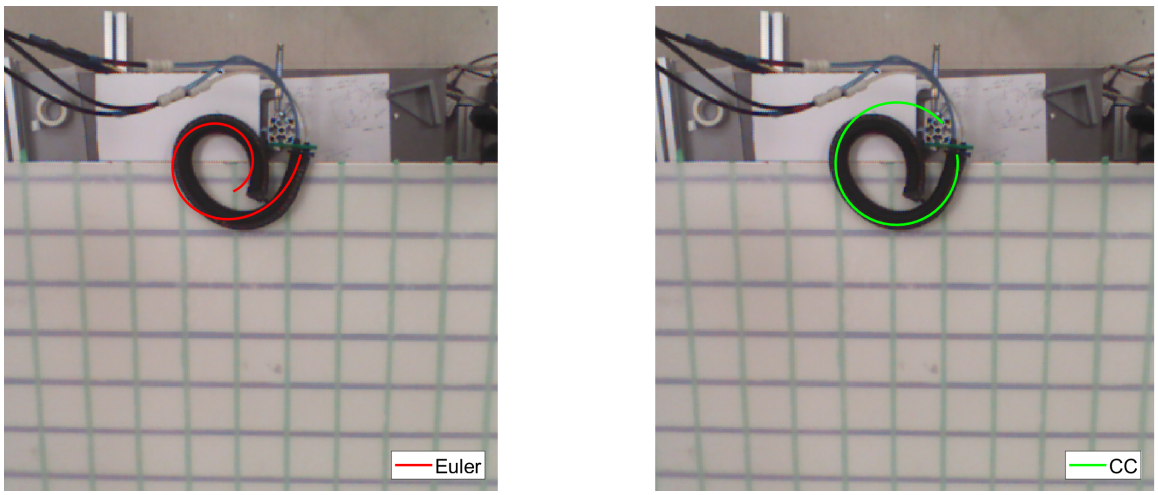

Figure 3.79: Pressure values (in PSI) in Mawby section muscles 1,2 and 3: 16.25-0-0

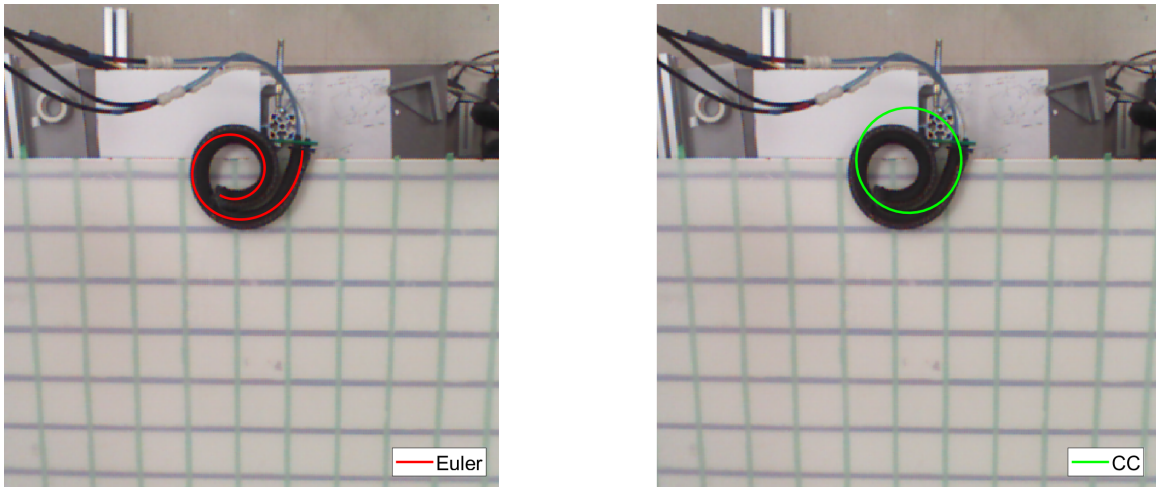

Figure 3.80: Pressure values (in PSI) in Mawby section muscles 1,2 and 3: 19.5-0-0

Pressure (PSI)	CC error - e1(in m)	Euler error (in m) (e2)	Percent error decrease
9.75	0.0081	0.0119	-46.91
11.05	0.0108	0.0081	25
11.05 (2)	0.0234	0.0081	65.38
13	0.025	0.0081	67.6
16.25	0.0369	0.0141	61.79
19.5	0.0326	0.0073	77.61

Table 3.18: Error Comparison - single muscle actuation for Mawby - 2D

Numerous cases of the Mawby section and Separating Sections section curves were illustrated and analyzed. The effect of the Euler curve approach was investigated on 42 different curves generated by varying the pressures in the muscles of the robots discussed in Chapter 2. It can be seen that the accuracy of the Euler curve approach is very good across a wide range of configurations.

Chapter 4

Statics

In this chapter, we investigate the underlying causes of the non-constant curvatures exhibited by the long, thin continuum sections of the Mawby and Separating Sections robots of Chapter 2, and kinematically modeled in Chapter 3. We use the statics of pneumatic muscles to develop a new understanding of the distribution of forces within such muscles. The design and implementation of a static model for a continuum robot is detailed in [40].

4.1 Underlying Theory

When pressure P is applied to a cylindrical tube, neglecting the effect of the change in volume, the force F it generates can simply be given by:

$$F = PA \tag{4.1}$$

where A is the the cross-sectional area. Because the extension occurs due to the force at the tip of the muscle, the area in question is the circular cross-section of the tube in which the force is acting. Upon exertion of the force, the muscle extension

is governed by the modulus of elasticity E of the material from which it is made. The modulus of elasticity is also known as Young's Modulus, and is determined by

$$E = \frac{FL_o}{A\Delta L} \tag{4.2}$$

where L_o is the initial length of the tube and ΔL is the increase in the length. It can be seen that the Young's modulus is inversely proportional to the displacement. Hence, the greater the modulus of elasticity, the lower the displacement of the muscle length for a given force. The resistance force exerted by the material can be determined by the equation shown below.

$$F_Y = \frac{EA\Delta L}{L_o} \tag{4.3}$$

Hence, when a single muscle is actuated, it extends, and since in the case of Mawby each muscle is connected to two other muscles along its length, the other muscles are physically constrained to extend. The force due to the Young's modulus in the actuated muscle causes the linear extension of that muscle, while the force due to the Young's modulus of the other two muscles causes the section to bend as this causes a Moment M. The curvature k caused due to M is given by the Euler-Bernoulli formula shown in Equation 4.4.

$$k = \frac{M}{EI} \tag{4.4}$$

where I is the second moment of inertia of the cylindrical tube at cross section of the tip where the force is acting, and is given by

$$I = \frac{\pi}{64}(d_o^4 - d_i^4) \tag{4.5}$$

To gain a better understanding of the theory explained in this section, a simple two-muscle system is considered and the cross section of the two connected muscles is as shown in Figure 4.1, such that when same pressure is applied to both muscles they extend axially out of plane. The muscles in the system are connected to each other at point O and each have a radius r. When only one muscle is pressurized, a force F due this pressure is generated at this cross section and is given by Equation 4.1. Due to this force there is extension in the muscle and due to the physical constraint at point O, the other muscle is caused to extend. Due to the elastic modulus E of the material of the muscle, the extension in the unpressurized muscle causes a force F_Y acting axially into the plane at the point of contact O and is given by Equation 4.3. The resultant force F_R of these two forces (F and F_Y) causes a moment M given by Equation 4.6 and the corresponding curvature k of the two muscles is given by Equation 4.4.

$$M = r \times F_R \tag{4.6}$$

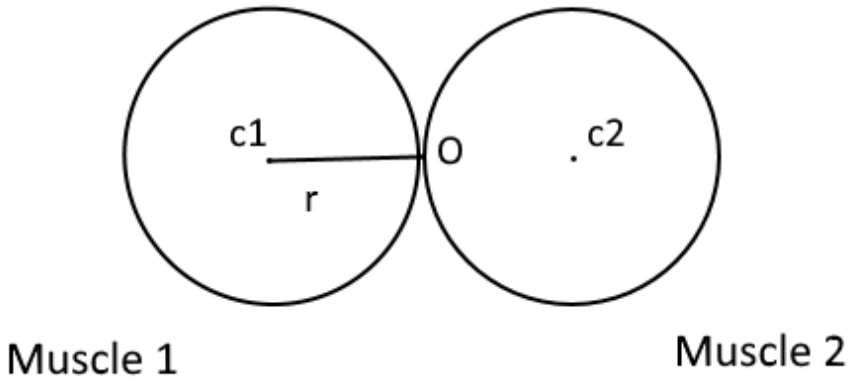

Figure 4.1: Two-muscle system representation

We next introduce a model for analyzing the geometric distribution of the forces produced by pneumatic continuum sections with three muscles. The orientation of the muscles can be represented as shown in Figure 4.2. The three muscles, labeled 1, 2 and 3, have equal radius $r \in \mathbb{R}$ and their centers are equidistant from the origin (O) and from each other. When muscle 1 is actuated, and the other two muscles are unpressurized, due to the resistive forces of the other two muscles, the resultant direction is in the $-Y$ direction as shown. This resultant force generated by the actuation of muscle 1 is termed $F_1 \in \mathbb{R}$. Muscles 2 and 3 are oriented at a 60° angles from the Y-axis, and their resultant forces $F_2 \in \mathbb{R}$ and $F_3 \in \mathbb{R}$ respectively are at 30° angles from the X-axis as shown. When multiple sections are actuated, the resultant force F_r and the direction of this force ϕ can be calculated by finding their component forces in the X and Y axis. This produces the equations below:

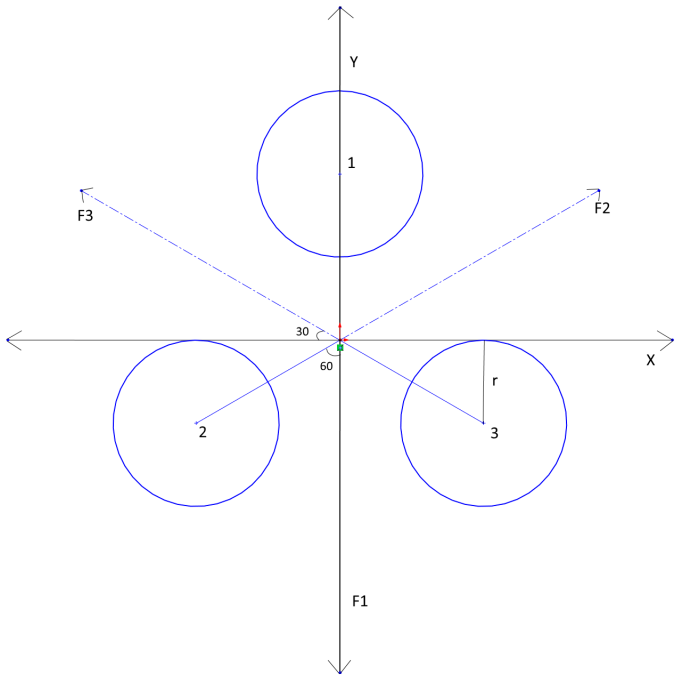

Figure 4.2: Muscle orientations and their forces

$$F_x = F_2 \cos 30^\circ - F_3 \cos 30^\circ \tag{4.7}$$

$$F_y = F_1 \cos 60^\circ - F_3 \cos 60^\circ - F_1 \tag{4.8}$$

$$F_r = \sqrt{F_x^2 + F_y^2} \tag{4.9}$$

$$\phi = \arctan \frac{F_y}{F_x} \tag{4.10}$$

To illustrate the above analysis, an experiment was conducted, moving a section 120° about its long axis (out of page in Figure 4.2), while maintaining a constant curvature. To achieve this, it was decided to test using a constant resultant force during the entire 120° motion. To perform this only two muscles were required. By setting $F_1 = 0$, all possible combinations for the pressures in the two other muscles within the operating range were calculated to achieve the desired resultant pressure value. Once all the combinations of values for the two muscles were generated, they were sorted by their ϕ values, so that the section moves from 0° to 120°. The plot of this sorted pressure profile is shown in Figure 4.3. The corresponding hardware motion can be seen in Figure 4.4 where the section rotates about its long axis with a constant curvature.

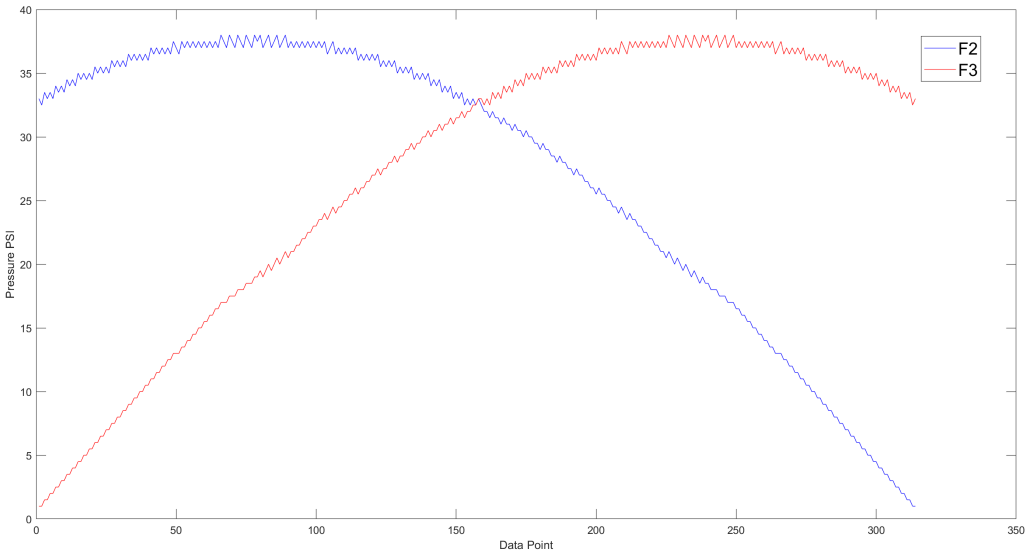

Figure 4.3: Resultant pressure in two muscle plot

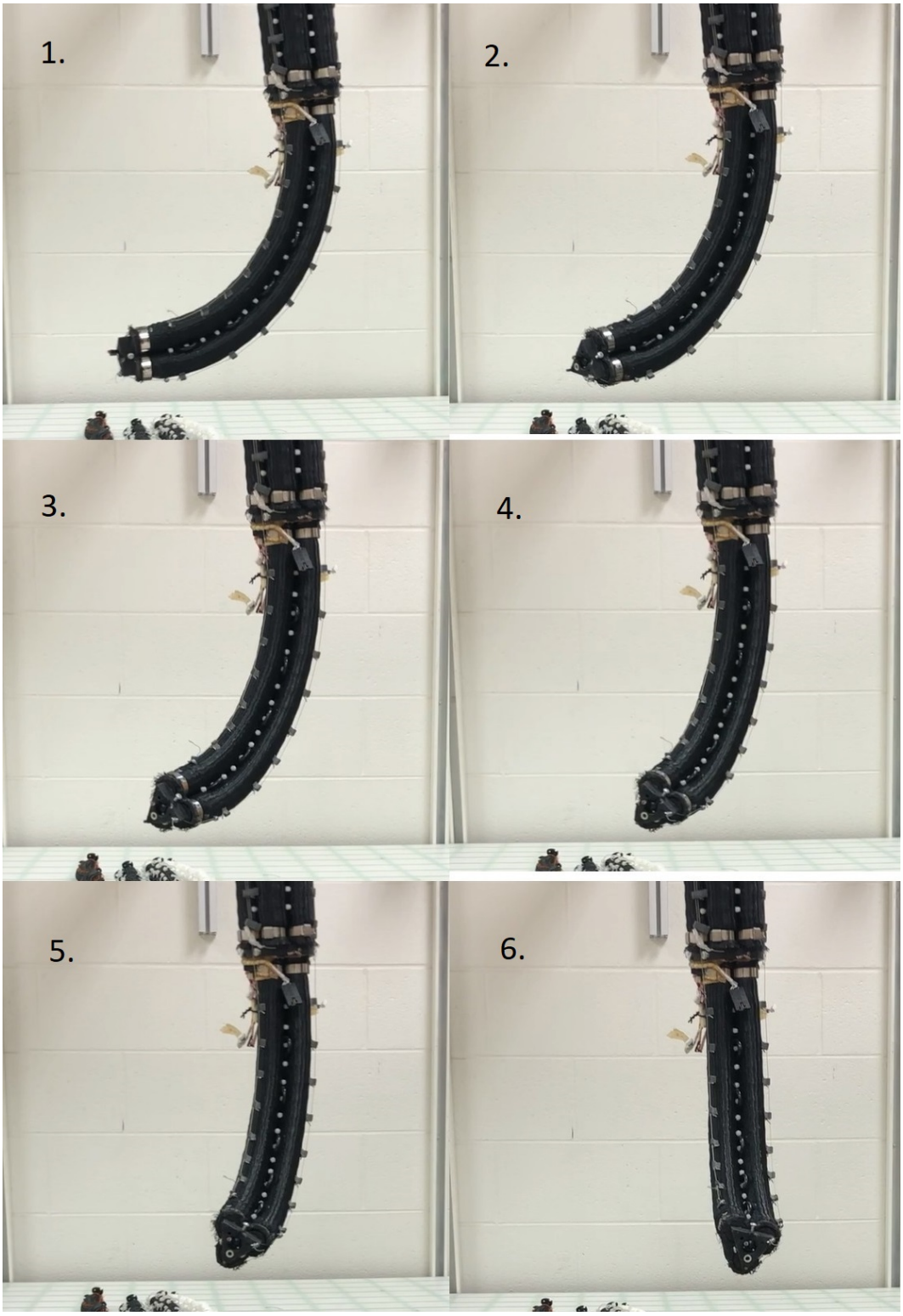

Figure 4.4: Octarm section transition from 0° to 120°

4.2 An Observation

When the data (s and r values) for various curvatures generated from varying input pressure values and the Euler spiral model-fitting performed in Chapter 3 were analyzed, it was observed that a value $m = w(sk)^2$, where $s \in \mathbb{R}$ is the arc length, $k = s/r$ is the curvature, and $w \in \mathbb{R}$ is a constant, followed a similar pattern with $P_r w \in \mathbb{R}$ - the resultant pressure calculated as specified in Equations 4.7-4.9 for forces and $P_t w \in \mathbb{R}$ - the total pressure in the section which is combination of the pressures in the individual muscles such that $P_t = P_1 + P_2 + P_3$. In the Figures 4.5, 4.8, 4.9, 4.12 and 4.13, the plots with the value m calculated as shown in Equation 4.11, and the resultant and total input pressure values denoted by F_r and Ft, are shown.

$$m = 1.6(sk)^2 = 1.6(s.\frac{s}{r})^2 = 1.6(\frac{s^4}{r^2}) \tag{4.11}$$

It was observed that the value of m follows the pattern of the pressure values, and in some cases transitions from the resultant pressure value (P_r) to total pressure value (P_t). It is also interesting to note that this transition happens exactly when the the section curls and forms a circle (as seen in Figure 4.7). For example, for the 'two muscles with same pressure case' shown in Figure 4.5, the transition happens between the 3rd and 4th data point, which from Chapter 3 is known to be between 19.5 PSI (Figure 4.6) and 22.75 PSI (Figure 4.7). This is also the case with the data shown in Figure 4.8. For , It can be seen in the cases whose data is shown in Figures 4.12 and 4.13 that the aforementioned transition does not occur. It can also be seen that the sections do not curl in a circular form. The transition does also occur in the single muscle actuation shown in Figure 4.9 when the sections curls.

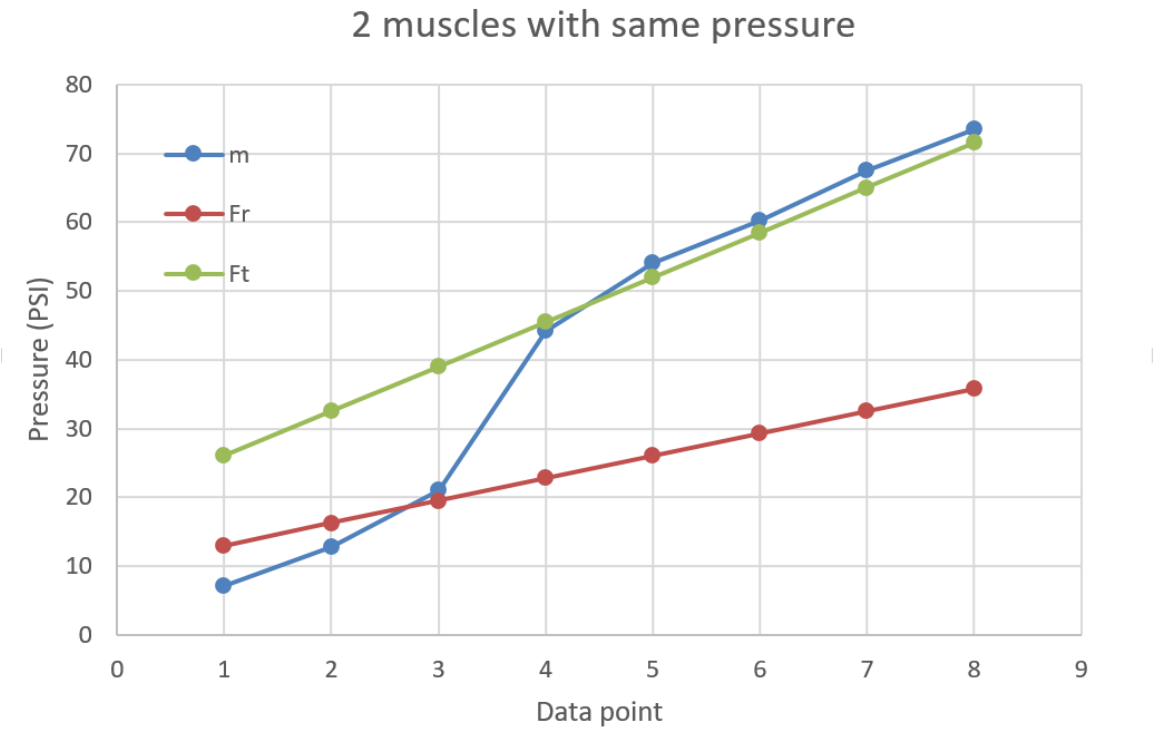

Figure 4.5: 2 muscles with same pressure - observation

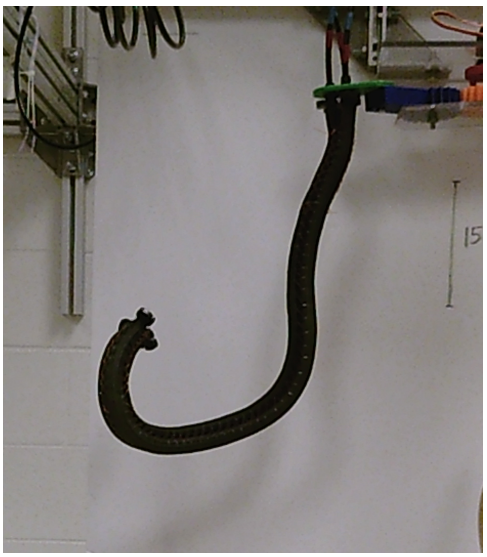

Figure 4.6: Two muscles with 19.5 PSI - data point 3

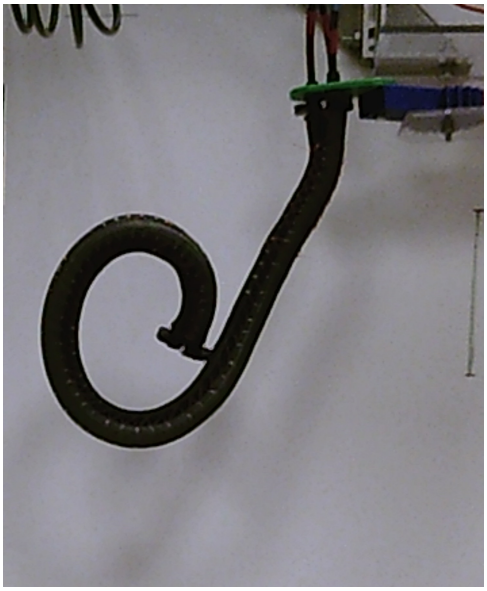

Figure 4.7: Two muscles with 22.75 PSI - data point 4

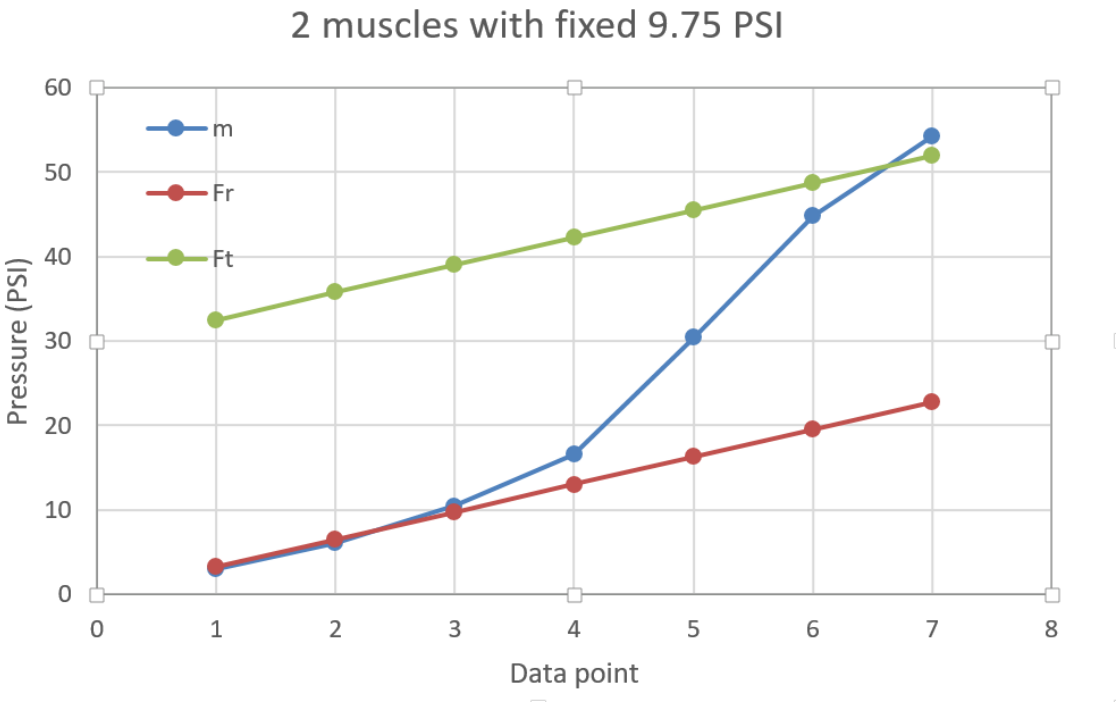

Figure 4.8: 2 muscles with fixed 9.75 PSI - observation

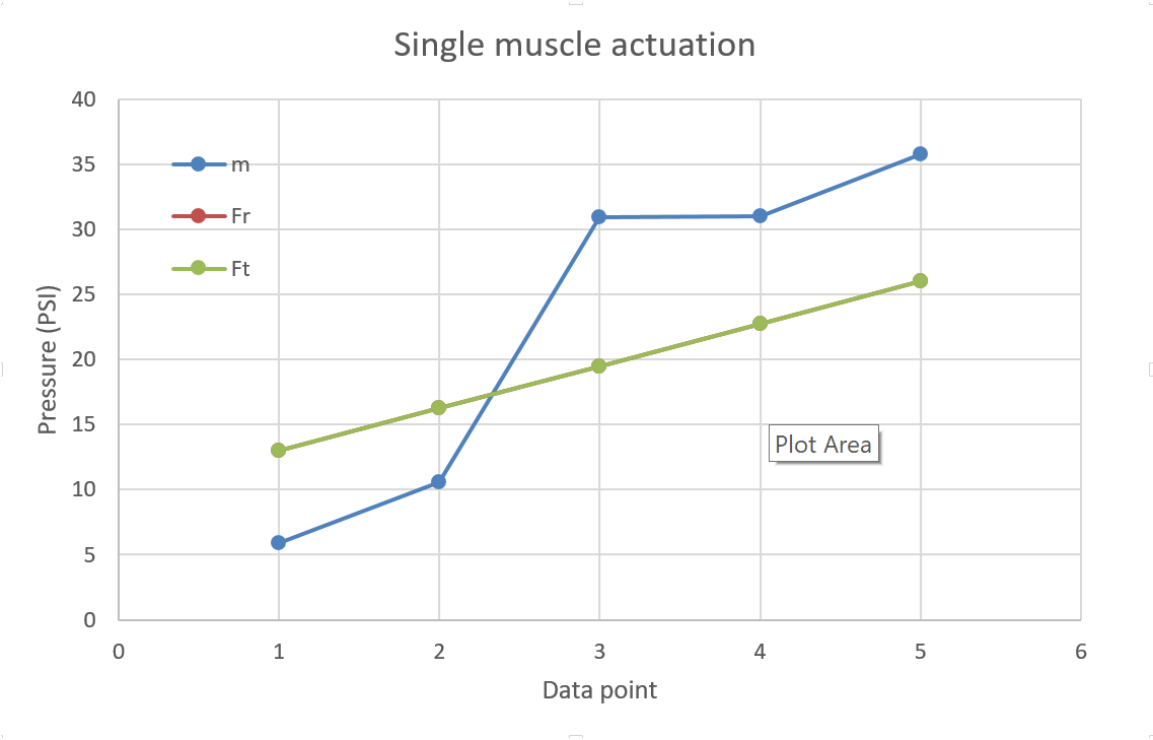

Figure 4.9: Mawby single muscle actuation - observation

Figure 4.10: Mawby single muscle actuation - 16.25 PSI

Figure 4.11: Mawby single muscle actuation - 19.5 PSI

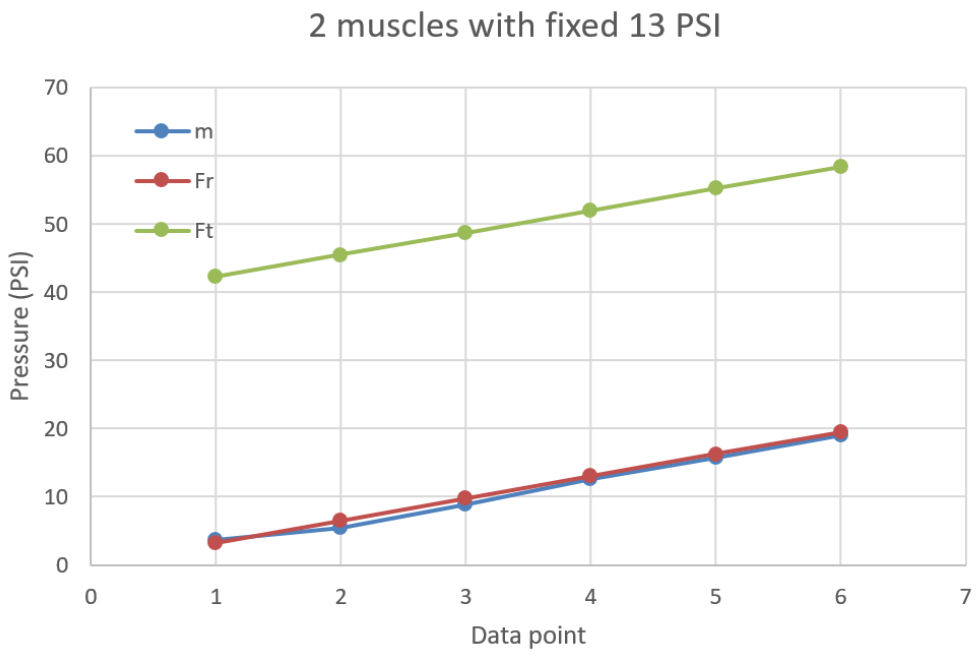

Figure 4.12: 2 muscles with fixed 13 PSI - observation

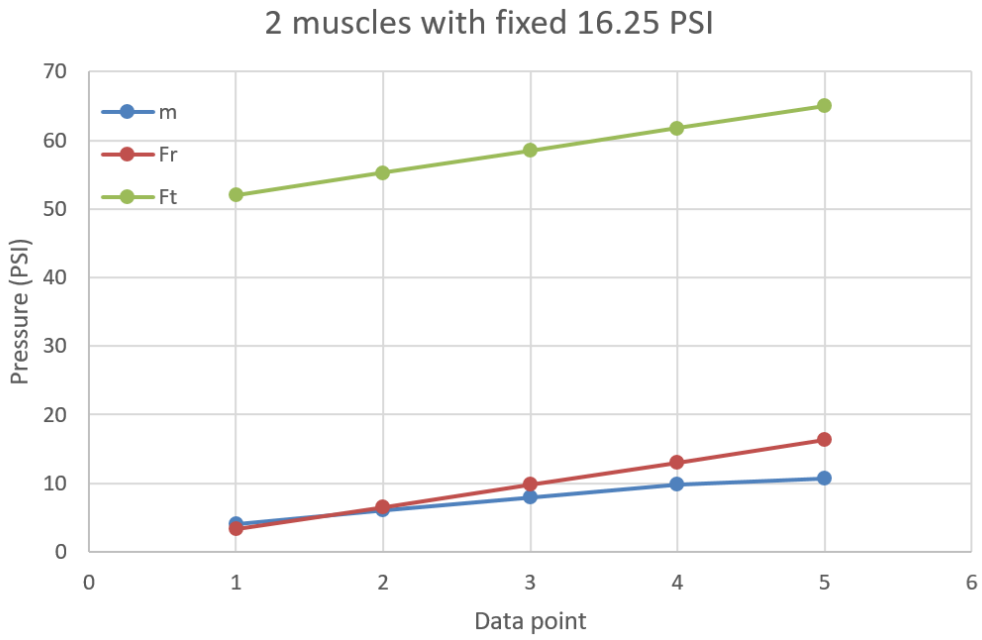

Figure 4.13: 2 muscles with fixed 16.25 PSI - observation

Although it is still unclear why this transition takes place, if this phenomenon exists for other for all curves generated for the Mawby sections in Chapter 3, a model to relate the pressure values to corresponding curvatures could be developed and hence this phenomenon needs to be further investigated.

4.3 Calculation of Forces in a Pneumatic Artificial Muscle

The Pneumatic Artificial muscles construed for the robots discussed in this thesis are not fully governed by the force equations shown in Equation 4.1. The effects of the change in volume of the tubing and and its interaction with the braid needs to be considered to understand the forces involved in the continuum structure and to accurately predict their movements. As discussed in Chapter 2, a Mawby section comprises of three McKibben Pneumatic Artificial muscles connected along their length 120° apart. The models developed by Chou and Hannaford [41] for static and dynamic modeling of the contracting forms of these muscles are widely used. The equation of the force $F \in \mathbb{R}$ generated in a contractor muscle due to applied pressure is given in [41] as

$$F = \frac{Pb^2(3\cos^2\theta - 1)}{4\pi n^2} \tag{4.12}$$

where,

$P \in \mathbb{R}$ is relative pressure

$\theta \in \mathbb{R}$ is angle between a braided thread of the artificial muscle sleeve and the cylinder long axis

$n \in \mathbb{R}$ is number of turns of a thread

$b \in \mathbb{R}$ is thread length.

An equivalent simplified version of Equation 4.12 is given by:

$$F = \frac{\pi D_o^2 P}{4}(3\cos^2\theta - 1) \tag{4.13}$$

where,

$D_o \in \mathbb{R} = b/n\pi$ is the diameter of the cylinder when θ equals 90°

The force generated by the McKibben actuator is therefore a function of the pressure and the braid angle. Based on the Chou-Hannaford equations, Giri [42] proposed a new model for the extensor versions of these air muscles given by:

$$F = \frac{Pb^2}{4\pi n^2}(1 - \frac{3L^2}{b^2}) \tag{4.14}$$

where, $L \in \mathbb{R}$ is the length of the actuator and other notations are same as Equation 4.12.

Numerous other models for the McKibben actuators, for example [43] and [44], based on the principle of work/energy conservation, have been proposed. However, there are many assumptions made in these models. For example, one of the assumptions made in Chou-Hannaford is that there is always contact between the tube and the sleeving. This is not true in Mawby's case, since the Mawby muscles exhibit little contact between braid and inner tube at low pressures. Because of disparities such as this, calculating the forces that pneumatic muscles generate is difficult to predict accurately and are subject to change based on the construction and operation of the muscle.

4.4 A Second Observation

A second observation results from the fact that for the single muscle actuation and the two muscle actuation cases, a given resultant force does not correspond to a unique curvature. The curvature for two muscles with the same pressures applied to them is lower than the curvature of a single muscle with the same amount of pressure applied to it. This can be seen in Figures 4.14 and 4.15. This is due to the fact that as the pressures in the muscles increase, the stiffness of these muscles increases as well. Furthermore, increases in the total pressure results in a stiffer sections with a lower curvatures. A similar observation is made in [45], and an equation to calculate this stiffness due to pressure in a McKibben muscle is given by Equation 4.15.

$$s = \frac{P_g \Delta V}{L^2} - \frac{f_{rs}}{\Delta L} - \frac{f_r}{\Delta L} \tag{4.15}$$

where $P_g \in \mathbb{R}$ is the input air pressure,

$f_r \in \mathbb{R}$ is the resistance force,

$f_{rs} \in \mathbb{R}$ is the resistance dependent on the stiffness of the rubber,

ΔV is the volume change,

$L \in \mathbb{R}$ is the actuator length and

ΔL is the change in actuator length.

Figure 4.14: Single muscle with 16.25 PSI

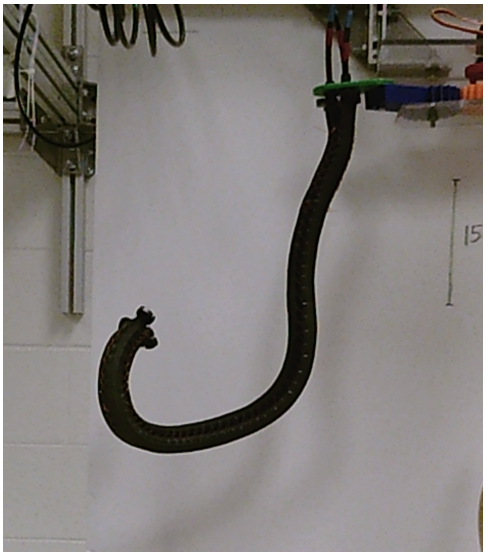

Figure 4.15: 2 muscles each with 16.25 PSI

Due to the highly non-linear features exhibited by a pneumatic actuator muscle as detailed in [43], their modeling is difficult and currently inaccurate. The accurate modeling of a continuum section such as those discussed in this thesis depends on the understanding of the forces involved in their constituent muscles and their accurate modeling.

Chapter 5

Conclusions and Future Work

In this thesis, two novel continuum manipulators were designed, tested and discussed. A new kinematic model was also proposed to more accurately predict the shape and tip position of these robots than the conventional models used. A novel parallel continuum robot gripper featuring a webbing between its continuum fingers was designed and built. To the best of our knowledge, the addition of webbing on a continuum manipulator has not previously been considered in the existing literature, and presents unique possibilities for manipulation which were investigated and discussed. Due to its elastic properties, the webbing provided opportunities for grasping objects the manipulator might not have otherwise been able to grasp or manipulate. The results discussed in Chapter 2 provide insight into the potential of the manipulator and the webbing to provide better grasping an manipulation capabilities in comparison to existing continuum robots, without the use of additional actuators. Mawby, the parallel continuum robot, had its design inspiration taken from the Barrett Hand, which is unique in allowing various orientations of the parallel continuum sections to better grasp objects. The Mawby robot is the first parallel continuum robot to feature adjustable relative section base positions, or to use a compliant webbing. Results

with the prototype demonstrate novel, adaptive, and compliant grasping of a wide range of objects.

Another novel parallel continuum robot, named Separating Sections, was designed and built. The three sections in the robot could operate as a single serial section unit, but could also branch out into three separate and distinct units as the situation demanded. This design has the potential to be useful for locomotion in tight spaces and manipulating payloads on the far side of tight obstacle fields at the same time. The ability of the robot to work as both a single unit and multiple units are investigated and discussed.

The third key novel idea introduced in this thesis is the use of Euler spirals to model continuum robot sections. When compared to the constant curvature model, which is the state-of-the-art for such manipulators, the Euler Spirals model yielded a 93% improvement in predicting the shape in the sections of Mawby. This new approach was applied to continuum sections of the Separating Sections robot and the results were similar. The sections of Separating Sections are shorter than Mawby's, and the results were seen to be more consistent for these shorter section. In Chapter 3, different versions of the Euler spiral model were investigated and compared. The most accurate model was then applied to 42 different curves that were generated by different combination of pressure values in the three muscles of a section. These results were then analyzed in Chapter 4 to understand the limitations and application of this modeling approach.

5.1 Future work

Finally, we list a number of areas for extension and improvement of the work presented in this thesis.

1. One of the prime factors of the highly non-constant curvature behavior of the robots discussed in this thesis is the method of construction of the individual muscles. Many variations were made in the construction of the long, thin sections for Mawby and Separating Sections to achieve greater extension and bending. When compared with the muscles comprising the sections in the visibly constant curvature Octarm, the rubber tubing was longer, more flexible, and had smaller diameter. More of the braided sleeving was added on the tubing resulting in the tube and the braided sleeve and tubing were not in solid contact with each other at rest. The muscles were stitched together using thread as opposed to the use of zip ties in the Octarm. However, zip ties were used in the construction of the Separating Sections, so sewing does not seem to be a fundamental cause of change in behavior of these thin, long sections. More investigation needs to be made on the effect of construction techniques on the behavior of these muscles. Investigating the effects on a shorter section (possibly even shorter that the Octarm section) would be a good place to start. Using less braid (in length) with smaller diameter in long, thin muscles to ensure contact between the tubing and the sleeve, especially at rest could provide additional insight into the behavior of such robots that is currently not fully understood.

2. Robot grippers have been constructed using Ecoflex 00-30 (Smooth-On, Inc) for the construction of artificial muscles. This material was also used to construct the webbing during the course of this thesis. The sections in the robots using these materials to date are relatively short. The implementation of Euler spiral kinematics on thin, long continuum sections constructed with these materials would be interesting and potentially very useful.

3. It was shown that the Euler spiral modeling approach was more accurate in predicting not only the tip position of a continuum manipulator, but also the shape of the entire robot. A greater, more in depth understanding of the Euler Spirals model

for continuum robots is needed, with a potential benefit of determining an accurate inverse kinematic model.

4. The continuum robot sections discussed in this thesis were thin, long and highly flexible, resulting in the forces generated by them to be incapable of causing significant structural or physical damage to most objects they would come into contact with. A rigid support structure could be built to keep these compliant structures more stable when interacting with external forces.

5. Force sensors could be mounted on the continuum robot sections to better understand the forces generated by them at the point of contact with the object. Calculation of these forces using external and indirect techniques is extremely difficult and highly unreliable due to the compliant nature of these sections.

6. Interacting with objects is the primary application of a gripper. Investigating the effects of force by empirical investigation would give a better understanding of the limitations and capabilities of these kinds of robots.

7. Upon gaining a better understanding of the effect of weight on the behavior of the continuum gripper, the additional effect of the webbing can be analyzed. Being attached along the length of the section at two points on the cross section, the webbing has proved advantageous during the experiments by restricting excessive bending the sections. By varying the weight and position of the webbing, an optimal value for these parameters could be achieved.

Appendices

Appendix A

Matlab Code

A.1 Matlab Code for Kinematic Modeling

```
%close all
clear xn yn xn2 yn2;
r2 = 0.18;
m=1;
r=0.06;
for i=0.05:0.004:0.58
%for i=0.74:0.004:3.1
% %Final Euler
xn(m) = (r/i)*(sin((i*i)/(r)));
yn(m) = -(r/i)*(cos((i*i)/(r)));
% %Simple Euler
%     xn(m) = r*(sin((i*i)));
%     yn(m) = -r*(cos((i*i)));
```

```
%
% %Euler in paper
%     xn(m) = (r/i)*(cos((i*i)/(r))-1);
%     yn(m) = (r/i)*(sin((i*i)/(r)));
%
% %Modified Euler
%     xn(m) = (r/i)*(cos((i*i)/(r))-1);
%     yn(m) = (r/i)*(sin((i*i)/(r)));
%     r=r-0.00020;
%
% %Plant Curl
%     xn(m) = sqrt(pi/r)*(sin(i*i));
%     yn(m) = -sqrt(pi/r)*(cos(i*i));
%      r=r+0.007;


m=m+1;
end
m=1;
for i=0.01:0.004:0.375              %Constant Curvature


xn2(m) = (r2)*(cos((i)/r2)-1);
yn2(m) = (r2)*(sin((i)/r2));


m=m+1;
end
```

```
origin = [final(1,1) final(1,2) 0];
%xn2=5000;
xn2(:) = xn2(:)*4000;
yn2(:) = yn2(:)*4000;
%final euler : xn*2100
%simple euler : xn*1300
%paper euler/modified : xn*3300
%plant : xn(:)*240;
xn(:) = xn(:)*3300;
yn(:) = yn(:)*3300;
xn(:) = xn(:)-xn(1)+final(1,1);
yn(:) = yn(:)-yn(1)+final(1,2);
xn2(:) = xn2(:)-xn2(1)+final(1,1);
yn2(:) = yn2(:)-yn2(1)+final(1,2);
figure(3);
subplot(1,2,1);
imshow(d);
hold on
h = plot(xn(:),yn(:),'r','LineWidth',2);axis([0 3000 0 3000]);
set(gca,'Ydir','reverse');
%hold off
legend({'Euler'},'Location','southeast','FontSize',16);
%figure(4);
%subplot(1,2,2);
imshow(d);
hold on
```

```
h2 = plot(xn2(:),yn2(:),'g','LineWidth',2);
axis([0 3000 0 3000]);set(gca,'Ydir','reverse');
legend({'CC'},'Location','southeast','FontSize',16);
direction = [0 0 1];
rotate(h,direction,-120,origin);
rotate(h2,direction,-13,origin);

% [b3 a3] = butter(2, 0.5, 'low');
% filtert22(:,1) = filter(b3,a3,final(:,1));
% filtert22(:,2) = filter(b3,a3,final(:,2));
% plot(filtert22(:,1),filtert22(:,2),'b','LineWidth',3);
%pbaspect([1 1 1]);
%axis([0 3000 0 3000]);set(gca,'Ydir','reverse')
% figure(3); plot(final(:,1),final(:,2),'b','LineWidth',3);
%pbaspect([1 1 1]);
%axis([0 3000 0 3000]);set(gca,'Ydir','reverse')
%legend({'Euler','CC'},'Location','northeast','FontSize',14);
```

A.2 Matlab Code for Error Calculation

```
clear xnn2 ynn2 eul;
mul = 0.15/510;
%mul = 0.1/104;
%mul = 0.105/339;
theta = 145;
esq2=0;
%rz = [cosd(theta) -sind(theta) 0; sind(theta) cosd(theta) 0;0 0 1];
R = [cosd(theta) -sind(theta); sind(theta) cosd(theta)];
for m=1:size(xn,2)
xy = R*[xn(1,m); yn(1,m)];
xnn2(1,m) = xy(1);
ynn2(1,m) = xy(2);
end

xnn2(:) = xnn2(:)-xnn2(1)+final(1,1);
ynn2(:) = ynn2(:)-ynn2(1)+final(1,2);
eul(:,1) = xnn2(1,:);
eul(:,2) = ynn2(1,:);
%f = (size(yn,2)/size(final,1));

[k2, D2] = dsearchn(eul,final)

for i=1:size(final,1)
```

```
%n(i) = round(i*f);
err2(i) = mul*(sqrt((final(i,1)-xnn2(1,k2(i)))^2 + (final(i,2)-ynn2(1,k2(i)))^2));
esq2 = esq2+err2(i)^2;
end
e_mean = esq2/size(final,1)
rms=sqrt(e_mean)

%  k = dsearchn(eul,XI)
figure(27);plot(final(:,1),final(:,2),'b','LineWidth',2);
pbaspect([1 1 1]);axis([0 3000 0 3000]);set(gca,'Ydir','reverse')
hold on; plot(xnn2(:),ynn2(:),'r','LineWidth',2);
axis([0 3000 0 3000]);set(gca,'Ydir','reverse');
legend({'Mawby','Euler'},'Location','northwest','FontSize',14);
```

A.3 Matlab Code for Resultant Force Calculation

```
clear all
m=1;n=1;

for i=1:0.25:17
for j=1:0.25:17

Fx = i*cosd(30) - j*cosd(30);
Fy = i*cosd(60) + j*cosd(60);

Fr(n,1) = sqrt(Fx^2+Fy^2);
theta(n,1) = atan2d(Fy,Fx);

if Fr(n,1)>14.5 && Fr(n,1)<15
P(m,1) = i;
P(m,2) = j;
P(m,3) = theta(n,1);
m=m+1;
end
n=n+1;
end
end

% figure(6);plot(P(:,1),'b-*')
```

```
% hold on
% figure(6);plot(P(:,2),'r-*')


PS = sortrows(P,3);
figure(7);plot(PS(:,1),'b*')
hold on
figure(7);plot(PS(:,2),'r*')
legend({'F2','F3'},'Location','southeast','FontSize',16);
PSV(:,1) = PS(:,1)/13;
PSV(:,2) = PS(:,2)/13;
PSV1(:,1) = PSV(:,1);
PSV2(:,1) = PSV(:,2);
```

Bibliography

[1] B. S. Homberg, R. K. Katzschmann, M. R. Dogar, and D. Rus, "Haptic identification of objects using a modular soft robotic gripper," in *Proc. IEEE/RSJ Int. Conf. Intel. Robot. Syst.*, Hamburg, Germany, 2015, pp. 1698–1705.

[2] M. Hannan and I. Walker, "Analysis and experiments with an elephant's trunk robot," *Advanced Robotics*, vol. 15, no. 8, pp. 847–858, Aug. 2001.

[3] W. McMahan, B. Jones, and I. Walker, "Robotic manipulators inspired by cephalopod limbs," *Jour. Eng. Des. Inno.*, vol. 1.

[4] S. Hirose, *Biologically Inspired Robots*. Oxford, UK: Oxford University Press, 1993.

[5] J. L. C. Santiago, I. S. Godage, P. Gonthina, and I. D. Walker, "Soft robots and kangaroo tails: Modulating compliance in continuum structures through mechanical layer jamming," *Soft Robotics*, vol. 3, no. 2, pp. 54–63, Jun. 2016.

[6] M. B. Wooten, "Novel vine-like continuum robot for environmental exploration applications," Master's thesis, Clemson University, 2016.

[7] J. Li, Z. Teng, J. Xiao, A. Kapadia, A. Bartow, and I. Walker, "Autonomous continuum grasping," in *Proc. IEEE/RSJ Int. Conf. Intel. Robot. Syst.*, Tokyo, Japan, 2013, pp. 4569–4576.

[8] H. Mao, J. Xiao, M. M. Zhang, and K. Daniilidis, "Shape-based object classication and recognition through continuum manipulation," in *Proc. IEEE/RSJ Int. Conf. Intel. Robot. Syst.*, Vancouver, BC, Canada, 2017, pp. 456–463.

[9] N. Simaan, R. Taylor, and P. Flint, "A dextrous system for laryngeal surgery," in *Proc. IEEE Int. Conf. Robot. Autom.*, New Orleans, LA, 2004, pp. 351–357.

[10] J. Mehling, M. Diftler, M. Chu, and M. Valvo, "A minimally invasive tendril robot for in-space inspection," in *Proc Biorobotics Conference*, Pisa, Italy, 2006, pp. 690–695.

[11] R. Buckingham, "Snake arm robots," *Ind. Robot: An Int. Jour.*, vol. 29, no. 3, pp. 242–245, Mar. 2002.

[12] R. Webster III and B. A. Jones, "Design and modeling of constant curvature continuum robots," *Int. Jour. Robots. Res.*, vol. 29, no. 13, pp. 1661–1683, Jul. 2010.

[13] G. Chirikjian, "Hyper-redundant manipulator dynamics: A continuum approximation," *Adv. Robot.*, vol. 9, no. 3, pp. 217–243, Jun. 1995.

[14] I. Godage, E. Guglielmino, D. Branson, G. MedranoCerda, and D. Caldwell, "Novel modal approach for kinematics of multisection continuum arms," in *Proc. IEEE/RSJ Int. Conf. Intel. Robot. Syst.*, San Francisco, CA, 2011, pp. 1093–1098.

[15] H. Mochiyama and T. Suzuki, "Kinematics and dynamics of a cable-like hyper-flexible manipulator," in *Proc. IEEE Int. Conf. Robot. Autom.*, Taipei, Taiwan, 2003, pp. 3672–3677.

[16] I. S. Godage, R. Wirz, I. D. Walker, , and R. J. W. III, "Accurate and efficient dynamics for variable-length continuum arms: A center of gravity approach," *Soft Robotics*, vol. 2, no. 3, pp. 96–106, Jun. 2015.

[17] M. Mahvash and P. Dupont, "Stiffness control of a continuum manipulator in contact with a soft environment," in *Proc. IEEE/RSJ Int. Conf. Intel. Robot. Syst.*, Taipei, Taiwan, 2010, pp. 863–870.

[18] T. Mahl, A. E. Mayer, A. Hildebrandt, and O. Sawodny, "A variable curvature modeling approach for kinematic control of continuum manipulators," in *2013 American Control Conference.*, Washington, DC, 2013, pp. 4945–4950.

[19] D. Trivedi, A. Lofti, and C. Rahn, "Geometrically exact dynamic models for soft robotic manipulators," in *Proc. IEEE/RSJ Int. Conf. Intel. Robot. Syst.*, San Diego, CA, 2007, pp. 1497–1502.

[20] S. Sadati, S. E. Naghibi, A. Shiva, I. D. Walker, K. Althoefer, and T. Nanayakkara, "Mechanics of continuum manipulators, a comparative study of five methods with experiments," in *Towards Autonomous Robotic Systems*, Surrey, UK,, 2017, pp. 686–702.

[21] K. Hsiao and H. Mochiyama, "A wire-driven continuum manipulator model without assuming shape curvature constancy," in *Proc. IEEE/RSJ Int. Conf. Intel. Robot. Syst.*, Vancouver, BC, Canada, 2017, pp. 436–443.

[22] M. Giorelli, F. Renda, M. Calisti, A. Arienti, G. Ferri, and C. Laschi, "A two dimensional inverse kinetics model of a cable driven manipulator inspired by the octopus arm," in *Proc. IEEE Int. Conf. Robot. Autom.*, Saint Paul, Minnesota, USA, 2012, pp. 3819–3824.

[23] Z. Wang, Y. Torigoe, and S. Hirai, "A prestressed soft gripper: Design, modeling, fabrication, and tests for food handling," in *Proc. IEEE/RSJ Int. Conf. Intel. Robot. Syst.*, Vancouver, BC, Canada, 2017.

[24] H. Zhang, M. Y. Wang, F. Chen, Y. Wang, A. S. Kumar, and J. Y. H. Fuh, "Design and development of a soft gripper with topology optimization," in *Proc. IEEE/RSJ Int. Conf. Intel. Robot. Syst.*, Vancouver, Canada, 2017, pp. 6239–6244.

[25] M. C. S. Yuen, T. R. Lear, H. Tonoyan, M. Telleria, and R. Kramer-Bottiglio, "Toward closed-loop control of pneumatic grippers during pack-and-deploy operations," *IEEE Robotics and Automation Letters*, vol. 3, no. 3, pp. 1402–1409, July 2018.

[26] P. Glick, S. A. Suresh, D. R. III, M. Cutkosky, M. T. Tolley, and A. Parness, "A soft robotic gripper with gecko-inspired adhesive," *IEEE Robotics and Automation Letters*, vol. 3, no. 2, pp. 903–910, April 2018.

[27] C. Choi, W. Schwarting, J. DelPreto, and D. Rus, "Learning object grasping for soft robot hands," *IEEE Robotics and Automation Letters*, vol. 3, no. 3, pp. 2370–2377, July 2018.

[28] B. Shih, D. Drotman, C. Christianson, Z. Huo, R. White, H. I. Christensen, and M. T. Tolley, "Custom soft robotic gripper sensor skins for haptic object visualization," in *Proc. IEEE/RSJ Int. Conf. Intel. Robot. Syst.*, Vancouver, BC, Canada, 2017, pp. 494–501.

[29] I. D. Walker, "Continuous backbone continuum robot manipulators," *ISRN Robotics*, vol. 2013, pp. 54–63, 2013.

[30] B. H. et al., "Field experiments with the octarm continuum manipulator," in *Proc. IEEE/RSJ Int. Conf. Intel. Robot. Syst.*, Beijing, China,, 2006, pp. 10–10.

[31] T. Yoshimi, N. Iwata, M. Mizukawa, and Y. Ando, "Picking up operation of thin objects by robot arm with two-fingered parallel soft gripper," in *IEEE International Workshop on Advanced Robotics and its Social Impacts*, Munich, Germany, 2012, pp. 7–12.

[32] F. Daerden and D. Lefebe, "Pneumatic artificial muscles: actuators for robotics and automation," *European journal of mechanical and environmental engineering*, vol. 47, pp. 10–21, 2000.

[33] M. Grissom, V. Chitrakaran, D. Dienno, M. Csencsits, M. Pritts, B. Jones, W. McMahan, D. Dawson, C. Rahn, and I. Walker, "Design and experimental testing of the octarm soft robot manipulator," in *Proc. SPIE Conf. Unmanned Sys. Tech.*, Kissimee, FL, 2006, pp. 109–114.

[34] M. R. Hasan, R. Vepa, H. Shaheed, and H. Huijberts, "Modelling and control of the barrett hand for grasping," in *International Conference on Computer Modelling and Simulation*, Cambridge, UK, 2013, pp. 230–235.

[35] B. Jones and I. Walker, "Kinematics of multisection continuum robots," *IEEE Trans. Robot.*, vol. 22, no. 1, pp. 43–57, Feb. 2006.

[36] M. Hannan and I. Walker, "Kinematics and the implementation of an elephant trunk manipulator and other continuum style robots," *J. Robot. Sys.*, vol. 20, no. 2, pp. 45–63, Feb. 2003.

[37] Y. Chen, Y. Cai, J. Zheng, and D. Thalmann, "Accurate and efcient approximation of clothoids using bezier curves for path planning," *IEEE Trans. Robot.*, vol. 33, no. 5, pp. 1242–1247, Oct. 2017.

[38] Levien and Raph, "The euler spiral: a mathematical history," 2008.

[39] A. Rafsanjani, V. Brul, T. L. Western, and D. Pasini, "Hydro-responsive curling of the resurrection plant selaginella lepidophylla," *Scientific Reports*, vol. 5, no. 8064, Jan 2015.

[40] J. Fras, J. Czarnowski, M. Macias, and J. Gwka, "Static modeling of multisection soft continuum manipulator for stiff-flop project," in *Recent Advances in Automation, Robotics and Measuring Techniques*, Cham, 2014, pp. 365–375.

[41] C.-P. Chou and B. Hannaford, "Measurement and modeling of mckibben pneumatic artificial muscles," *IEEE Transactions on robotics and automation*, vol. 12, no. 1, pp. 90–102,, 1996.

[42] N. Giri, "A new approach to dynamic modeling of continuum robots," Master's thesis, Clemson University, 2011.

[43] B. Tondu and P. Lopez, "Modeling and control of mckibben artificial muscle robot actuators," *IEEE Control Systems*, vol. 20, no. 2, pp. 15–38,, 2000.

[44] H. Al-Fahaam, S. Davis, and S. Nefti-Meziani, "A novel, soft, bending actuator for use in power assist and rehabilitation exoskeletons," in *Proc. IEEE/RSJ Int. Conf. Intel. Robot. Syst.*, Vancouver, BC, Canada, 2017, pp. 533–538.

[45] A. Al-Ibadi, S. Nefti-Meziani, and S. Davis, "Efficient structure-based models for the mckibben contraction pneumatic muscle actuator: The full description of the behaviour of the contraction pma," *Actuators*, vol. 6, no. 4, 2017.